PNNL-28065
DVZ-RPT-0015 Rev 0

Pacific Northwest NATIONAL LABORATORY

Sensitivity Analysis of Contaminant Transport from Vadose Zone Sources to Groundwater

Case Study for Hanford Site B-Complex

September 2018

ML Rockhold
X Song
JD Tagestad
PD Thorne
GD Tartakovsky
X Chen

U.S. DEPARTMENT OF ENERGY

Prepared for the U.S. Department of Energy
under Contract DE-AC05-76RL01830

DISCLAIMER

This report was prepared as an account of work sponsored by an agency of the United States Government. Neither the United States Government nor any agency thereof, nor Battelle Memorial Institute, nor any of their employees, makes **any warranty, express or implied, or assumes any legal liability or responsibility for the accuracy, completeness, or usefulness of any information, apparatus, product, or process disclosed, or represents that its use would not infringe privately owned rights**. Reference herein to any specific commercial product, process, or service by trade name, trademark, manufacturer, or otherwise does not necessarily constitute or imply its endorsement, recommendation, or favoring by the United States Government or any agency thereof, or Battelle Memorial Institute. The views and opinions of authors expressed herein do not necessarily state or reflect those of the United States Government or any agency thereof.

PACIFIC NORTHWEST NATIONAL LABORATORY
operated by
BATTELLE
for the
UNITED STATES DEPARTMENT OF ENERGY
under Contract DE-AC05-76RL01830

Printed in the United States of America

Available to DOE and DOE contractors from the
Office of Scientific and Technical Information,
P.O. Box 62, Oak Ridge, TN 37831-0062;
ph: (865) 576-8401
fax: (865) 576-5728
email: reports@adonis.osti.gov

Available to the public from the National Technical Information Service
5301 Shawnee Rd., Alexandria, VA 22312
ph: (800) 553-NTIS (6847)
email: orders@ntis.gov <http://www.ntis.gov/about/form.aspx>
Online ordering: http://www.ntis.gov

This document was printed on recycled paper.
(8/2010)

PNNL-28065
DVZ-RPT-0015 Rev 0

Sensitivity Analysis of Contaminant Transport from Vadose Zone Sources to Groundwater

Case Study for Hanford Site B-Complex

September 2018

ML Rockhold
X Song
JD Tagestad
PD Thorne
GD Tartakovsky
X Chen

Prepared for
the U.S. Department of Energy
under Contract DE-AC05-76RL01830

Pacific Northwest National Laboratory
Richland, Washington 99352

Executive Summary

Remedy selection and implementation in the Central Plateau of the Hanford Site will be facilitated by a technically defensible description of vadose zone sources and their spatial and temporal impacts on groundwater. To this end, a case study approach is used to assess impacts to groundwater associated with uncertainties in source terms and hydraulic and sorption parameters for the B-Complex at Hanford. Several unplanned releases of wastes occurred in the tanks in the B-Complex. Several planned liquid waste discharges also occurred to cribs, trenches, tile fields, and French drains within the B-Complex, creating a significant inventory of contaminants in the vadose zone whose downward migration in the subsurface pose a potential threat to groundwater. Given the uncertainty in multiple source locations, volumes and intensities, and uncertainties in hydraulic and sorption properties, an integrated assessment of their combined effects is needed to guide characterization, support selection of appropriate remedies, and design appropriate monitoring for vadose zone source areas and the underlying aquifer.

This report documents initial simulation results investigating the sensitivities that multiple source areas have on source attribution in groundwater using the B-Complex as a case study. Uncertainty in both liquid volumes and contaminant masses (NO_3) or activities (Tc-99) discharged to the 36 waste sites at the B-Complex were simulated without considering uncertainty in the timing of the releases. Uncertainty associated with hydraulic and sorption parameters was also considered. Based on predicted groundwater concentrations and contaminant flux to ground water, sorption parameters had the largest impact on contaminant flux to groundwater. Uncertainty associated with source mass and volumes had the least impact on predicted groundwater concentrations. This implies that the chemical and physical properties of the vadose zone have a greater impact on contaminant flux to groundwater than the release mass/activity and volumes. Hence, remedies may need to largely focus on reducing contaminant fluxes to the water table.

Simulations that accounted for uncertainties in hydraulic parameters, sorption parameters, and source terms predicted groundwater concentrations that bracketed measured concentrations for many of the observation wells that were selected for comparisons. Predictions matched observed concentrations more closely for Tc-99 than for NO_3 at most of the groundwater monitoring locations. Simulation results also indicate that a significant inventory of contaminants still remains in the vadose zone, and is predicted to persist well into the future (beyond year 2100), posing a continuing contaminant flux to groundwater.

Acknowledgments

This work was supported by DOE Richland Operations Office. Pacific Northwest National Laboratory (PNNL) is operated by Battelle Memorial Institute for the DOE under contract DE-AC05-76RLO1830.

We thank Patrick Royer (PNNL) for providing NAIP imagery that was used for land classification, Bob Moore and Fred Zhang for independent technical review, and Matt Wilburn for editorial review and document formatting assistance. Vicky Freedman is acknowledged for management review, and Becky Jones is acknowledged for project management support.

Acronyms and Abbreviations

CCU	Cold Creek Unit
CCUc	Cold Creek Unit - carbonate
CCUg	Cold Creek Unit – gravel-dominated
CCUz	Cold Creek Unit – silt-dominated
CPVZ	Central Plateau Vadose Zone
CHPRC	CH2M Hill Plateau Remediation Company
eSTOMP	exascale Subsurface Transport Over Multiple Phases
FIO	For Information Only
fm	formation
GFM	Geologic Framework Model
H1, H2, H3	subunits of the Hanford formation
HEIS	Hanford Environmental Information System
NQAP	Nuclear Quality Assurance Program
PNNL	Pacific Northwest National Laboratory
PWA	perched-water aquifer
Rlm	Ringold Formation Lower Mud unit
Rtf	Ringold Formation Taylor Flat unit
Rwia	Ringold Formation member Wooded Island unit A
Rwie	Ringold Formation member Wooded Island unit E
SIM	Soil Inventory Model
TCT	tensorial connectivity-tortuosity

Contents

Executive Summary ii
Acknowledgments iii
Acronyms and Abbreviations iv
1.0 Introduction 1.1
2.0 Site Description 2.1
2.1 Hydrogeology 2.2
2.2 Liquid Effluent and Waste Release Estimates 2.2
3.0 Sensitivity Analysis Methodology 3.1
3.1 Hydraulic and Sorption Parameters 3.2
3.2 Source Terms 3.4
4.0 Results and Discussion 4.1
4.1 Sensitivity of Groundwater Concentrations to Hydraulic Parameters 4.1
4.2 Sensitivity of Groundwater Concentrations to Sorption Parameters 4.7
4.3 Sensitivity to Groundwater Concentrations to Source Terms 4.9
4.4 Sensitivity of Fluxes from Vadose Zone to Groundwater to Hydraulic Parameters, Sorption Parameters, and Source Terms 4.11
4.5 Discussion 4.15
5.0 Conclusions 5.1
6.0 Quality Assurance 6.1
7.0 References 7.1
Appendix A – Model Development A.1
Appendix B – Simulation Results from Baseline Model B.1

Figures

Figure 2.1. Map of the B-Complex Showing Key Facilities, Boreholes, and Wells (from Serne et al. 2010). 2.1

Figure 2.2. Hydrostratigraphic Units and Generalized Hanford Site Stratigraphy (from Hammond and Lupton 2015). 2.3

Figure 2.3. Cutaway View of Hydrostratigraphic Units Underlying the B-Complex Showing Waste Storage Tanks of the B-BX-BY Tank Farms. 2.4

Figure 2.4. Estimated Liquid Effluent Discharge Rates Over Time for Waste Sites in the B-Complex. 2.5

Figure 2.5. Estimated Tc-99 Release Rates Over Time for Waste Sites in the B-Complex. 2.6

Figure 2.6. Estimated NO_3 Release Rates Over Time for Waste Sites in the B-Complex. 2.7

Figure 2.7. Estimated Total Uranium Release Rates for Waste Sites in the B-Complex. 2.8

Figure 3.1. (a) Hierarchical uncertainty quantification framework, with (b) addition of multiple components included in model uncertainty (from Dai et al. 2017). 3.1

Figure 3.2. Realizations of Liquid Disposal Volume Perturbations for B-Complex Waste Sites Generated Using the Quasi-Monte Carlo Method. 3.5

Figure 4.1. Simulated Tc-99 Isosurfaces [1 pCi/L] for Baseline Model in 1956 Showing Tanks of the B-BX-BY Tank Farms and a Cutaway View of Hydrostratigraphic Units Underlying the B-Complex. 4.2

Figure 4.2. Simulated Tc-99 Isosurfaces [1 pCi/L] for Baseline Model in 2018 Showing Tanks of the B-BX-BY Tank Farms and a Cutaway View of Hydrostratigraphic Units Underlying the B-Complex. 4.2

Figure 4.3. Observed Concentrations of Tc-99 from Groundwater Monitoring Wells in the B-Complex and Simulation Results Illustrating the Sensitivity of Results to Uncertainties in K_s for the Hanford fm. The K_s values listed in Table 3.1 for the H1, H2, and H3 subunits were scaled as shown for the different simulation cases. 4.3

Figure 4.4. Observed concentrations of Nitrate from Groundwater Monitoring Wells in the B-Complex and Simulation Results Illustrating the Sensitivity of Results to Uncertainties in K_s for the Hanford fm. The K_s values listed in Table 3.1 for the H1, H2, and H3 subunits were scaled as shown for the different simulation cases. 4.4

Figure 4.5. Observed Concentrations of Tc-99 from Groundwater Monitoring Wells in the B-Complex and Simulation Results Illustrating the Sensitivity of Model Results to Uncertainties in the Anisotropy of Hydraulic Properties in the Hanford fm. Model_00 represents parameters from Table 3.1. Model_01 represents the TCT model for moisture-dependent anisotropy. Model_02 represents anisotropy in K_s only with $K_{xx}=K_{yy}=4*K_{zz}$. Model_03 represents the changes used in Model_01 and _02 combined. Values of $0.1*K_s$ were used as baseline parameters for all subsequent model simulations. 4.5

Figure 4.6. Observed Concentrations of Nitrate from Groundwater Monitoring Wells in the B-Complex and Simulation Results Illustrating the Sensitivity of Model Results to Uncertainties in the Anisotropy of Hydraulic Properties in the Hanford fm. Model_00 represents parameters from Table 3.1. Model_01 represents the TCT model for moisture-dependent anisotropy. Model_02 represents anisotropy is K_s only with $K_{xx}=K_{yy}=4*K_{zz}$. Model_03 uses the parameters from Model_01 and _02 combined. Values of $0.1*K_s$ were used as baseline parameters for all subsequent model simulations. 4.6

Figure 4.7. Observed Concentrations of Tc-99 from Groundwater Monitoring Wells in the B-Complex and Simulation Results Illustrating the Sensitivity of Model Results to Uncertainties in K_d for the Hanford fm. 4.7

Figure 4.8. Observed Concentrations of Nitrate from Groundwater Monitoring Wells in the B-Complex and Simulation Results Illustrating the Sensitivity of Model Results to Uncertainties in K_d for the Hanford fm. 4.8

Figure 4.9. Observed Concentrations of Tc-99 from Groundwater Monitoring Wells in the B-Complex and Simulation Results for 200 Realizations Illustrating the Sensitivity of Predicted Concentrations to Uncertainties in Source Terms. 4.9

Figure 4.10. Observed Concentrations of Nitrate from Groundwater Monitoring Wells in the B-Complex and Simulation Results for 200 Realizations Illustrating the Sensitivity of Predicted Concentrations to Uncertainties in Source Terms. 4.10

Figure 4.11. Simulated Aqueous Volumetric Flow Rates, and Flux-Averaged NO_3, Tc-99, and Total Uranium Concentrations Crossing the 122 m Elevation Over Time for Different Values of K_s. 4.12

Figure 4.12. Simulated Aqueous Volumetric Flow Rates, and Flux-Averaged NO_3, Tc-99, and Total Uranium Concentrations Crossing the 122 m Elevation Over Time for Different Cases of Anisotropy. Model_00 represents parameters from Table 3.1 (isotropic). Model_01 represents the TCT model for moisture-dependent anisotropy. Model_02 represents anisotropy in K_s only with $K_{xx}=K_{yy}=4*K_{zz}$. Model_03 represents the changes used in Model_01 and _02 combined. 4.13

Figure 4.13. Simulated Aqueous Volumetric Flow Rates, and Flux-Averaged NO_3, Tc-99, and Total Uranium Concentrations Crossing the 122 m Elevation Over Time for Different Values of K_d. 4.14

Figure 4.14. Simulated Aqueous Volumetric Flow Rates, and Flux-Averaged NO_3, Tc-99, and Total Uranium Concentrations Crossing the 122 m Elevation Over Time for 200 Realizations of Source Terms. 4.15

Tables

Table 3.1. Hydraulic and Sorption Parameters that were Varied for Model Simulations of Subsurface Flow and Transport for the Hanford B-Complex Area. 3.4

1.0 Introduction

Large groundwater contaminant plumes exist at the Hanford Site as a result of disposal of liquid wastes associated with past nuclear weapons production activities. Liquids containing mixed chemical and radioactive wastes were intentionally released to the subsurface through unlined ponds, trenches, cribs, and tile fields. Unplanned releases of contaminants also occurred from overfill events and leaks during and after the filling of some high-level waste storage tanks. Although several contaminants disposed to the vadose zone reached the underlying aquifer, there is evidence that significant quantities of contamination still remain in the vadose zone. This remaining vadose zone contamination is a continuing source for ongoing and future contamination of groundwater. The U.S. Department of Energy and stakeholders alike have a strong interest in understanding and managing the risk posed by these contaminants.

There is significant uncertainty associated with the many factors that influence the movement of contaminants from waste disposal sites to the underlying aquifer. Uncertainties include sources (e.g., liquid volumes, composition, and the time-history of releases to waste disposal sites); physical and hydraulic properties of the heterogeneous sediments; and the transport, sorption, and reaction properties of the contaminants in the subsurface. In addition, external forcings on the system (e.g., recharge rates, flow directions, and hydraulic head gradients) are uncertain for past, present, and future conditions.

Truex et al. (2015a) performed screening analyses to illustrate the sensitivity of subsurface flow and transport model predictions to some of the factors noted above for the SX Tank Farm. Oostrom et al. (2017) performed similar screening analyses, but used field electrical resistivity survey results from Johnson and Wellman (2013) to infer the subsurface distribution of nitrate (NO_3^{2-}) contamination beneath the BY Cribs. Their results illustrated uncertainties in subsurface contaminant distributions on the predicted future transport of nitrate to groundwater. Truex et al. (2015b) performed illustrative simulations to demonstrate the sensitivity of contaminant transport from generic, hypothetical waste sites to various model input parameters and source release scenarios. They also outlined a framework for categorizing waste sites, based on the time-histories of contaminants observed in groundwater monitoring wells, to support remedy decisions.

The objective of the current work was to conduct an initial sensitivity analysis to illustrate how uncertainty in flow and transport model predictions is affected by different sources of uncertainty in model input variables for a tank farm complex, including source terms representing historical releases of contaminants to the subsurface. The B-Complex, located in the northern part of the 200 East Area of the Hanford Site, was used as a case study. The B-Complex is of particular interest because of its large scale and the number and complexity of its contaminant sources. The primary focus of the current work is on the influence of source term uncertainty on model output, but simulations were also performed to evaluate the sensitivity of model results to uncertainties in both sorption and hydraulic properties, including moisture-dependent anisotropy of unsaturated hydraulic conductivity. Model outputs of interest include Tc-99 flux to groundwater and Tc-99 concentrations in groundwater monitoring wells.

This report is organized as follows. Section 2 provides an overview of the Hanford B-Complex. The methods used to evaluate sensitivity of model results to different parameters are described in Section 3. Results and discussion are presented in Section 4. Conclusions are given in Section 5. Quality assurance is discussed in Section 6, and references are provided in Section 7. Details on the development of the subsurface flow and transport model that was used for this work are presented in Appendix A. Graphics illustrating the evolution of simulated plumes from different waste sites within the B-Complex for a baseline model are presented in Appendix B.

2.0 Site Description

Figure 2.1 is a map of the B-Complex showing key facilities, boreholes, and wells. The B-Complex contains the B-, BX-, and BY-tank farms. The 12 large single-shell waste storage tanks in each of the B- and BX-tank farms each have a 530,000 gal (2,003,400 L) capacity. The 12 large single-shell tanks in the BY-tank farm each have a 758,000 gal (2,865,240 L) capacity.

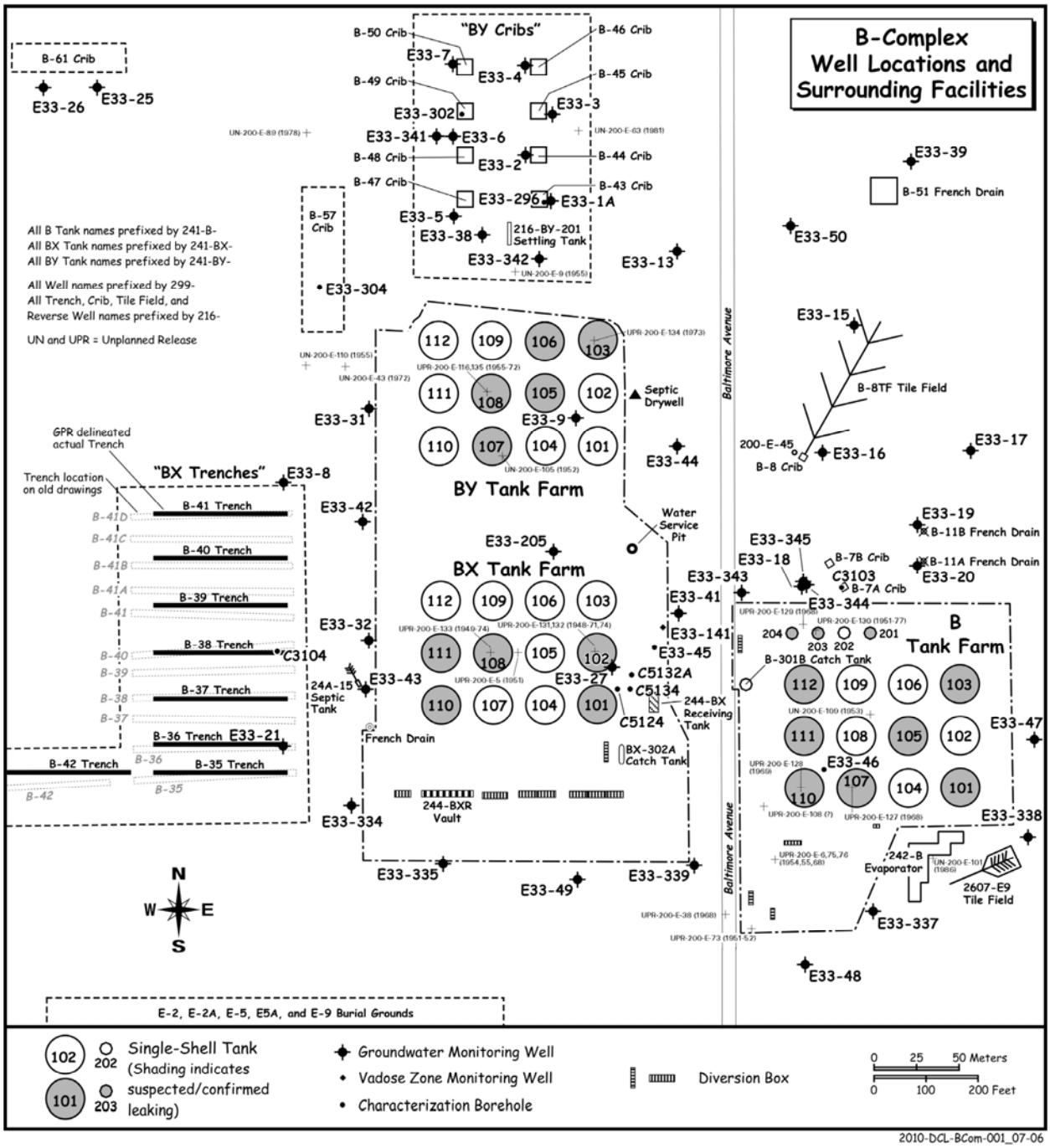

Figure 2.1. Map of the B-Complex Showing Key Facilities, Boreholes, and Wells (from Serne et al. 2010).

Several unplanned releases of wastes occurred during and after the filling of tanks in the B-Complex. The numerous cribs (e.g., BY Cribs), trenches (e.g., BX Trenches), tile fields, and French drains shown in Figure 2.1 were also used for intentional disposal of liquid wastes. An integrated assessment of the combined effects of uncertainties in hydraulic and transport properties, and waste disposal volumes/masses/activities to all known waste disposal sites in the B-Complex, on predictions of current and potential future groundwater contamination, is needed for remedy evaluation.

2.1 Hydrogeology

The generalized stratigraphy and major hydrostratigraphic units for the Hanford Site are shown in Figure 2.2. Surficial Holocene-age sediments are underlain by a thick sequence of unconsolidated sands and gravels of the Pleistocene-age Hanford formation (fm) that were deposited during a series of megafloods. The Hanford fm is underlain by the Pliocene-age Cold Creek Unit (CCU), which contains a silt-dominated subunit, CCUz, a caliche or carbonate-rich subunit, CCUc, and a gravel-dominated subunit, CCUg (Figure 2.2) (Hammond and Lupton 2015; Springer 2018). The CCU is underlain by various subunits of the semi-consolidated, Pliocene-age Ringold Formation, including the Taylor Flat member (Rtf), and the Unit E (Rwie), Lower Mud Unit (Rlm), and Unit A (Rwia) of the Wooded Island member (Figure 2.2). The combined Hanford and Ringold Formation constitute what is known as the supra-basalt aquifer system. The Ringold Formation is underlain by basalt of the Columbia River Basalt Group, which constitutes the basalt confined aquifer system.

Serne et al. (2010) provides a detailed description of the hydrogeology in the immediate vicinity of the B-Complex. Appendix A provides details on the Geologic Framework Model (GFM) for the region of interest in the current study. The current study used the Central Plateau Vadose Zone (CPVZ) GFM described by Springer (2018), in combination with the Hanford South GFM described by Weber (2018). In the CPVZ GFM, the Hanford fm is subdivided, from top to bottom, into H1, H2, and H3 subunits (Springer 2018). The Rtf and Rwie units are absent in the region of interest, and the Rlm unit is only found is a very small area in the southern part of the model domain (see Appendix A). Oostrom et al. (2013) subdivided the CCUz unit into upper and lower silts, separated by a thin sand, to account for local heterogeneities that result in a perched water zone under the B-Complex. The model developed for the current study also subdivided the CCUz unit in the same way. Further details on the GFM for the region of interest in the current study are provided in Appendix A.

Figure 2.3 is a cutaway view of the subsurface showing the hydrostratigraphic units and tanks of the B-BX-BY tanks farms. Similar figures are provided in the results and discussion section of this report, and in Appendix B, to show the evolution of simulated contaminant plumes over time. Estimates of physical, hydraulic, transport, and sorption parameters for the major hydrostratigraphic units and subunits are provided in Section 3 (see Table 3.1).

2.2 Liquid Effluent and Waste Release Estimates

Serne et al. (2010) compiled estimated liquid volume and contaminant mass/activity release information for waste sites in the B-Complex. Information from that report and references cited therein were used to construct source terms for the current study. Figure 2.4 shows a graphical representation of the estimated liquid volume release rates and time periods of operation for the majority of the sites where releases are known to have occurred. Figure 2.5, Figure 2.6, and Figure 2.7 show similar depictions of the release rates over time for Tc-99, NO_3, and total uranium, respectively, that were estimated for 36 sites. All of these sites were included in the model that was developed for this work. Estimated liquid effluent volumes and mass/activity of these and other species that were released from these sites are tabulated in Appendix A.

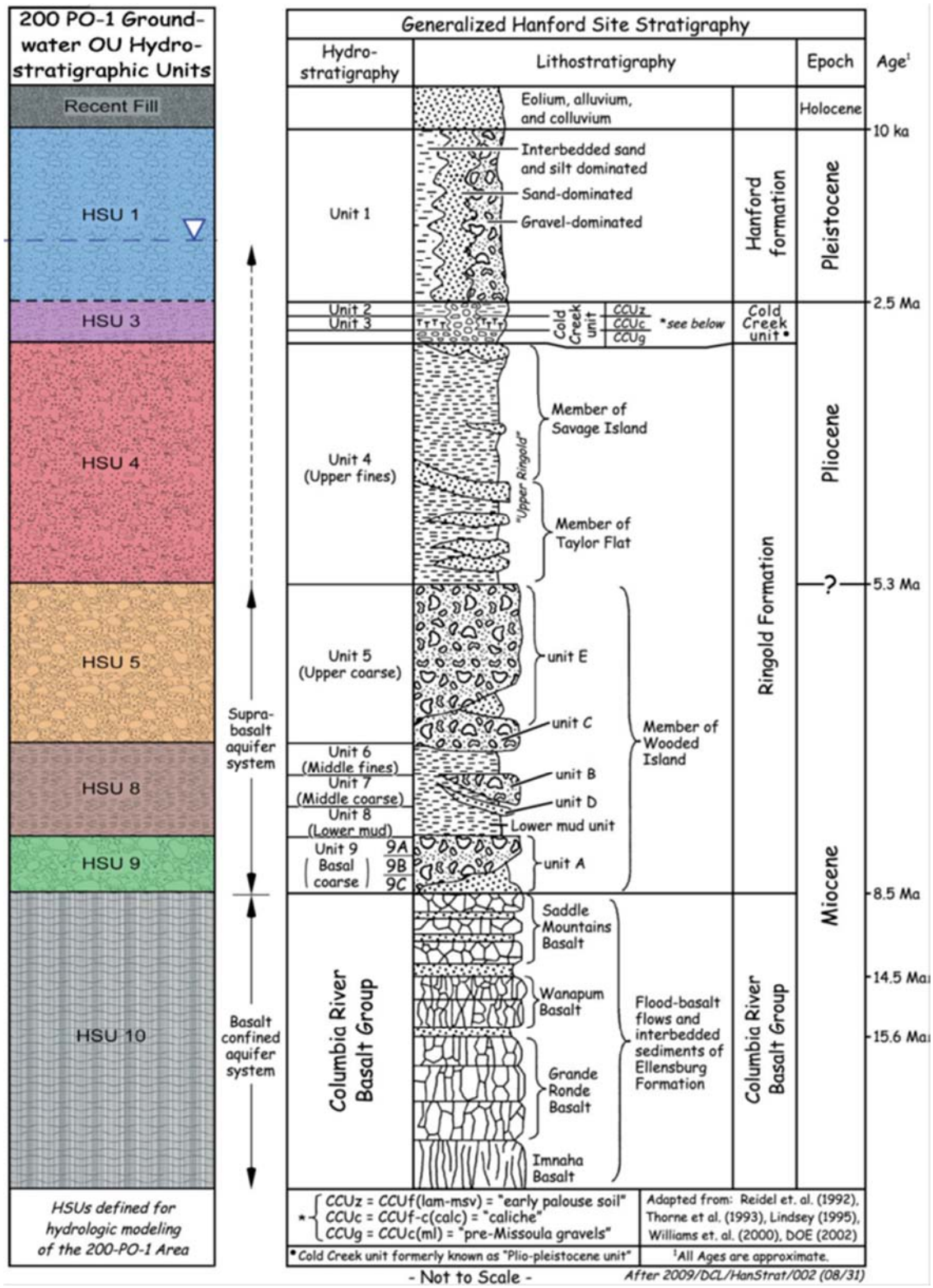

Figure 2.2. Hydrostratigraphic Units and Generalized Hanford Site Stratigraphy (from Hammond and Lupton 2015).

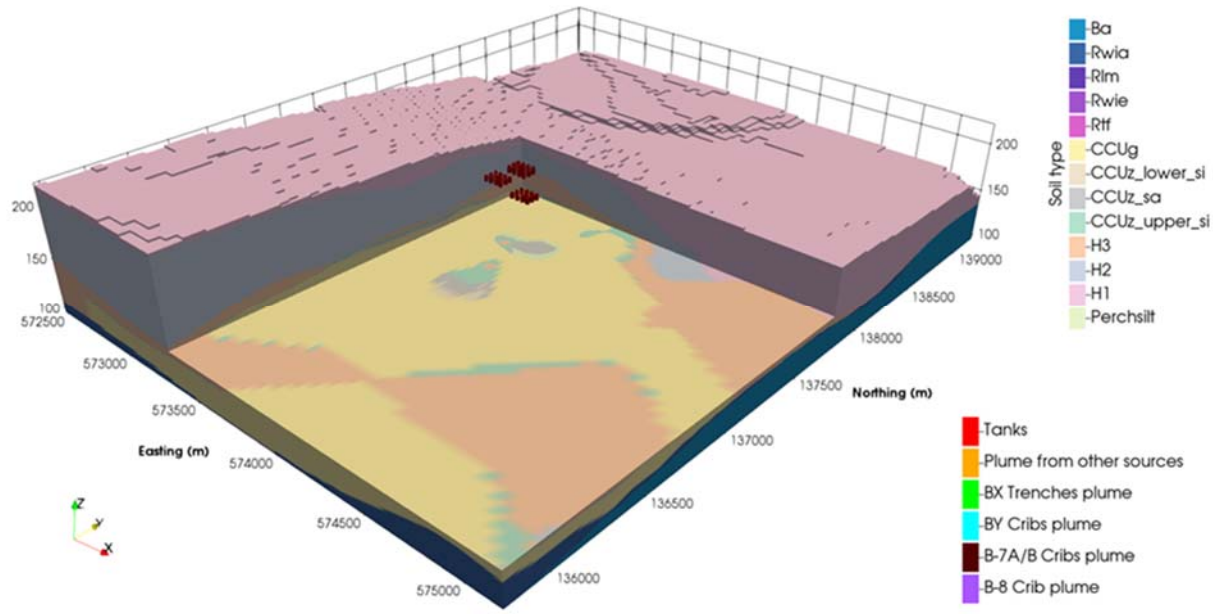

Figure 2.3. Cutaway View of Hydrostratigraphic Units Underlying the B-Complex Showing Waste Storage Tanks of the B-BX-BY Tank Farms.

Figure 2.4 through Figure 2.7 indicate that the largest estimated volumes of liquid and mass/activity of most contaminants released to the subsurface in the B-Complex were disposed of at the BY Cribs (216-B-43, -44, -45, -46, -47, -48, -49, and -50). As shown in Figure 2.7, site 241-BX-102 had the highest estimated release rates for total uranium. High levels of uranium and other contaminants have been found in a perched water zone that lies just north of the B-tank farm, and between the B- and BX-tank farms.

The estimates of liquid volumes and contaminant mass/activity released from B-Complex sources that were compiled by Serne et al. (2010) were based on results from the Hanford Waste Inventory Data System, and results compiled by Corbin et al. (2005) from the Hanford Soil Inventory Model (SIM). The SIM was used by the authors of that study to generate inventory and uncertainty estimates for 46 radionuclides and 29 chemicals using estimates of 196 waste streams applied to 377 liquid-waste disposal sites, unplanned releases, and tank leaks over their operating lifetimes, in intervals of 1 year, from 1944 to 2001. Appendix A of Corbin et al. (2005) provides summaries of the estimated liquid waste volumes and operating years for these disposal sites.

The radionuclide inventory of direct liquid discharges to soil in the Hanford 200 Areas has recently been updated (Zaher and Agnew 2018). This new information was not available in time to use for the current study, but the new inventory estimates will be reviewed and incorporated into future analyses for the B-Complex. Results of the current study are considered preliminary and For Information Only (FIO).

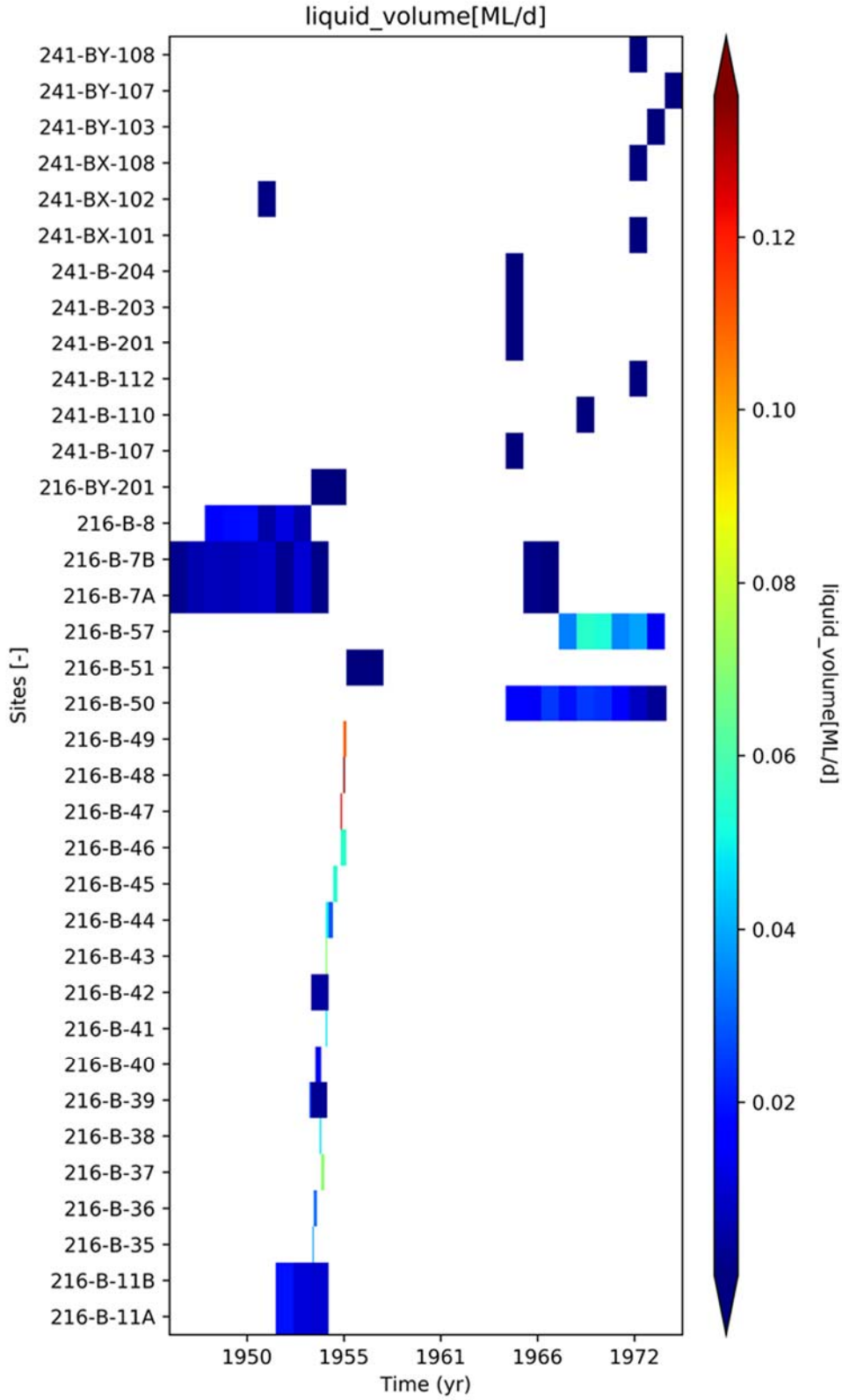

Figure 2.4. Estimated Liquid Effluent Discharge Rates Over Time for Waste Sites in the B-Complex.

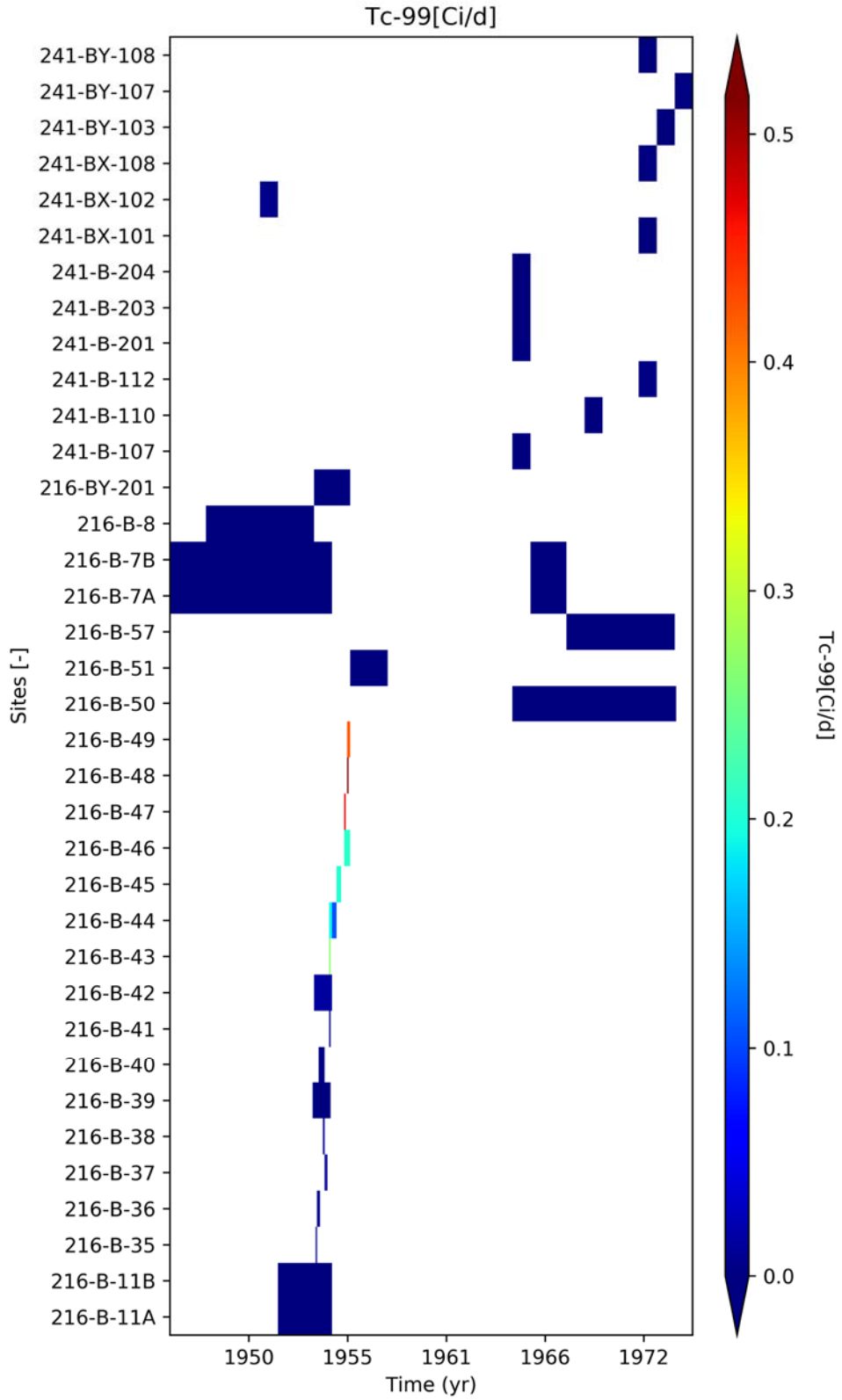

Figure 2.5. Estimated Tc-99 Release Rates Over Time for Waste Sites in the B-Complex.

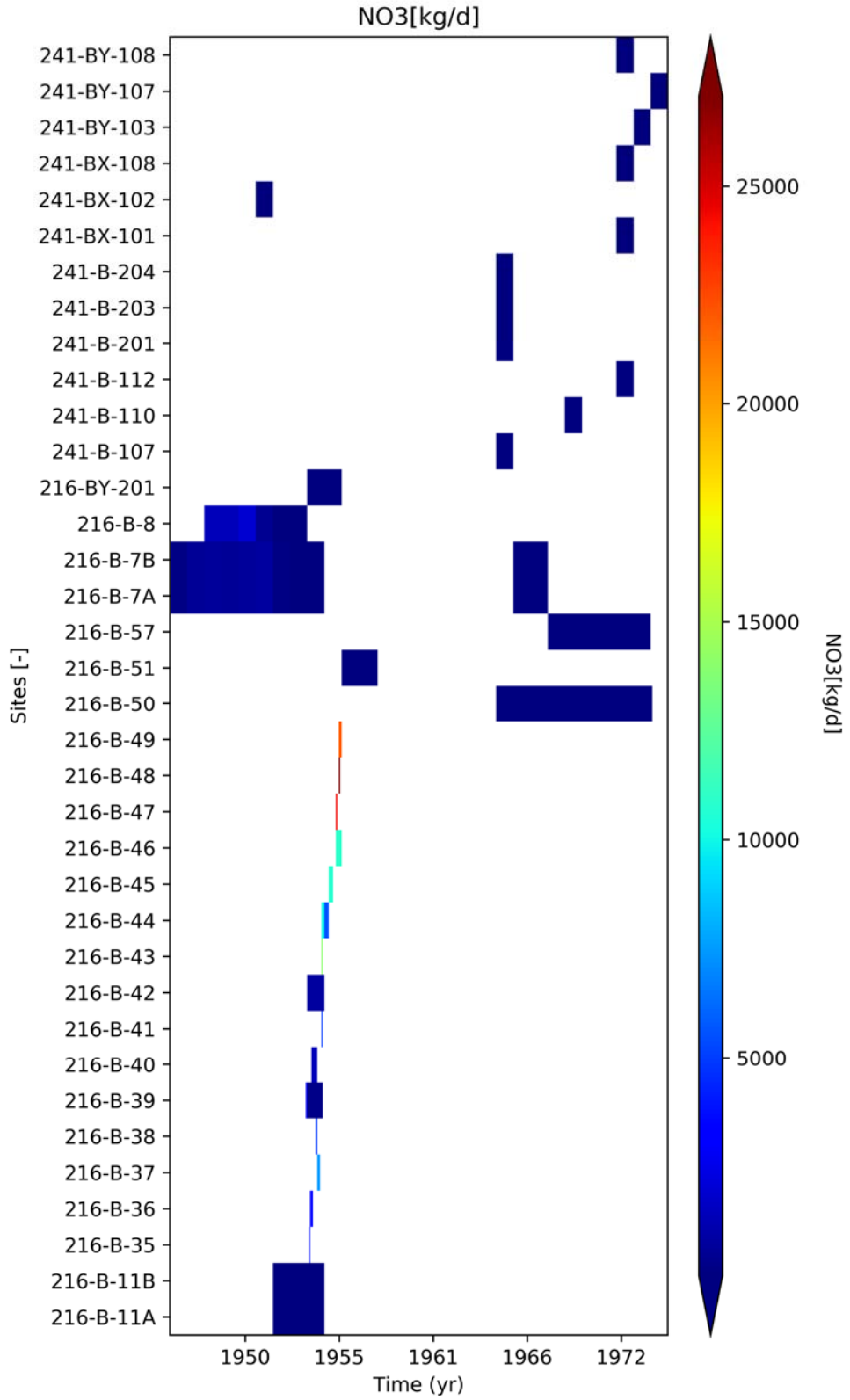

Figure 2.6. Estimated NO_3 Release Rates Over Time for Waste Sites in the B-Complex.

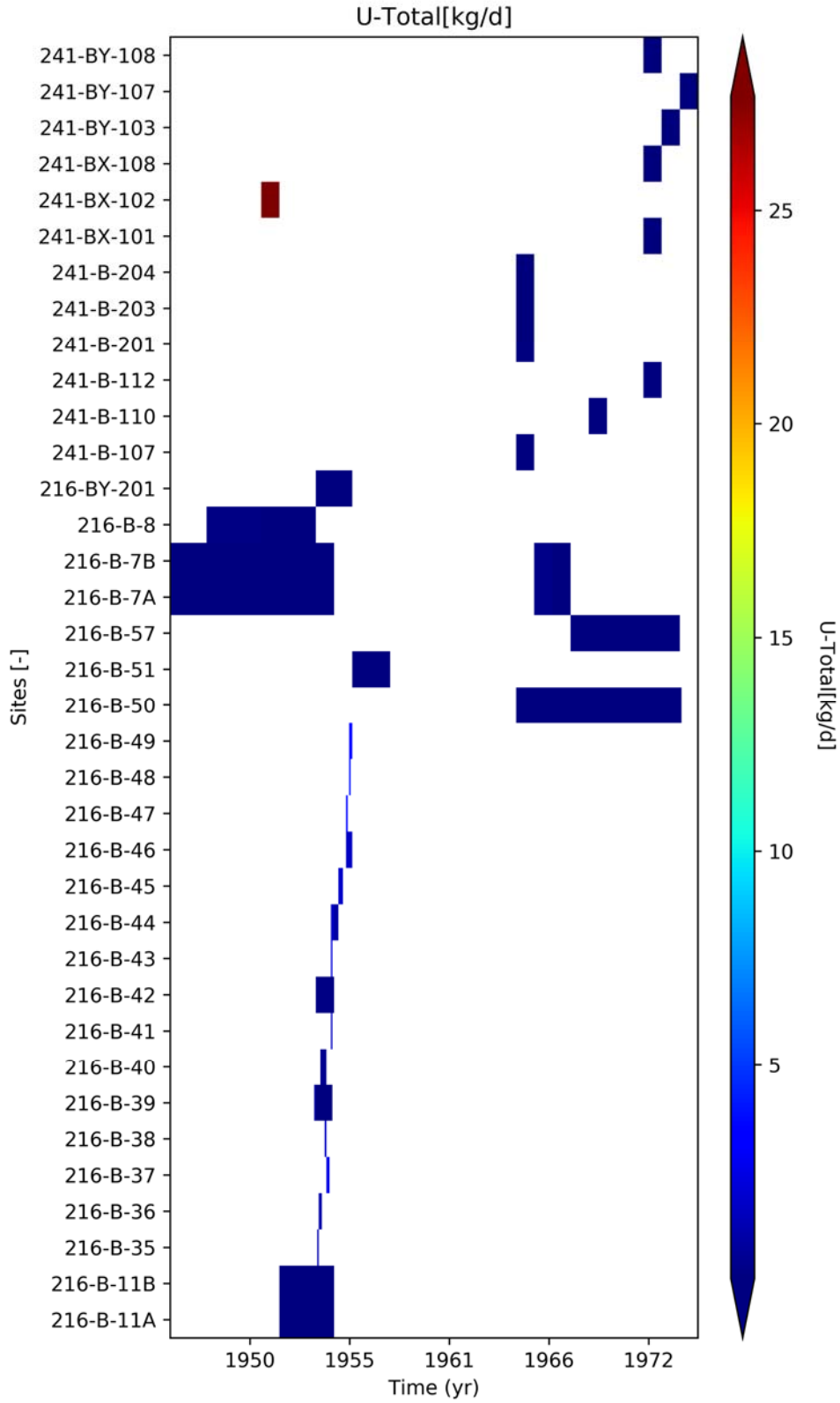

Figure 2.7. Estimated Total Uranium Release Rates for Waste Sites in the B-Complex.

3.0 Sensitivity Analysis Methodology

A brief review of sensitivity and uncertainty analysis is given in this section, followed by details of the methods used in the current study. Uncertainty analysis typically involves the demonstration of how uncertainties in model input variables propagate through to model outcomes or predictions, and the consequences of predictive uncertainty on decisions. Cole et al. (2001) provided an extensive review of uncertainty analysis methods and their application to Hanford site-wide groundwater flow and transport models. Sensitivity analysis can be defined as "*the study of how uncertainty in the output of a mathematical model or system can be apportioned to different sources of uncertainty in the inputs*" (https://en.wikipedia.org/wiki/sensitivity_analysis; last referenced 31-Aug-2018; Saltelli, 2002; Saltelli et al. 2008). Therefore, sensitivity analysis differs from uncertainty analysis in that it focuses on determining the relative sensitivity of model predictions to different, uncertain inputs.

Dai et al. (2017) describe a hierarchical, global sensitivity analysis method and its application to subsurface flow and transport modeling for a field experiment performed in the 300 Area of the Hanford Site. The method of Dai et al. (2017) was based in part on an uncertainty analysis framework described by Meyer et al. (2007, 2014). Figure 3.1a shows the framework of Meyer et al. (2007, 2014) with uncertainty divided into three categories: *scenario*, *model*, and *parameter*. Note that the general structure of the framework shown in Figure 3.1a was presented earlier by Kozak et al. (1993). In Figure 3.1, S, M, P, and C refer to Scenario, Model, Parameter, and Component, respectively. P1|M1 and P2|M2 refer to parameter set 1 applied to model 1, parameter set 2 applied to model 1, etc.

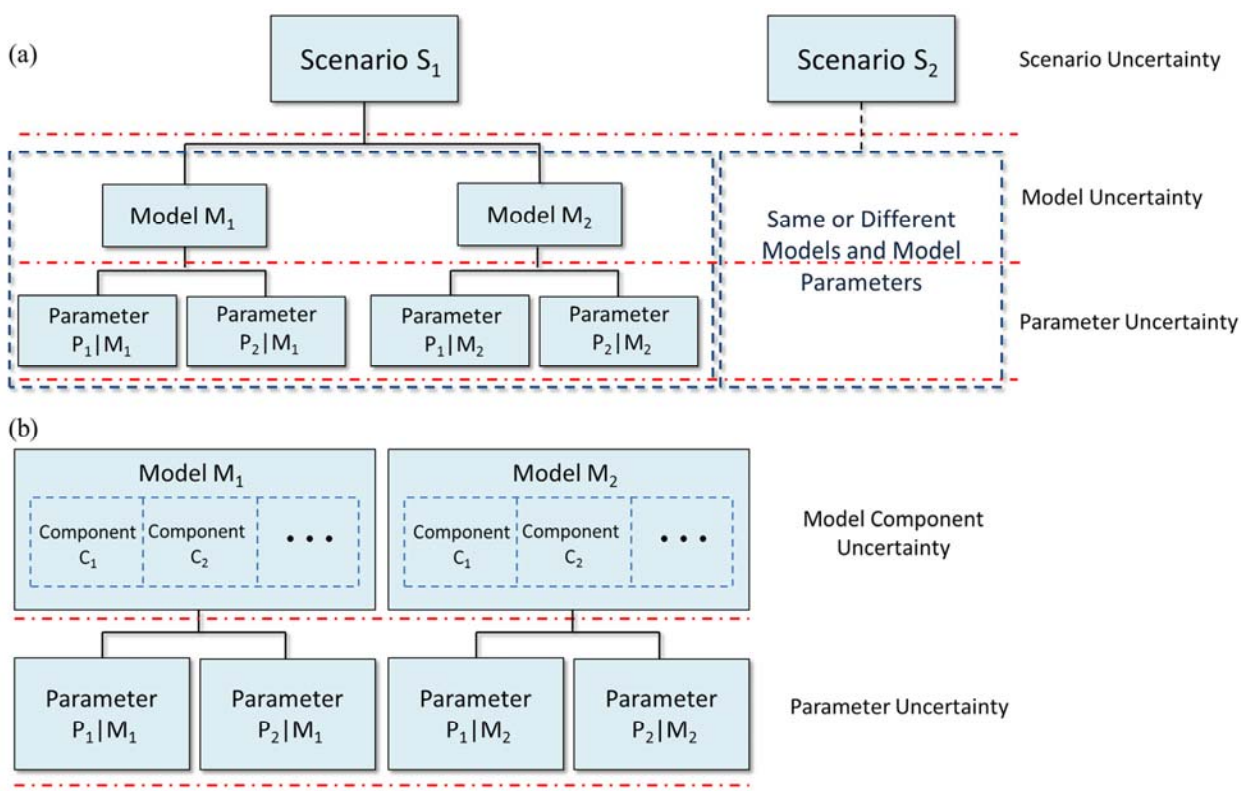

Figure 3.1. (a) Hierarchical uncertainty quantification framework, with (b) addition of multiple components included in model uncertainty (from Dai et al. 2017).

Scenario uncertainty is often used to refer to uncertainty in future conditions (Kozak et al. 1993) that affect external forcings on a model. For example, as the Earth's atmosphere warms and sea-ice melts, changes in precipitation patterns, recharge rates, and sea and groundwater levels are expected to occur. External forcings are usually represented in a model by boundary conditions.

Model uncertainty is typically used to refer to uncertainties associated with the structure of a model or the configuration of its features. For example, there may be uncertainty regarding whether the Hanford fm is best represented as a single, undifferentiated layer (Hammond 2017; Weber 2018), versus subdividing it into multiple layers (Springer 2018), facies, or other representations of heterogeneity (Rockhold et al. 2016). Model uncertainty, however, could also refer to alternative representations of processes that are represented mathematically in a model. For example, the process of "sorption" can be represented by a simple, linear equilibrium adsorption isotherm model (a.k.a. the K_d model), or by more complex kinetic multi-rate adsorption and surface complexation models that contain multiple parameters.

Parameter uncertainty typically refers to uncertainties in the parameters used in a particular process model, and/or to uncertainties in physical, chemical, or hydraulic properties/parameters that are assigned to material types in a model. For example, there may be significant uncertainty in hydraulic parameters such as saturated hydraulic conductivity, K_s, as well as K_d values that are used to represent sorption, due to the natural spatial variability of the sediments and sparse characterization data.

Dai et al. (2017) derived expressions for the total variance of model outputs resulting from uncertain inputs, and its decomposition into variances resulting from parameter, model, and scenario uncertainties. These variances were used to define sensitivity indices to measure the relative contribution of uncertainty from each category (i.e., scenario, model, and parameter). The Monte Carlo method was used in their study to evaluate the sensitivity indices, using 10,000 combinations of three input factors; i.e., 100 permeability field realizations, 10 alternative representations of boundary conditions, and 10 alternative representations of the surface representing the interface between the high-permeability Hanford fm and the lower-permeability Ringold Formation that underlies it. In their study, the sensitivity of hydraulic head predictions was shown to be dominated by uncertainties in boundary conditions, while the sensitivity of tracer concentration predictions was dominated by uncertainties in the permeability field.

The model developed for the current study represents a much larger spatial domain and much longer time periods than the model used in the example by Dai et al. (2017). Consequently, the model of the B-Complex area is much more computationally demanding and a simplified approach was necessary for the initial analyses. Instead of using multiple models, as depicted in Figure 3.1, a single model of the hydrogeologic system was developed based on the most current available hydrogeologic framework models for the Hanford Site and Central Plateau (Springer 2018; Weber 2018). The sensitivity of model results to uncertainties in hydraulic parameters, sorption parameters, and source terms for this layered model were evaluated qualitatively, with comparisons of simulation results to observed Tc-99 and NO_3 concentrations from groundwater monitoring wells. In this case, the use of different source terms is considered as alternative scenarios associated with uncertainties about disposal histories and inventories for waste sites (Figure 3.1a). Alternatively, source terms can also be categorized as model components (Figure 3.1b).

3.1 Hydraulic and Sorption Parameters

A baseline model configuration was first developed, based on best estimates of physical, hydraulic, and transport parameters, and source terms for a layered model of the subsurface (Serne et al. 2010; Oostrom et al. 2013, 2017). Simulations were performed with the baseline model, and with variations of the hydraulic and sorption parameters, applied separately, to qualitatively illustrate sensitivity of model

results to changes in these parameters. This approach is consistent with the types of screening analyses that have been reported previously by Truex et al. (2015a) for the SX Tank Farm, and by Oostrom et al. (2017) for the BY Cribs. However, in the current study there is more emphasis on comparing model results to groundwater monitoring data.

Table 3.1 lists physical, hydraulic, transport, and sorption parameters that were perturbed for modeling. Hydraulic and sorption parameters that were varied are indicated by the bracketed numbers, which are explained in the table footnotes. A complete set of parameters for all hydrostratigraphic units is given in Table A.1 (Appendix A). The vadose zone in the study area is dominated by the Hanford fm, so the effects of uncertainties in hydraulic and sorption properties for the H1, H2, and H3 units on model outputs were evaluated. The sensitivity of model results to uncertainties in source terms was also evaluated, as described in Section 3.2.

Hanford sediments tend to be anisotropic owing to their mode of deposition and non-spherical particle shapes. In laboratory characterization studies, hydraulic conductivity calculations are typically made for the vertical direction only, due to the vertical orientation of core samples. Therefore, moisture-dependent anisotropy can usually only be inferred from field observations and theoretical calculations (Rockhold et al. 2015). In contrast, aquifer characterization studies are usually targeted at determining hydraulic conductivity or transmissivity in the horizontal direction, owing to the use of wells for injection/ withdrawal/monitoring. Aquifer characterization studies tend to produce hydraulic conductivity values that are an order of magnitude or more greater than those determined on vertically-oriented core samples of the same formation. These differences can be attributed to anisotropy and scale effects, including potential bias associated with sampling of very coarse (gravel- and cobble-dominated) sediments with small-diameter core barrels. Aquifer characterization studies can provide information about anisotropy in saturated porous media (Rockhold et al. 2018), but provide no information about moisture-dependent anisotropy, since the porous media is saturated in an aquifer system.

Oostrom et al. (2017) suggested that after peak disposal periods from Hanford waste sites, the subsequent recharge-driven contaminant flux from vadose zone to the underlying aquifer is relatively insensitive to hydraulic properties. Moisture-dependent anisotropy was not explicitly considered in their study. For the current study, in addition to the perturbations of K_s and K_d noted in Table 3.1, the effects of anisotropy in both saturated and unsaturated hydraulic conductivity were also evaluated because lateral spreading can affect contaminant flux to the water table. Simulations were performed using baseline values of K_s shown in Table 3.1 for the vertical direction, but increasing the K_s values applied to the x- and y-directions by a factor of four (4X) for the H1, H2, and H3 subunits. In addition to anisotropy in K_s, the combined effects of anisotropy in K_s plus anisotropy in unsaturated hydraulic conductivity were evaluated using a tensorial connectivity-tortuosity (TCT) model (Zhang and Khaleel 2010; Rockhold et al. 2015). The TCT model parameters that were used are listed in Table 3.1.

New physical and hydraulic property characterization data and associated parameters were reported recently for some of the hydrostratigraphic units shown in Table 3.1 (Rockhold et al. 2018). Those results were recently released and were not available for use in the current study. However, the parameters in Table 3.1 are still considered to be reasonable estimates based on parameters reported previously by Oostrom et al. (2013, 2017) and references cited therein. Hoffman (1992) reports values of K_s for core samples from the 200-BP-1 operable unit in the vicinity of BY Cribs that range from 2.1e-6 cm/s to 7.4e-2 cm/s, which provides some basis for the ranges of K_s values shown in Table 3.1.

Table 3.1. Hydraulic and Sorption Parameters that were Varied for Model Simulations of Subsurface Flow and Transport for the Hanford B-Complex Area.

Unit	*Ks* [(a)] [cm/s]	*ℓ* [(b)]	K_d –Tc-99 [(c)] [cm³/g]	K_d – NO_3 [(c)] [cm³/g]
H1	6.65e-4 [K_s*0.01, K_s*1000]	0.5 [-0.683, 0.916]	0 [0.0, 1.0]	0 [0.0, 1.0]
H2	2.27e-3 [K_s*0.01, K_s*1000]	0.5 [-0.683, 0.916]	0 [0.0, 1.0]	0 [0.0, 1.0]
H3	6.65e-4 [K_s*0.01, K_s*1000]	0.5 [-0.683, 0.916]	0 [0.0, 1.0]	0 [0.0, 1.0]

(a) Numbers in brackets are lower and upper limits for K_s. Six values were evaluated: 0.01*K_s, 0.1*K_s (baseline), K_s, 10*K_s, 100*K_s, 1000*K_s.

(b) Baseline model used 0.1*Ks and constant value of pore interaction term, ℓ=0.5. Alternative cases used 0.1*Ks and TCT model of moisture-dependent anisotropy (Zhang and Khaleel 2010), with ℓxx = ℓyy = -0.683, and ℓzz=0.916. These values represent an intermediate level of anisotropy for sandy sediments (Rockhold et al. 2015).

(c) Values in brackets indicate lower and upper Kd limits used in simulations, based on Serne (2007). Eleven Kd values were evaluated over this range (inclusive), in increments of 0.1 cm3/g.

3.2 Source Terms

The quasi-Monte Carlo method was used to generate 200 alternative realizations of source terms representing uncertainty in both liquid volumes and contaminant masses/activities discharged to the 36 waste sites represented in this study. The stated uncertainties in the reported liquid waste volumes for sites in the B-Complex range from 10% to 50% (Corbin et al. 2005). The higher end of this range (50%) was used as a conservative estimate of the uncertainty in both liquid discharge volumes and mass/activity released for the current study. Figure 3.2 shows a representation of the perturbations that were generated for liquid volume using the quasi-Monte Carlo sampling method.

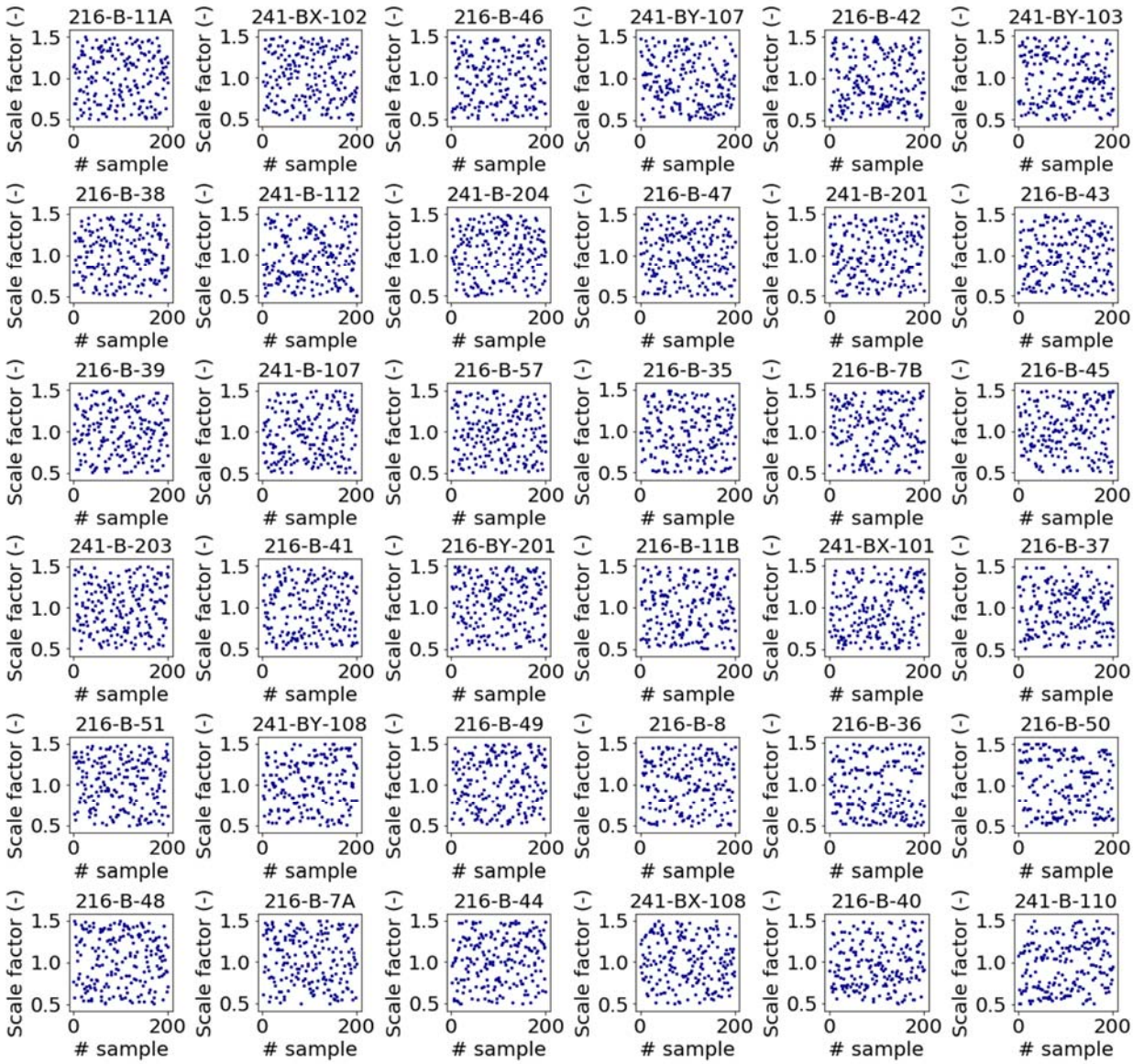

Figure 3.2. Realizations of Liquid Disposal Volume Perturbations for B-Complex Waste Sites Generated Using the Quasi-Monte Carlo Method.

The liquid waste volumes and mass or activity for each contaminant in the baseline model were scaled (range: 0.5 – 1.5) to account for their assumed uncertainty. The alternative realizations generated for mass/activity released (not shown) were independent of the generated liquid volumes. Constant values of the hydraulic, transport, and sorption parameters for the baseline case were used with the alternative realizations of the source terms. Appendix A lists the baseline estimates of liquid waste and species masses or activities that were released over time. It is important to note that uncertainties in the time histories of discharges to the waste sites were not considered in the current study.

4.0 Results and Discussion

Simulations were run from year 0 to 2100. The timeframe from year 0 to 1943 was a spin-up period to achieve an initial steady state. Figure 4.1 and Figure 4.2 show snapshots of simulation results from the baseline model for 1956 and 2018, respectively, showing isosurfaces (1 pCi/L) of simulated Tc-99 plumes representing different source areas, and the locations of tanks, superimposed on a cutaway view of the hydrostratigraphy. Tc-99 from different grouped sites was labeled separately in these figures to illustrate the origin of the subsurface contamination. Tc-99 pools in the perched water aquifer region. Additional snapshots of Tc-99 plume isosurfaces from the baseline model are provided in Appendix B.

Model simulation results are presented and discussed in this section by category of parameter, which can be grouped into 1) Hydraulic Parameters (K_s and moisture-dependent anisotropy), 2) Sorption Parameters (K_d), and 3) Source Terms. In all cases, simulated and observed concentrations of Tc-99 and NO_3 are compared for groundwater monitoring wells located within the B-Complex. Well locations are shown in Figure 2.1. Simulated concentrations are flux-averaged values over the screened interval for each well. Observed concentrations were obtained from the Hanford Environmental Information System (HEIS) database. Transport of uranium was also modeled but results for simulated versus observed concentrations of uranium are not shown owing to additional complexities associated with interpreting some of the analytical data for different uranium isotopes reported in HEIS. All results presented here are FIO.

4.1 Sensitivity of Groundwater Concentrations to Hydraulic Parameters

Figure 4.3 and Figure 4.4 show observed concentrations over time for Tc-99 and NO_3, respectively, at the selected monitoring wells, and simulation results for cases in which the K_s values for the three subunits of the Hanford fm (H1, H2, and H3) were varied as shown in the legend of these figures. The sorption parameters were held constant at $K_d = 0$ cm^3/g for all of these simulation cases. Relatively few groundwater monitoring data are available for wells in the B-Complex for early (pre-1980s), and intermediate times (1980-2000), especially for Tc-99. Reducing the K_s value delays the arrival of Tc-99 and NO_3 from the source areas to the monitoring well locations, as expected, bringing the model results closer to the field observations at later times. For some wells, a larger value of K_s produces a better match to the field data (e.g. 299-E33-21, 299-E33-43), which may reflect spatial variability that is not well represented by a layered model, and/or inaccuracies in source terms. The observed Tc-99 and NO_3 data appear to behave similarly for most of the wells, but overall, the correspondence between simulated and observed results is better for Tc-99 than for NO_3. Both solutes were modeled as conservative and non-reactive for this group of simulations, so differences in closeness of model results to field observations may be partially attributable to sorption or other transformations of NO_3 occurring in the field that are not accounted for in the model. Differences may also be due to uncertainty in source terms.

Figure 4.5 and Figure 4.6 show observed concentrations over time for Tc-99 and NO_3, respectively, at the selected monitoring wells, and simulation results for cases in which variables affecting the anisotropy of hydraulic properties for the three subunits of the Hanford fm (H1, H2, and H3) were varied. The sorption parameters were again held constant at $K_d = 0$ cm^3/g for this group of simulations. Increasing anisotropy of hydraulic conductivity in the vadose zone has a similar effect to decreasing K_s, of delaying the arrival of contaminants at the groundwater monitoring wells. It is difficult to discern from the simulation results which, if any, of the variations provide better or closer overall matches to the field observations. Models using the baseline K_s values tend to overpredict observed concentrations more often than not for both contaminants and particularly for NO_3. Cases using $0.01*K_s$ tend to underpredict observed concentrations

for both contaminants, especially for Tc-99. Therefore values of 0.1*K_s (with no TCT model and no anisotropy in K_s) were chosen for subsequent models for the Hanford fm subunits.

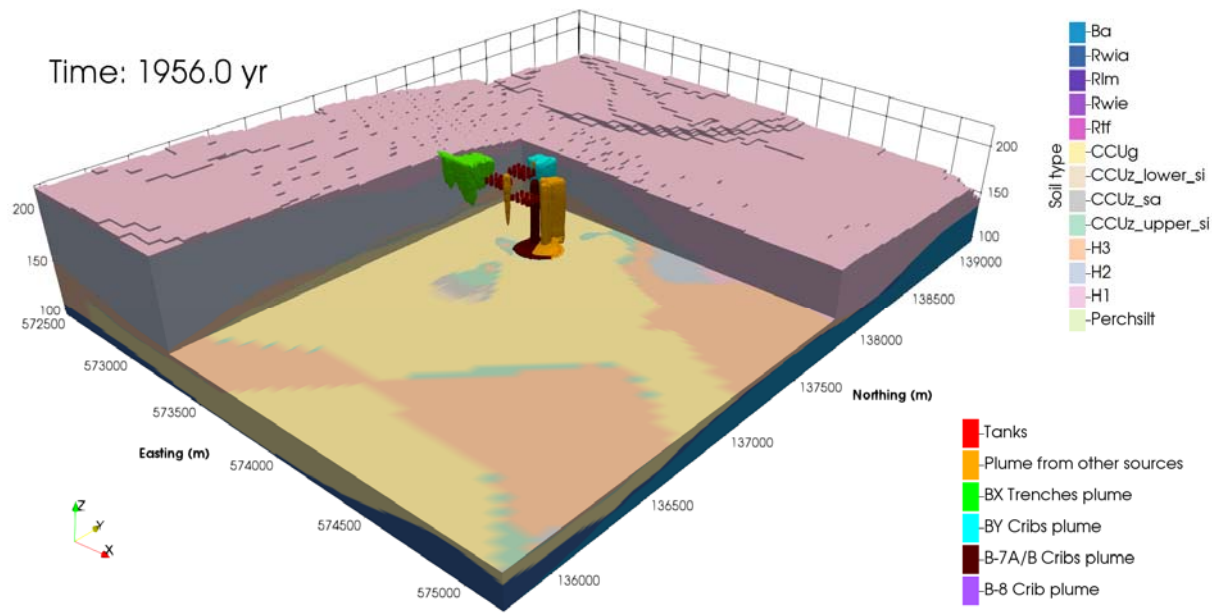

Figure 4.1. Simulated Tc-99 Isosurfaces [1 pCi/L] for Baseline Model in 1956 Showing Tanks of the B-BX-BY Tank Farms and a Cutaway View of Hydrostratigraphic Units Underlying the B-Complex. FIO.

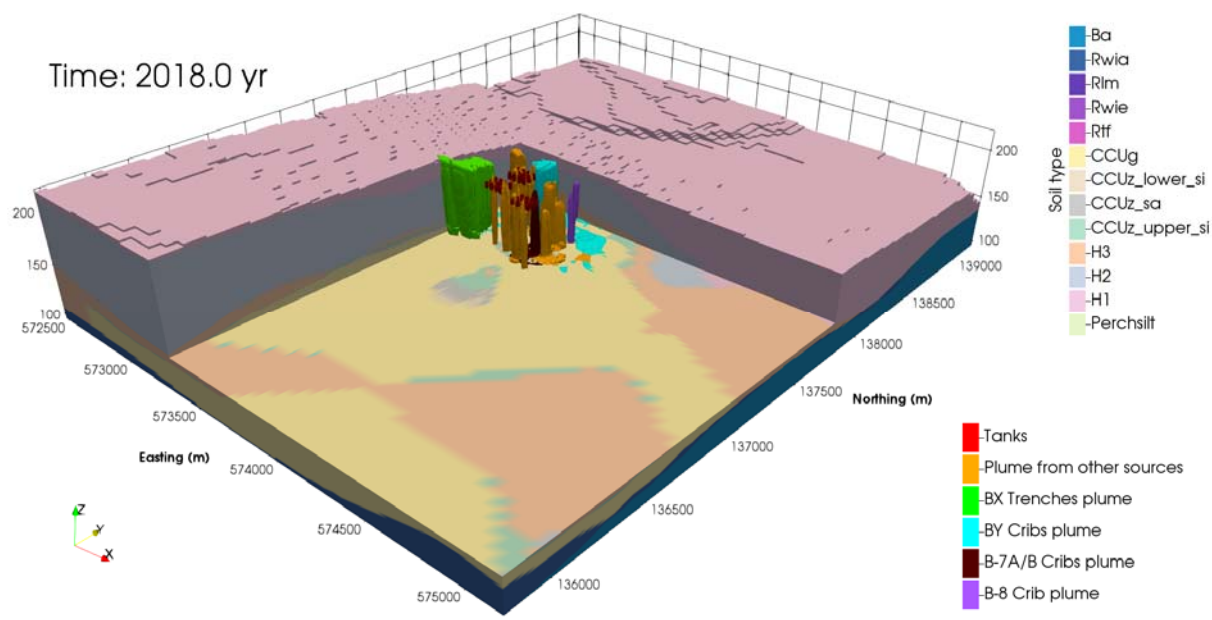

Figure 4.2. Simulated Tc-99 Isosurfaces [1 pCi/L] for Baseline Model in 2018 Showing Tanks of the B-BX-BY Tank Farms and a Cutaway View of Hydrostratigraphic Units Underlying the B-Complex.

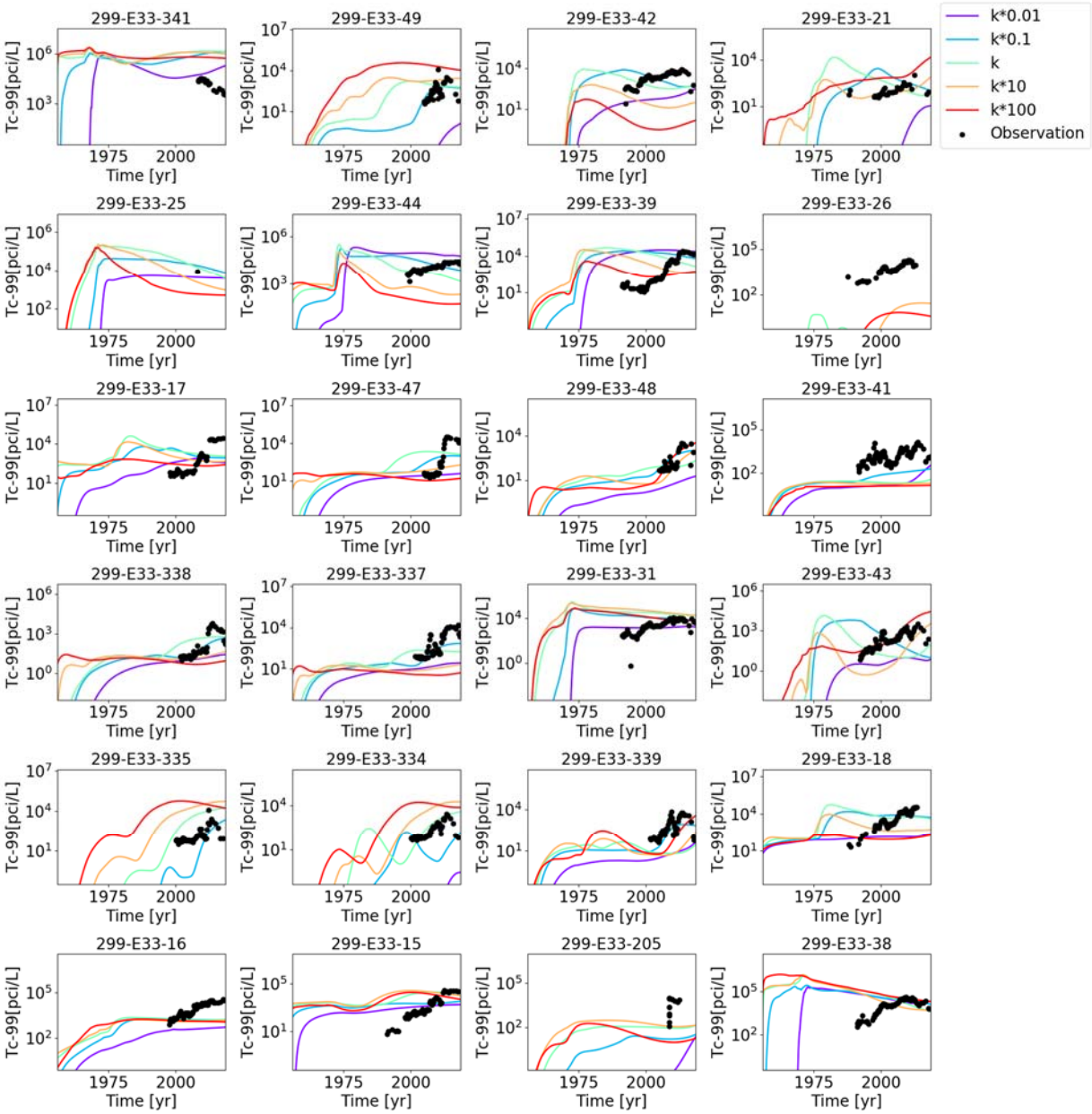

Figure 4.3. Observed Concentrations of Tc-99 from Groundwater Monitoring Wells in the B-Complex and Simulation Results Illustrating the Sensitivity of Results to Uncertainties in K_s for the Hanford fm. The K_s values listed in Table 3.1 for the H1, H2, and H3 subunits were scaled as shown for the different simulation cases.

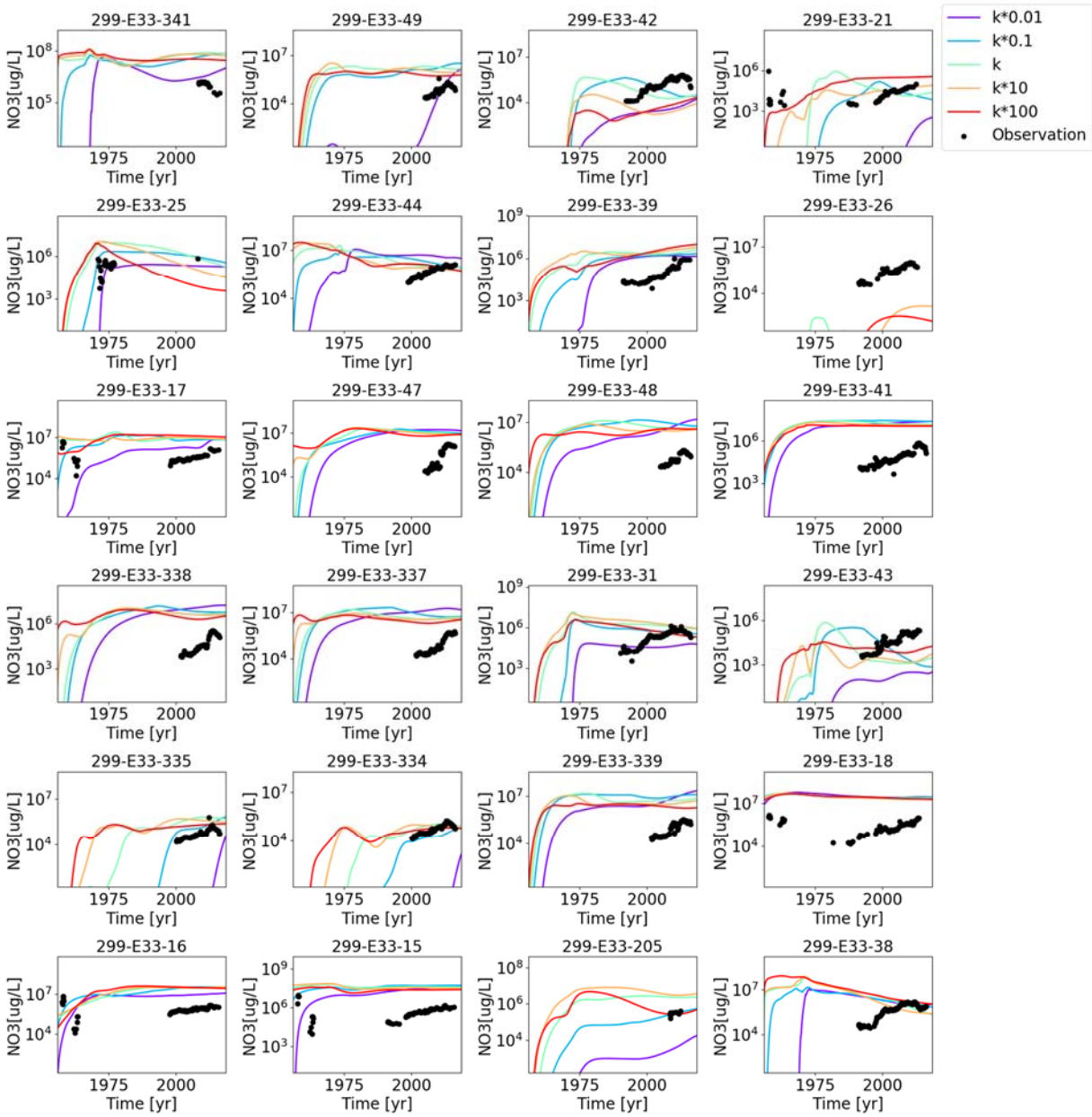

Figure 4.4. Observed concentrations of Nitrate from Groundwater Monitoring Wells in the B-Complex and Simulation Results Illustrating the Sensitivity of Results to Uncertainties in K_s for the Hanford fm. The K_s values listed in Table 3.1 for the H1, H2, and H3 subunits were scaled as shown for the different simulation cases.

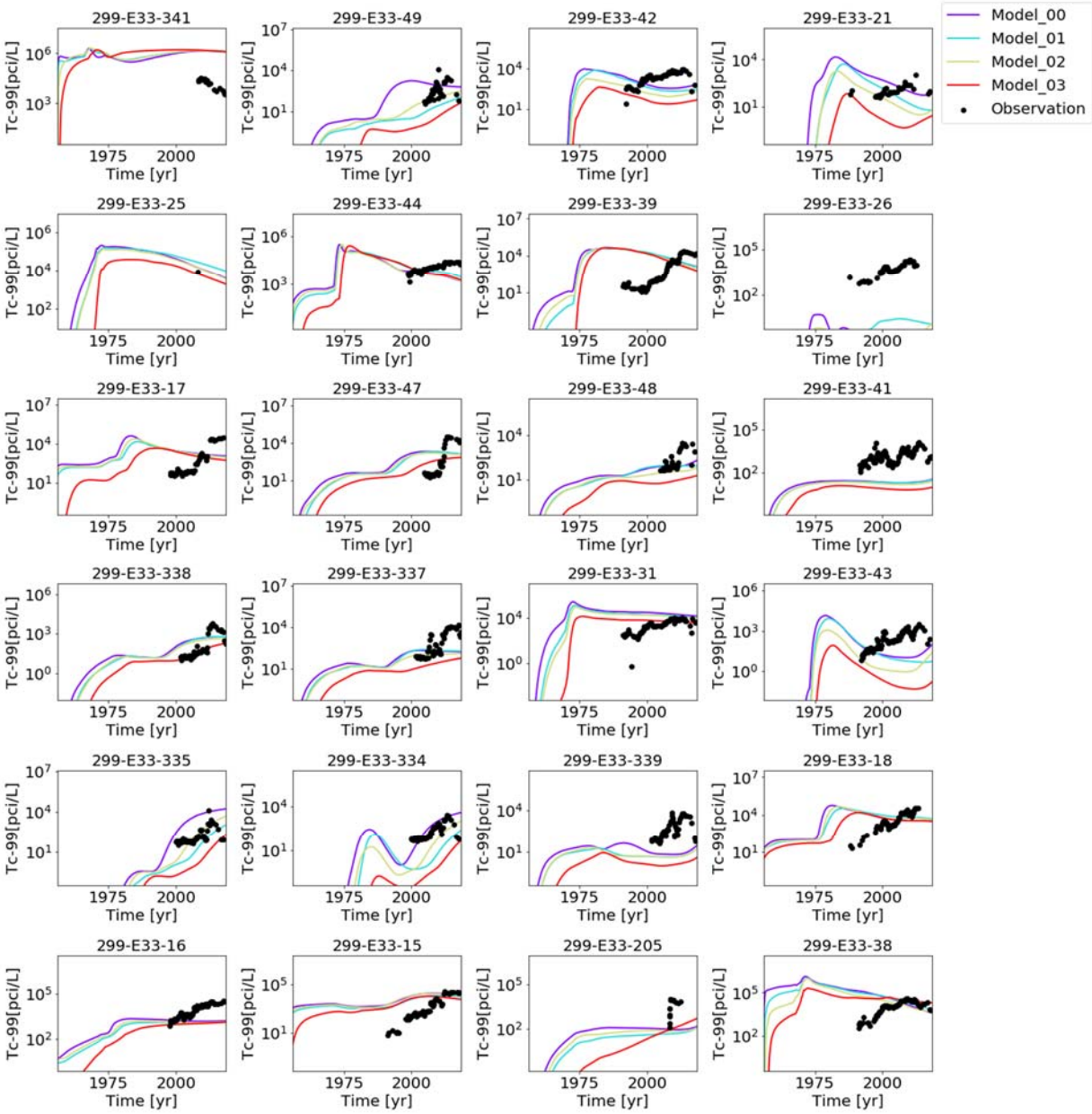

Figure 4.5. Observed Concentrations of Tc-99 from Groundwater Monitoring Wells in the B-Complex and Simulation Results Illustrating the Sensitivity of Model Results to Uncertainties in the Anisotropy of Hydraulic Properties in the Hanford fm. Model_00 represents parameters from Table 3.1. Model_01 represents the TCT model for moisture-dependent anisotropy. Model_02 represents anisotropy in K_s only with $K_{xx}=K_{yy}=4*K_{zz}$. Model_03 represents the changes used in Model_01 and _02 combined. Values of $0.1*K_s$ were used as baseline parameters for all subsequent model simulations.

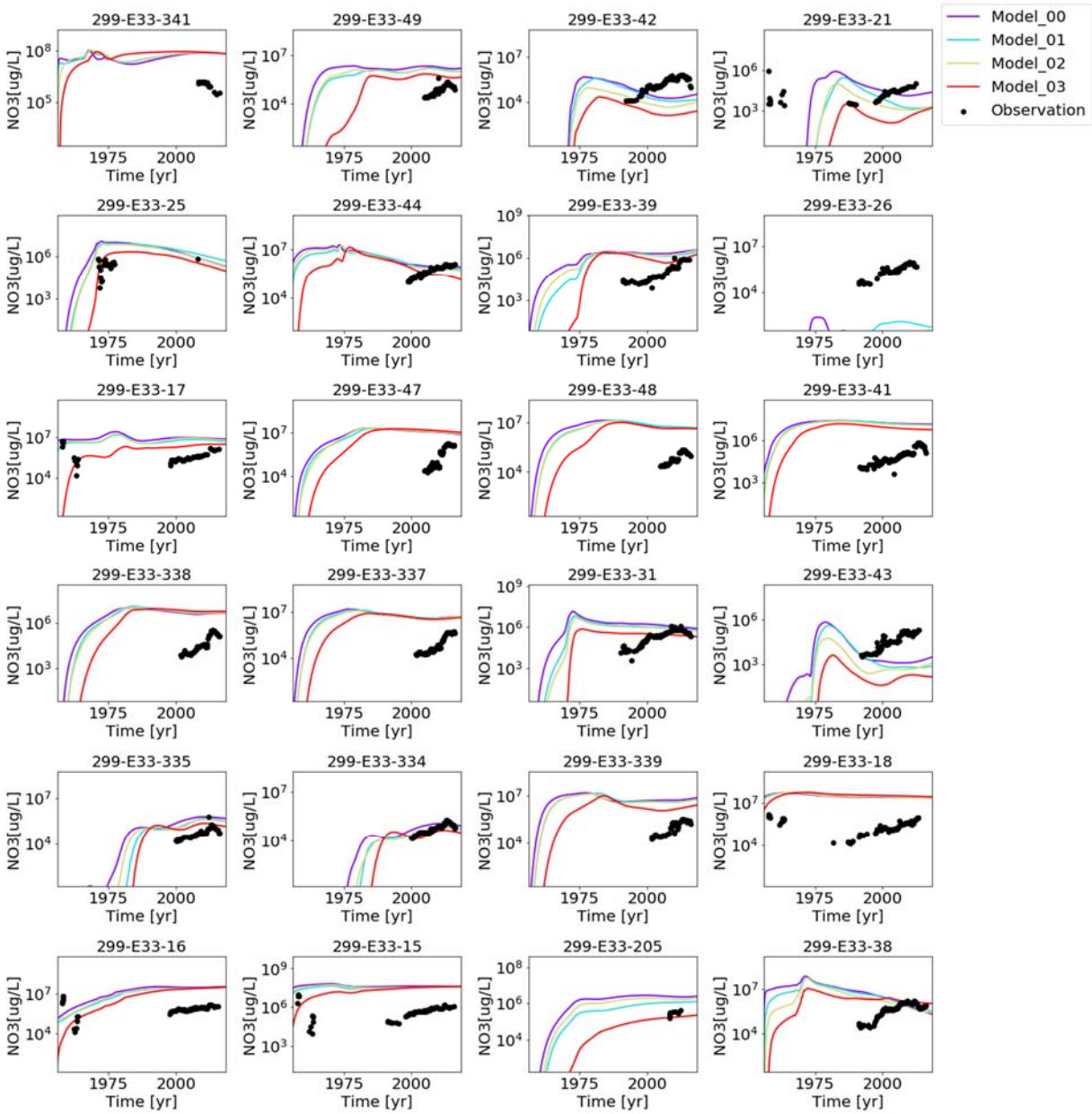

Figure 4.6. Observed Concentrations of Nitrate from Groundwater Monitoring Wells in the B-Complex and Simulation Results Illustrating the Sensitivity of Model Results to Uncertainties in the Anisotropy of Hydraulic Properties in the Hanford fm. Model_00 represents parameters from Table 3.1. Model_01 represents the TCT model for moisture-dependent anisotropy. Model_02 represents anisotropy is K_s only with $K_{xx}=K_{yy}=4*K_{zz}$. Model_03 uses the parameters from Model_01 and _02 combined. Values of $0.1*K_s$ were used as baseline parameters for all subsequent model simulations.

4.2 Sensitivity of Groundwater Concentrations to Sorption Parameters

Figure 4.7 and Figure 4.8 show observed concentrations over time for Tc-99 and NO_3, respectively, at the selected monitoring wells, and simulation results for cases in which K_d values were varied for the three subunits of the Hanford fm (H1, H2, and H3). The ranges used for the K_d values are based on Serne (2007). The hydraulic properties were held constant for these simulation cases at the baseline values.

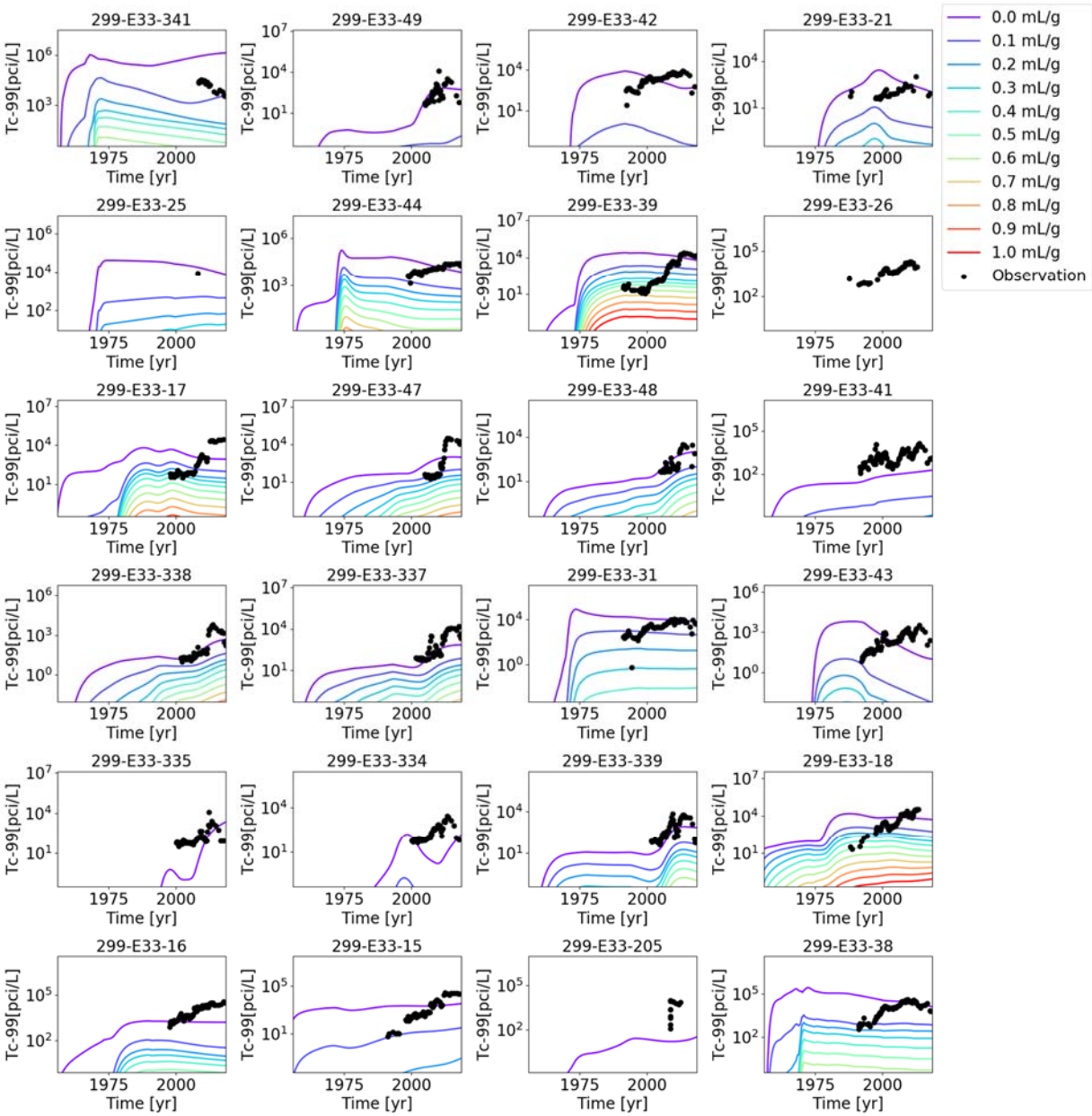

Figure 4.7. Observed Concentrations of Tc-99 from Groundwater Monitoring Wells in the B-Complex and Simulation Results Illustrating the Sensitivity of Model Results to Uncertainties in K_d for the Hanford fm.

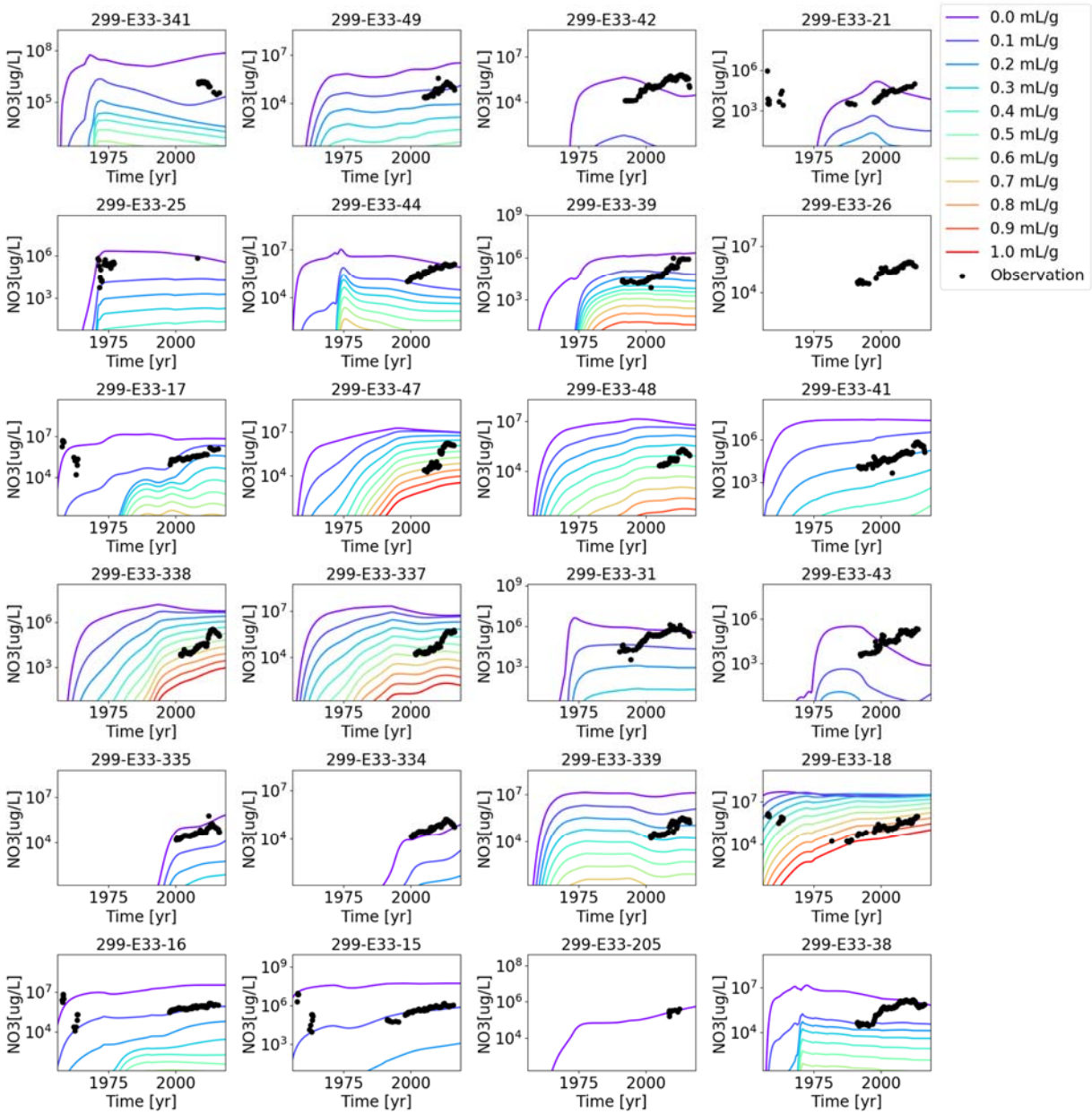

Figure 4.8. Observed Concentrations of Nitrate from Groundwater Monitoring Wells in the B-Complex and Simulation Results Illustrating the Sensitivity of Model Results to Uncertainties in K_d for the Hanford fm.

The lower end of the K_d range is typical of what is expected for native Hanford sediments that have very low organic matter content. The upper end may be more representative of values that might develop if the liquid wastes contained dissolved organic matter that sorbs with contaminants and binds with the sediment, or if Hanford sediments were used for future agricultural purposes (Serne 2007). A value of $K_d = 0$ cm^3/g provides the closest correspondence to measured Tc-99 concentrations for the majority of the selected groundwater monitoring wells. In contrast, non-zero but small K_d values appear to provide better matches to measured nitrate concentrations for about half of the selected wells. Over the ranges of

the parameters that were evaluated, simulated Tc-99 and nitrate concentrations qualitatively appear to be more sensitive to sorption (K_d) than to hydraulic properties (K_s and anisotropy).

4.3 Sensitivity to Groundwater Concentrations to Source Terms

Figure 4.9 and Figure 4.10 show observed concentrations over time for Tc-99 and NO_3, respectively, at the selected monitoring wells, and simulation results for 200 realizations of the model source terms. Sorption parameters were held constant at $K_d = 0$ cm^3/g and hydraulic parameters were fixed at their baseline values for this group of simulations. The spread of simulated concentration curves resulting from uncertainties in source terms overlaps the Tc-99 field observations for the majority of the wells.

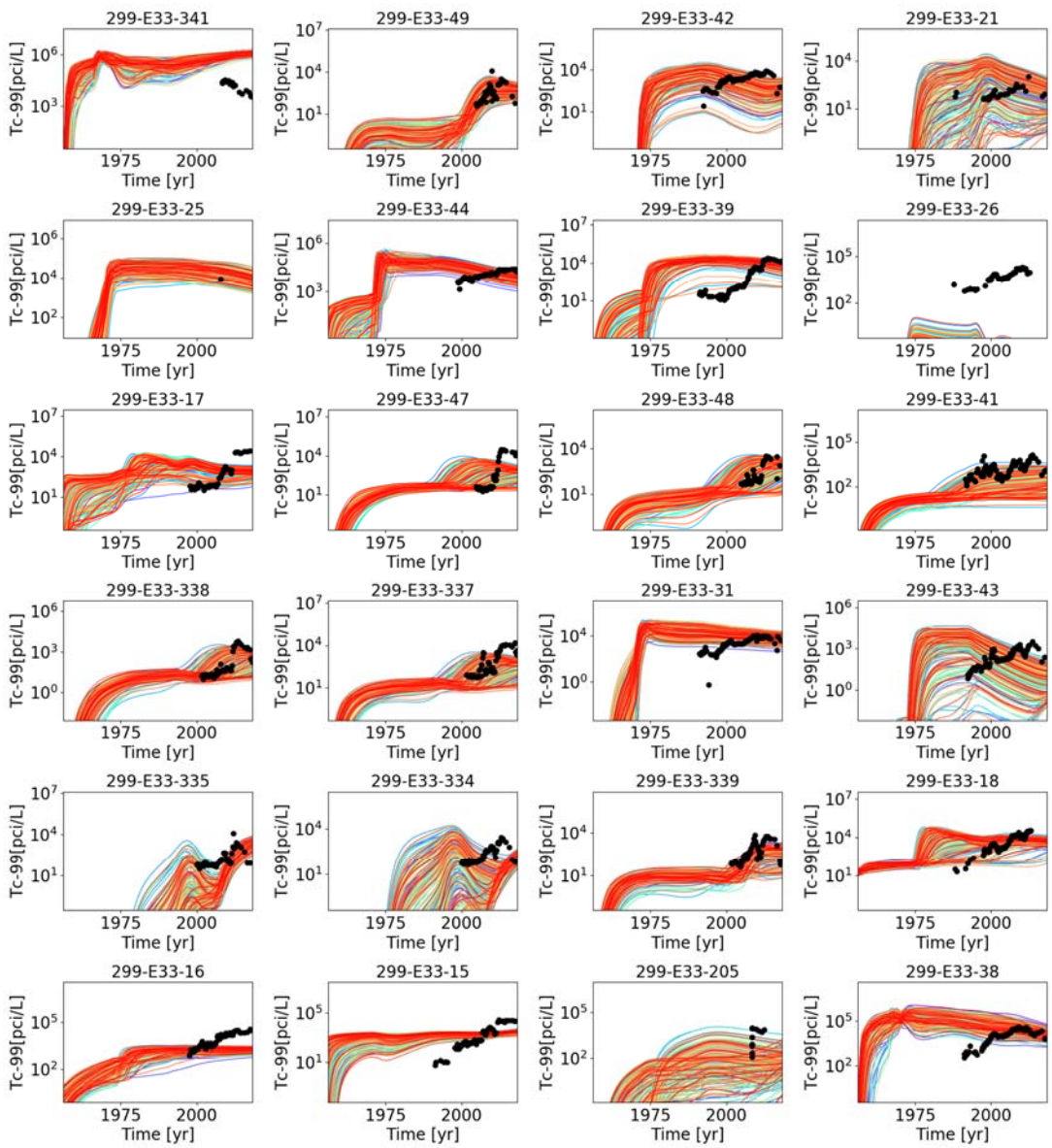

Figure 4.9. Observed Concentrations of Tc-99 from Groundwater Monitoring Wells in the B-Complex and Simulation Results for 200 Realizations Illustrating the Sensitivity of Predicted Concentrations to Uncertainties in Source Terms.

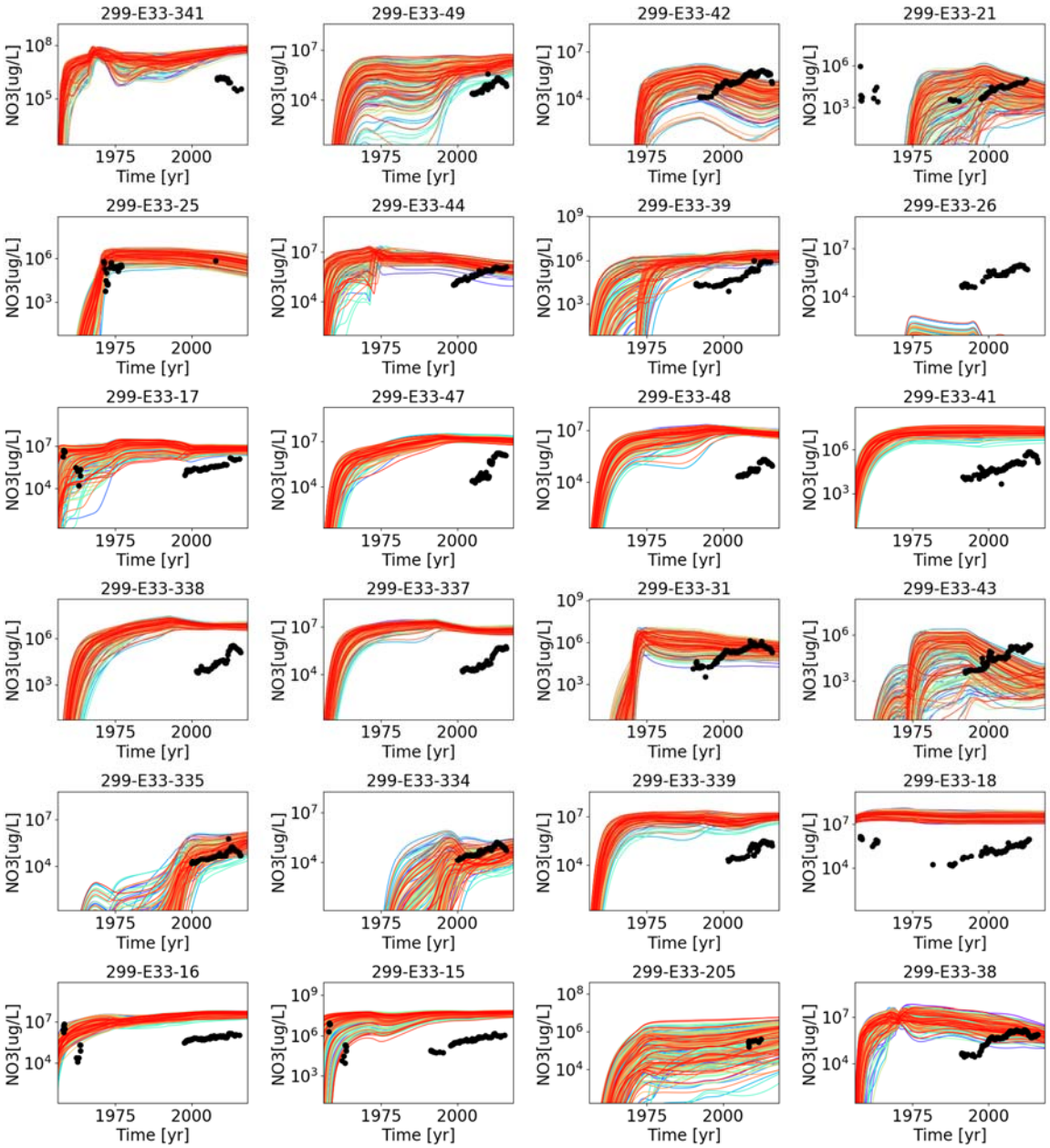

Figure 4.10. Observed Concentrations of Nitrate from Groundwater Monitoring Wells in the B-Complex and Simulation Results for 200 Realizations Illustrating the Sensitivity of Predicted Concentrations to Uncertainties in Source Terms.

Relatively few data are available for early and intermediate times to assess whether or not multiple peaks in groundwater concentrations have occurred from liquid waste discharges in the B-Complex. However, based on the few wells where early time data are available (e.g., 299-E33-15, 299-E33-16, 299-E33-17, 299-E33-18, 299-E33-21), and more recent data for the majority of the wells, it does look like multiple peaks might have occurred, or are still in the process of occurring. In most cases, the observed concentrations for both Tc-99 and NO_3 over the last 20 years or so are trending upward, although concentrations do appear to be declining in recent measurements from some of the wells. The trends of the simulation results are similar to observations for some wells (e.g., 299-E33-335, 299-E33-334), but not for others (e.g., 299-E33-26). Differences between simulated and observed concentrations are greater

for NO_3 than for Tc-99 for most, but not all, wells. The spread of the simulated concentration curves resulting from the modeled uncertainty in source terms appears to be less than that generated from the modeled uncertainty in hydraulic and sorption parameters for many of the wells.

Differences between observed and simulated concentrations may be due in part to several factors that were not accounted for in the current model. For example, if the baseline source terms and their potential uncertainty are relatively accurate, the differences in simulated versus observed groundwater concentrations could result, in part, from lateral spatial variability of sediment physical and hydraulic properties that is not represented in a layered model. This could potentially include differences in the permeability of sediments in the bottom of trenches and cribs resulting from accumulation of colloidal material, sedimentation, and/or precipitation reactions. Spatial variability in hydraulic properties such as this could account for the sensitivity analysis results that show decreasing K_s values lead to improved correspondence between observed and simulated results for some wells, while increasing K_s values leads to improved results for other wells. No attempt was made to assess the sensitivity of model results to other physical and hydraulic properties such as porosity and water retention parameters. Some information to assess the potential spatial variability and uncertainty of sediment properties is available through site geophysical well logging records, and in physical and hydraulic property characterization data that are tabulated in several reports (Hoffman 1992; Serne et al. 2010; Rockhold et al. 2018). On the other hand, inaccuracies in the time-histories of liquid volume discharges and contaminant mass/activity released to different sites could also account for some of these differences. Zaher and Agnew (2018) recently published revised estimates of radionuclide inventories for direct liquid discharges to soils in the 200 Areas. These results were not available in time to use for the current study, but will be considered in future analyses.

Another factor that was not accounted for is uncertainty in groundwater elevations, flow directions, and gradients. The water table in the 200 East Area has been notoriously flat in recent times, which has led to significant uncertainty regarding flow directions and gradients. The regional water table elevation in the area of interest has been declining, which reduces the saturated thickness of the unconfined aquifer. This will potentially result in changes in flow directions and gradients, and will affect the concentration trends in wells, since groundwater and associated contaminants are forced into a thinner portion of the unconfined aquifer. Oostrom et al. (2017) performed simulations of transport through the vadose zone to the water table at BY Cribs. Their model did not include the underlying aquifer, so they performed mixing model calculations to illustrate the effects of reducing the saturated thickness of the unconfined aquifer on groundwater concentrations. In the current study, an integrated model of the combined vadose zone-aquifer system was used, and time-dependent lateral boundary conditions were used that are based on field measurements of water levels in monitoring wells from the HEIS database. Model results also represent flux-averaged concentrations over the screened intervals for the monitoring wells. Therefore, the effects of the declining water table should be well represented by the model used in the current study. However, as shown by Dai et al. (2017), given the sparse nature of water level monitoring data, spatial variability, and the need for interpolation, there can still be significant uncertainty in gradients and flow directions computed from water level data that are used to define boundary conditions.

4.4 Sensitivity of Fluxes from Vadose Zone to Groundwater to Hydraulic Parameters, Sorption Parameters, and Source Terms

A flux plane was specified across the entire plan-view extent of the model domain, at the 122 m elevation, to compute volumetric flow rates and flux-averaged concentrations leaving the vadose zone and entering the aquifer over time. The elevation of 122 m was selected to represent the approximate elevation of the water table in recent times.

The convention used for computing flow rates and fluxes in the exascale Subsurface Transport Over Multiple Phases (eSTOMP) simulator is that positive values indicate movement in the direction of increasing elevation (upward) and negative values indicated movement in the direction of decreasing elevation (downward).

Figure 4.11 shows simulated aqueous volumetric flow rates, and flux-averaged NO_3, Tc-99, and total uranium concentrations crossing the 122 m elevation over time for different values of K_s. Recall that the K_d values and source terms were held constant for these simulations. The water table elevation at the site has varied significantly over time, with water levels rising during the active discharge periods, and falling after the cessation of active discharges. This is reflected in the positive values shown in Figure 4.11 for computed aqueous volumetric flow rates at early times, and negative values at later times. The time-histories of flux-averaged concentrations show a series of spikes that result from waste discharges to the different sites at different times, and water table fluctuations. The results in Figure 4.11 are consistent with the observations of Oostrom et al. (2017) that flux to groundwater is more sensitive to uncertainties in hydraulic properties at early times, during and shortly after active discharge periods, relative to at later times when flux is controlled primarily by the recharge rate.

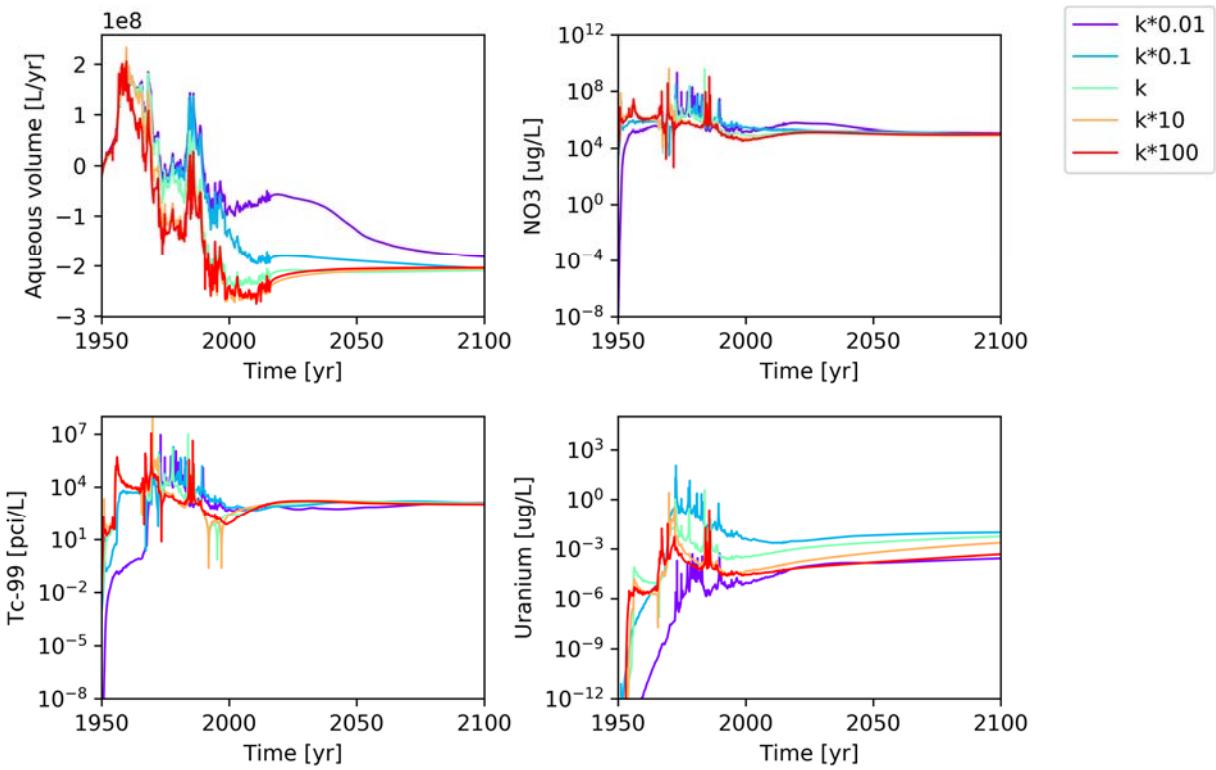

Figure 4.11. Simulated Aqueous Volumetric Flow Rates, and Flux-Averaged NO_3, Tc-99, and Total Uranium Concentrations Crossing the 122 m Elevation Over Time for Different Values of K_s.

Figure 4.12 shows simulated aqueous volumetric flow rates, and flux-averaged NO_3, Tc-99, and total uranium concentrations crossing the 122 m elevation over time for different representations of anisotropy in hydraulic properties. K_d values and source terms were held constant for these simulations. Note that some of the spikes in flux-averaged concentrations shown previously for Tc-99 in Figure 4.11 are modulated or smoothed in Figure 4.12 as a result of lateral spreading of the simulated plumes. This is especially evident for Model_03, which includes anisotropy in K_s as well as anisotropy in unsaturated hydraulic conductivity generated using the TCT model (Zhang and Khaleel 2010; Rockhold et al. 2015).

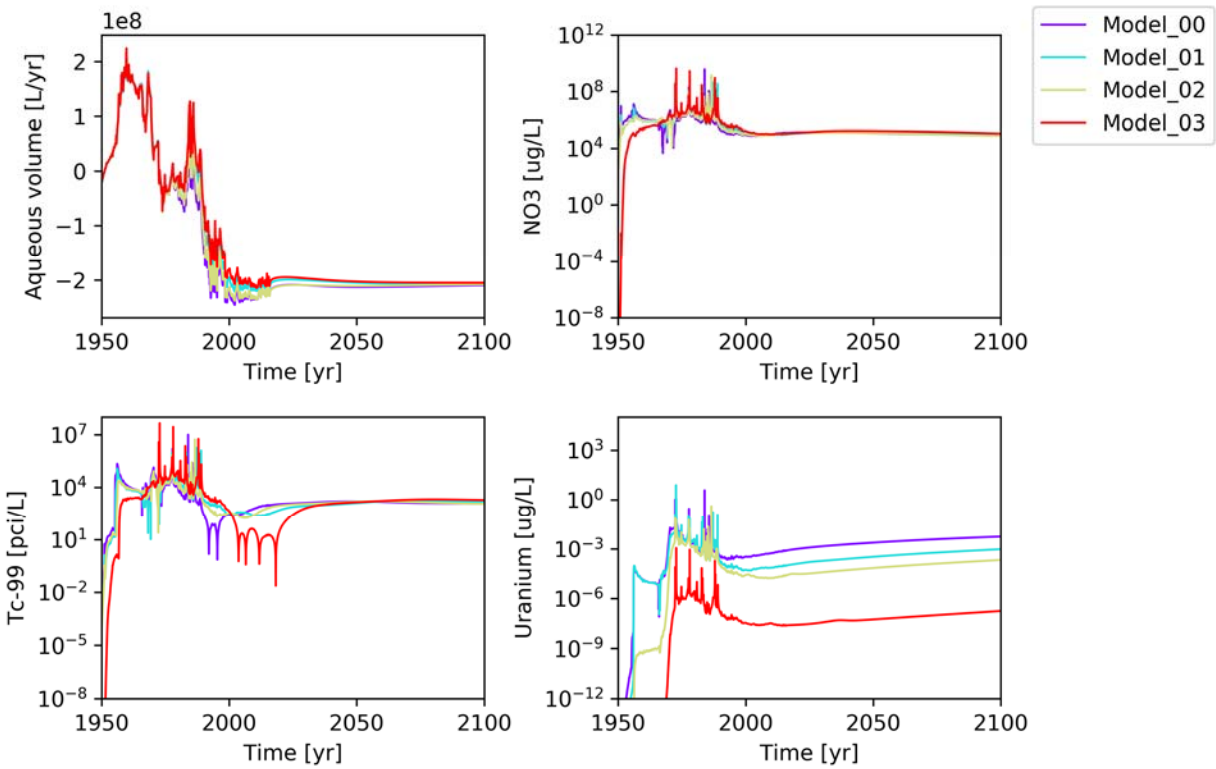

Figure 4.12. Simulated Aqueous Volumetric Flow Rates, and Flux-Averaged NO_3, Tc-99, and Total Uranium Concentrations Crossing the 122 m Elevation Over Time for Different Cases of Anisotropy. Model_00 represents parameters from Table 3.1 (isotropic). Model_01 represents the TCT model for moisture-dependent anisotropy. Model_02 represents anisotropy in K_s only with $K_{xx}=K_{yy}=4*K_{zz}$. Model_03 represents the changes used in Model_01 and _02 combined.

Figure 4.13 shows simulated aqueous volumetric flow rates, and flux-averaged NO_3, Tc-99, and total uranium concentrations crossing the 122 m elevation over time for different values of K_d. Values of 0.1*K_s (with K_s from Table 3.1) were used as baseline parameters for these and subsequent simulations. The hydraulic properties and source terms were held constant for these simulation cases, and the K_d value for uranium was fixed at K_d = 0.8 cm^3/g. Therefore, the plots for aqueous volumetric flow rates and uranium concentrations over time show no variability. However, the variability in the time series for simulated flux-averaged NO_3 and Tc-99 flux-averaged concentrations for different values of K_d is significant. As mentioned earlier, the lower K_d values are representative of Hanford sediments with very low organic matter content. The higher K_d values may be more representative of liquid wastes containing dissolved organic matter or colloidal material that sorbs with contaminants and binds with the sediment.

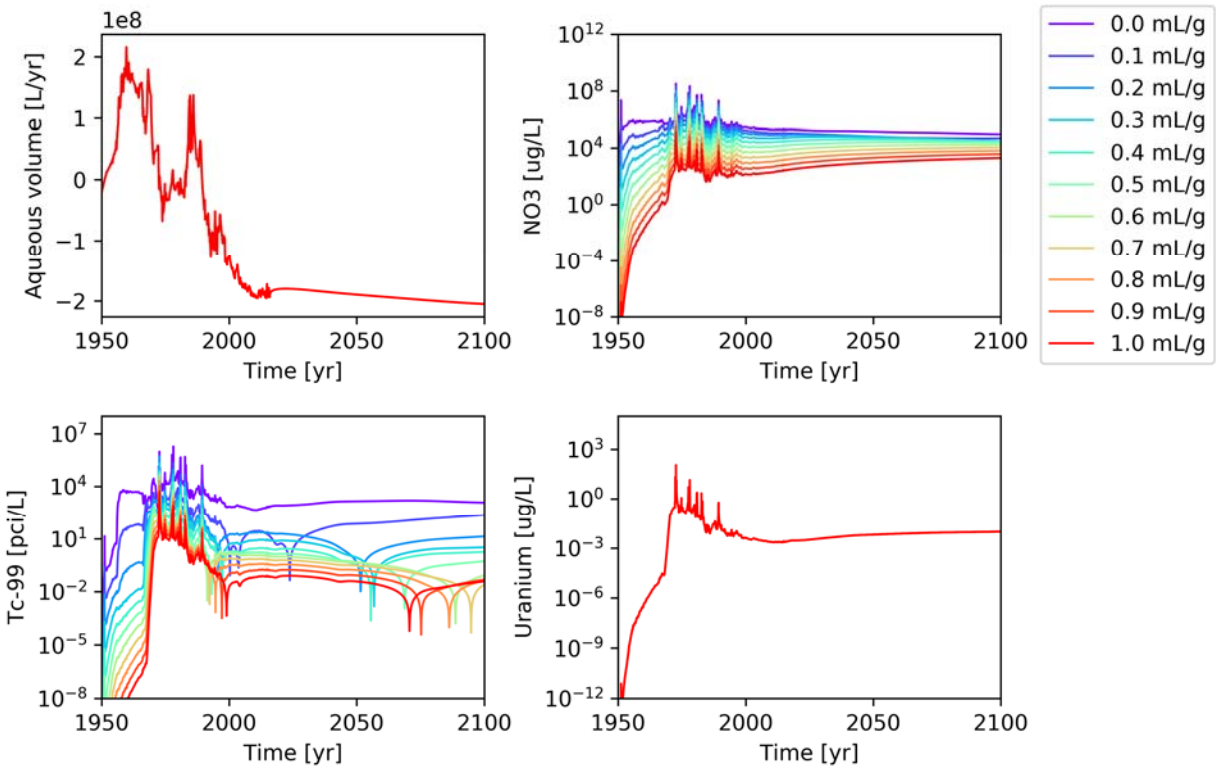

Figure 4.13. Simulated Aqueous Volumetric Flow Rates, and Flux-Averaged NO_3, Tc-99, and Total Uranium Concentrations Crossing the 122 m Elevation Over Time for Different Values of K_d.

Figure 4.14 shows simulated aqueous volumetric flow rates, and flux-averaged NO_3, Tc-99, and total uranium concentrations crossing the 122 m elevation over time for 200 realizations of model source terms. Hydraulic and sorption parameters were held constant for these simulation cases. Comparisons of Figure 4.14 with Figure 4.11 through Figure 4.13 indicate that the sensitivity of these variables to the modeled uncertainty in source terms is less than that of the hydraulic and sorption parameters. This result is particularly interesting considering that the modeled uncertainty in source terms for all sites was ±50%, which is more uncertainty than was estimated by Corbin et al. (2006) for many of the waste sites in the B-Complex

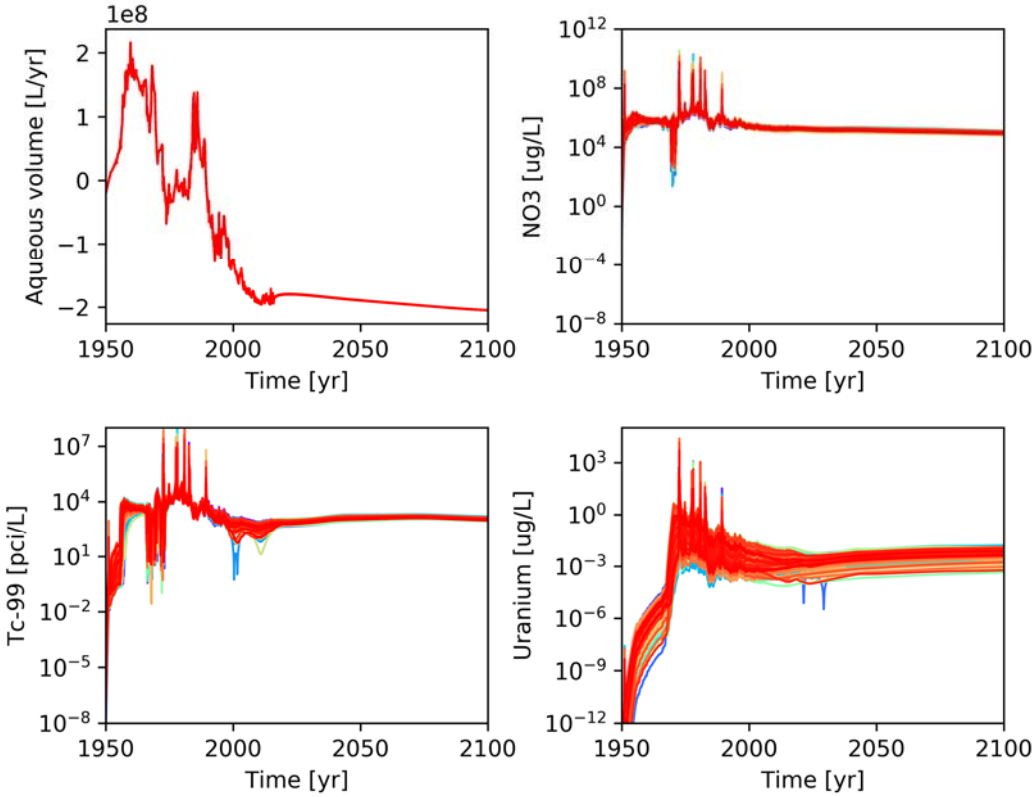

Figure 4.14. Simulated Aqueous Volumetric Flow Rates, and Flux-Averaged NO_3, Tc-99, and Total Uranium Concentrations Crossing the 122 m Elevation Over Time for 200 Realizations of Source Terms.

4.5 Discussion

This study illustrates the sensitivity of predicted groundwater concentrations, and fluxes of water and contaminants of concern from the vadose zone to the underlying aquifer, on uncertainties in hydraulic parameters, sorption parameters, and source terms, with each factor evaluated separately. A more rigorous analysis is planned to evaluate sensitivity of model results to all of these factors, and perhaps others, simultaneously. This will allow for a more formal sensitivity analysis, including consideration of variable interactions (Dai et al. 2017). This will also allow the relative sensitivity of model outputs to inputs to be determined quantitatively (Sobol, 2001). A formal global sensitivity analysis was not performed for the current study owing to the exploratory nature of this study. For future analyses, a much larger computational effort will be needed.

Due to the sparseness of groundwater monitoring data for the B-Complex at early and intermediate times, and since multiple waste disposal sites have contributed to overlapping plumes that affect the observed concentrations of contaminants in groundwater (Appendix B), it is difficult to unambiguously categorize the aggregate behavior of the waste sites in the B-Complex according to the criteria proposed by Truex et al. (2015b). They defined Category I sites as being characterized by contaminant discharge from the vadose zone to groundwater that results in a single peak of groundwater contamination that, in most cases, will occur in the future. Category II sites are characterized by contaminant discharge from the vadose zone to groundwater that results in two peaks – one associated with an existing, near-term plume, and one that will occur in the future (similar to a Category I site). Use of such a framework and some of its associated algebraic equations or analytical solutions could potentially simplify and expedite a more formal sensitivity and uncertainty analysis. The challenge with this and many other complex waste sites is in abstracting the available information to develop surrogate models that are simple enough to allow for computationally-efficient analyses while still providing realistic representations of key features, events, and processes. However, even if simplified but realistic models can be developed, detailed, mechanistically-based models of the type used in the current study are always needed to underpin the simplified models.

Results of the current study will help to inform decisions on future analyses to support remedy evaluation for this and other complex waste sites. Future activities that could lead to the refinement of the model(s) and results presented herein may include the following:

1) Update source terms and reevaluate their uncertainties based on new inventory estimates from Zaher and Agnew (2018)

2) Update best estimates of hydraulic parameters and uncertainties based on detailed analysis of sediment characterization data (Hoffman 1992) and new physical and hydraulic property data from vadose zone core samples collected recently from the 200-UP-1 operable unit (Rockhold et al. 2018)

3) Implement an approach for addressing uncertainties in boundary conditions resulting from sparse and uncertain water level monitoring data (Dai et al. 2017).

4) Assess the adequacy of available characterization and monitoring data for better defining a baseline model configuration and associated parameters, and for supporting the development of multiple conceptual models for the B-Complex

5) Develop tools to facilitate semi-automated application of the global sensitivity and uncertainty analysis framework described by Dai et al. (2017)

The current modeling approach is relevant to assessing complex source uncertainties and potential remedies and for evaluating approaches for characterization and monitoring of vadose zone sources.

5.0 Conclusions

This report describes a preliminary study to assess the sensitivity of subsurface flow and transport model predictions to uncertainties in source terms, hydraulic parameters, and sorption parameters for a large-scale area with multiple discharges to the subsurface, using the B-Complex in the 200 East Area of the Hanford Site as a case study. Key findings of this work include the following:

- Simulation results suggest that a significant inventory of contaminants still remains in the vadose zone under the B-Complex and poses a continuing source of contamination to groundwater
- Continuing sources are predicted to persist well into the future (beyond year 2100)
- Modeled uncertainties in hydraulic parameters, sorption parameters, and source terms predicted Tc-99 and NO_3 groundwater concentrations that bracketed measured concentrations for many of the observation wells that were selected for comparison. Predicted Tc-99 concentrations matched observed concentrations more closely than NO_3 for at most of the groundwater monitoring locations.
- The relative sensitivity of predicted groundwater concentrations and contaminant flux to ground water are ranked as, from highest to lowest, sorption parameters, hydraulic parameters, and source terms. This implies that the chemical and physical properties of the vadose zone have a greater impact on contaminant flux to groundwater than uncertainties in the release mass/activity and volumes. Hence, remedies may need to largely focus on contaminant flux reduction to the water table. Although uncertainties in total liquid volumes and total contaminant mass/activity were considered, uncertainties in time-histories of waste disposal were not considered in this analysis and may impact the initial ranking.

The results of this study point to specific follow-on activities that are recommended for future work:

- Update source terms and reevaluate their uncertainties based on new inventory estimates from Zaher and Agnew (2018)
- Update best estimates of hydraulic parameters and uncertainties based on detailed analysis of past sediment characterization data (Hoffman 1992) and new data from vadose zone core samples collected recently from the 200-UP-1 operable unit (Rockhold et al. 2018)
- Address uncertainties in boundary conditions resulting from sparse and uncertain water level monitoring data

The results of this and proposed follow-on activities provide examples of uncertainty and complex source assessments that are relevant for characterization, monitoring, and remedy evaluations for the B-Complex and other Hanford waste sites.

6.0 Quality Assurance

The results presented in this report originate from work performed by the Pacific Northwest National Laboratory under a Nuclear Quality Assurance Program (NQAP). The NQAP implements the requirements of U.S. Department of Energy Order 414.1D, *Quality Assurance*, and 10 CFR 830 Subpart A, *Quality Assurance Requirements*. The NQAP uses ASME NQA-1-2012, *Quality Assurance Requirements for Nuclear Facility Applications*, as its consensus standard and NQA-1-2012 Subpart 4.2.1 as the basis for its graded approach to quality.

Two quality grading levels are defined by the NQAP:

Basic Research - The required degree of formality and level of work control is limited. However, sufficient documentation is retained to allow the research to be performed again without recourse to the original researcher(s). The documentation is also reviewed by a technically competent individual other than the originator.

Not Basic Research - The level of work control is greater than basic research. Approved plans and procedures govern the research, software is qualified, calculations are documented and reviewed, externally sourced data is evaluated, and measuring instrumentation is calibrated. Sufficient documentation is retained to allow the research to be performed again without recourse to the original researcher(s). The documentation is also reviewed by a technically competent individual other than the originator.

The work supporting the results presented in this report was performed in accordance with *Basic Research* grading level controls.

7.0 References

Cole CR, MP Bergeron, CJ Murray, PD Thorne, SK Wurstner, and PM Rogers. 2001. *Uncertainty Analysis Framework – Hanford Site-Wide Groundwater Flow and Transport Model*. PNNL-13641, Pacific Northwest National Laboratory, Richland, Washington.

Corbin RA, BC Simpson, MJ Anderson, WF Danielson III, JG Field, TE Jones, and CT Kincaid. 2005. *Hanford Soil Inventory Model, Rev. 1*. RPP-26744, Rev. 0, CH2M Hill Plateau Remediation Company, Richland, Washington (PNNL document number: PNNL-15367).

Dai H, X Chen, M Ye, X Song, and JM Zachara. 2017. "A geostatistics-informed hierarchical sensitivity analysis method for complex groundwater flow and transport modeling." *Water Resour. Res*. 53:4327-4343, doi:10.1002/2016WR019756.

Hammond TB. 2017. *Development of the Hanford South Geologic Framework Model, Hanford Site, Washington*. ECF-HANFORD-13-0029, Revision 4, CH2M Hill Plateau Remediation Company, Richland, Washington.

Hammond TB and D Lupton. 2015. *Development of the Hanford South Geologic Framework Model, Hanford Site, Washington*. ECF-HANFORD-13-0029, Revision 2, CH2M Hill Plateau Remediation Company, Richland, Washington.

Hoffmann KM. 1992. *200-BP-1 Borehole Summary Report for Tasks 2, 4, and 6*. WHC-SD-EN-TI-054, Rev. 0. Westinghouse Hanford Company, Richland, Washington.

Johnson TC and DM Wellman. 2013. *Re-Inversion of Surface Electrical Resistivity Tomography Data from the Hanford Site B-Complex*. PNNL-22520, RPT-DVZ-AFRI-014, Pacific Northwest National Laboratory, Richland, Washington.

Kozak MW, NE Olague, RR Rao, and JT McCord. 1993. *Evaluation of a Performance Assessment Methodology for Low-Level Radioactive Waste Disposal Facilities*. NUREG/CR-5927; SAND91-2801, Vol. 1, Prepared for U.S. Nucl. Regul. Comm. by Sandia National Laboratories, Albuquerque, New Mexico.

Meyer PD, M Ye, ML Rockhold, SP Neuman, and KJ Cantrell. 2007. *Combined Estimation of Hydrogeologic Conceptual Model, Parameter, and Scenario Uncertainty with Application to Uranium Transport at the Hanford Site 300 Area*. NUREG/CR-6940 (PNNL-16396), U.S. Nucl. Regul. Comm., Washington, D.C.

Meyer PD, M Ye, TJ Nicholson, SP Neuman, and ML Rockhold. 2014. *Incorporating scenario uncertainty within a hydrogeologic uncertainty assessment methodology*. In Proceedings of the International Workshop on Model Uncertainty: Conceptual and Practical Issues in the Context of Risk-Informed Decision Making, edited by A. Mosleh and J. Wood, Int. Workshop Ser. On Adv. Top. In Reliab. And Risk Anal., Cent. For Risk and Reliab., Univ. of Maryland, Md., ISSN: 1084-5658.

Oostrom M, MJ Truex, KC Carroll, and GB Chronister. 2013. "Perched-water analysis related to deep vadose zone contaminant transport and impact to groundwater." *J. Hydrol*. 505:228-239.

Oostrom M, MJ Truex, ML Rockhold, TC Johnson. 2017. "Deep vadose zone contaminant flux evaluation at the Hanford BY-Cribs site using forward and imposed concentration modeling approaches." *Environ. Process*. 4:771-797.

Rockhold ML, FA Spane, TW Wietsma, DR Newcomer, RE Clayton, I Demirkanli, DL Saunders, MJ Truex, MM Valenta-Snyder, and CJ Thompson. 2018. *Physical and Hydraulic Properties of Sediments from the 200-DV-1 Operable Unit*. PNNL-27846, RPT-DVZ-CHPRC 0005, Rev 0, Pacific Northwest National Laboratory, Richland, Washington.

Rockhold ML, ZF Zhang, and Y-J Bott. 2016. *Alternative Conceptual Models of the Subsurface at WMA-C*. PNNL-SA-24740 (limited distribution), Pacific Northwest National Laboratory, Richland, Washington.

Rockhold ML, ZF Zhang, PD Meyer, and JN Thomle. 2015. *Physical, Hydraulic, and Transport Properties of Sediments and Engineered Materials Associated with Hanford Immobilized Low-Activity Waste*. PNNL-23711, RPT-IGTP-004, Rev. 0, Pacific Northwest National Laboratory, Richland, Washington.

Saltelli A, 2002. "Sensitivity analysis for importance assessment." *Risk Analysis* 22(3):1-12 doi:10.1111/0272-4332.00040.

Saltelli A, M Ratto, T Andres, F Campolongo, J Cariboni, D Gatelli, M Saisana, S Tarantola. 2008. *Global Sensitivity Analysis: The Primer*. John Wiley and Sons, New York.

Serne RJ, BN Bjornstad, JM Keller, PD Thorne, DC Lanigan, JN Christensen, and GS Thomas. 2010. *Conceptual Models for Migration of Key Groundwater Contaminants through the Vadose Zone and Into the Unconfined Aquifer Below the B-Complex*. PNNL-19277, Pacific Northwest National Laboratory, Richland, Washington.

Serne RJ. 2007. *Kd Values for Agricultural and Surface Soils for Use in Hanford Site Farm, Residential, and River Shoreline Scenarios*. PNNL-16531, Pacific Northwest National Laboratory, Richland, Washington.

Sobol IM. 2001. "Global sensitivity indices for nonlinear mathematical models and their Monte Carlo estimates." *Mathematics and Computers in Simulation* 55:271-280.

Springer SD. 2018. Model Package Report: Central Plateau Vadose Zone Geoframework, Version 1.0. CP-60925, Revision 0. CH2MHill Plateau Remediation Company, Richland, Washington.

Truex MJ, M Oostrom, GV Last, CE Strickland, and GD Tartakovsky. 2015a. *Evaluating Contaminant Flux from the Vadose Zone to the Groundwater in the Hanford Central Plateau: SX Tank Farm Case Study*. PNNL-23737, RPT-DVZ-AFRI-026, Pacific Northwest National Laboratory, Richland, Washington.

Truex MJ, M Oostrom, and GD Tartakovsky. 2015b. *Evaluating Transport and Attenuation of Inorganic Contaminants in the Vadose Zone for Aqueous Waste Disposal Systems.* PNNL-24731, RPT-DVZ-AFRI-033, Pacific Northwest National Laboratory, Richland, Washington.

Weber MC. 2018. Development of the Hanford South Geologic Framework Model, Hanford Site, Washington. ECF-HANFORD-13-0029, Revision 5. CH2MHill Plateau Remediation Company, Richland, Washington.

Zaher U, and S Agnew. 2018. *Hanford Soil Inventory Model (SIM-v2) Calculated Radionuclide Inventory of Direct Liquid Discharges to Soil in the Hanford Site's 200 Areas.* ECF-HANFORD-17-0079, Rev. 0, CH2M Plateau Remediation Company, Richland, Washington.

Zhang ZF and R Khaleel. 2010. "Simulating field-scale moisture flow using a combined power-averaging and tensorial connectivity-tortuosity approach." *Water Resour. Res.* 46(9):10.1029/2009wr008595.

Appendix A

Model Development

Appendix A

Model Development

This appendix summarizes the development of a subsurface flow and transport model, built with eSTOMP, that represents a region surrounding the B-Complex in the northern part of the Hanford 200 East Area.

A.1 Geoframework Model Surfaces

Geoframework models (GFMs) usually provide the basis for development of subsurface flow and transport models of the Hanford Site. CH2M Hill Plateau Remediation Company (CHPRC) maintains a database of elevations representing the contacts between major hydrostratigraphic units at borehole and well locations. This geocontacts database has been used by CHPRC to develop a GFM for the area south of and including Gable Mountain and Gable Butte. This Hanford South GFM is updated annually to incorporate information obtained from drilling of new wells (Weber 2018; Hammond 2017; Hammond and Lupton 2015).

In late March 2018, CHPRC issued the first version of a Central Plateau Vadose Zone (CPVZ) GFM to support a composite analysis for waste sites on the Hanford Central Plateau (Springer 2018). In addition to the major hydrostratigraphic units, the CPVZ GFM includes subunits of the Hanford formation and Cold Creek Units (CCUs), which are potentially important to distinguish owing to differences in their properties that affect subsurface flow and contaminant transport behavior. Gridded surface elevation files representing Version 1.0 of the CPVZ GFM were obtained from CHPRC in April 2018. Qualification checks of CPVZ GFM data files by Pacific Northwest National Laboratory (PNNL) indicated a number of order-relation violations for unit contacts. Subsequent communications between PNNL, CHPRC, and Intera led to the decision that a combination of the gridded surface files representing Version 1.0 of the CPVZ GFM (Springer 2018) and Revision 5 of the Hanford South GFM (Weber 2018) should be used for building subsurface flow and transport models for regions in and around the 200 East Area, until a new version of the CPVZ GFM is released (meeting between PNNL, CHPRC, and Intera staff at Intera offices, Richland, WA, June 5, 2018). Gridded surface elevation files representing Revision 5 of the Hanford South GFM were obtained from CHPRC in early June 2018, and were then used in conjunction with the gridded surface files from Version 1.0 of the CPVZ GFM to develop a model of the region surrounding the B-Complex.

Figure A.1 shows the major hydrostratigraphic units for the 200-PO-1 operable unit. In this figure HSU 1 represents the undifferentiated Hanford formation (Hf) and HSU 3 is the undifferentiated CCU. HSU 4, 5, 8, and 9 represent the Ringold Formation Taylor Flats unit (Rtf), Ringold Formation unit E (RE or Rwie), the Ringold Formation lower mud (Rlm), and the Ringold Formation unit A (RA or Rwia), respectively. In the CPVZ GFM, HSU 1 (or Hf) is subdivided, from top to bottom, into H1, H2, and H3 subunits. The H1 and H3 subunits tend to be relatively thin and have higher gravel contents than the H2 subunit. In the CPVZ GFM the HSU 3 (or CCU) unit shown in Figure A.1 is subdivided into silt- (CCUz), carbonate- (CCUc), and gravel-dominated (CCUg) subunits.

Locally, within the area of the B-Complex, Oostrom et al. (2013) further subdivided the CCUz into CCUz-upper silt, CCUz-sand, and CCUz-lower silt zones. The CCUz-lower silt is also referred to as the "perching silt," and it forms a flux-limiting layer that creates a perched water zone within the overlying CCUz-sand. For the model described herein, the CCUz unit was subdivided into CCUz-upper silt, CCUz-

sand, and CCUz-lower silt zones, based on the thicknesses reported for these units by Oostrom et al. (2013, Figure 3). The CCUz-lower silt in the region around the perched water aquifer was also assigned a unique material identification so that its permeability could be reduced to create perched water conditions locally.

Figure A.2 through Figure A.13 show the elevations of each of the major hydrostratigraphic units and subunits within the modeled domain. Note that the Cold Creek and Ringold Formation units are discontinuous over the Hanford Site and some of these units appear to be absent within the area of the model domain.

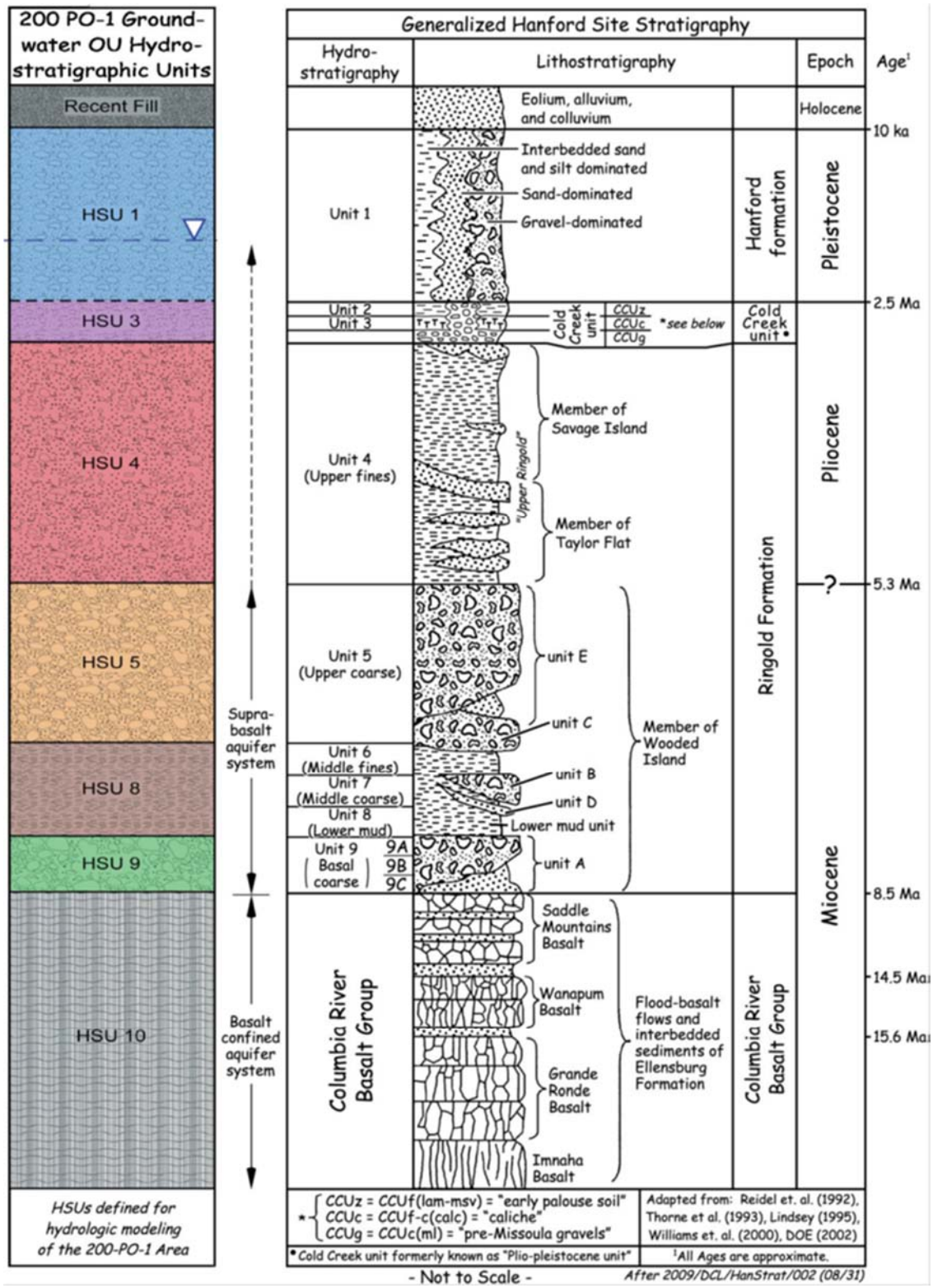

Figure A.1. Hydrostratigraphic Units Defined in the Hanford South Geologic Framework Model (Hammond and Lupton 2015) and Generalized Hanford Site Stratigraphy.

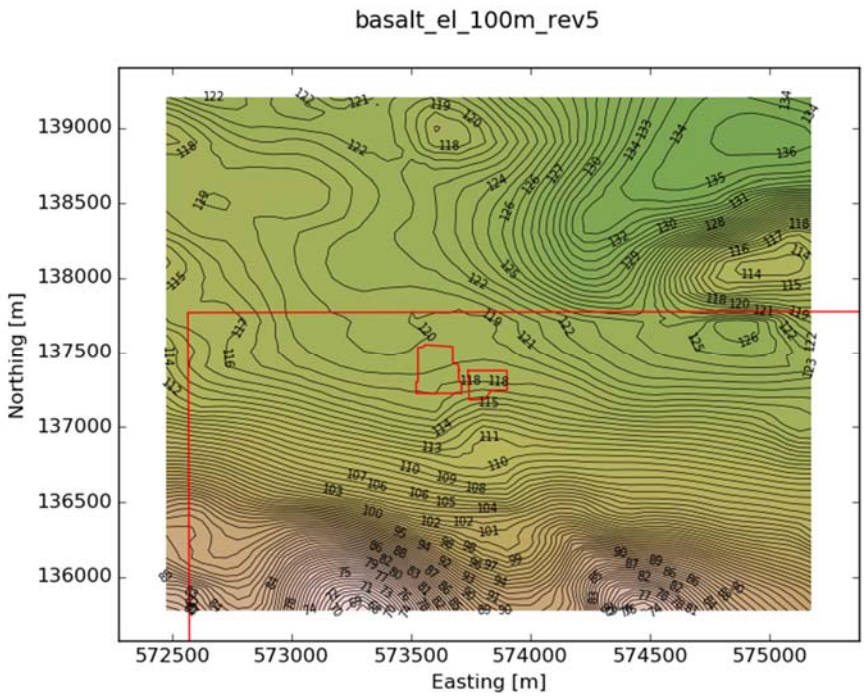

Figure A.2. Contour Map Showing Elevations of the Top of Basalt. The small red polygons in the center of the figure show outlines of the B-BX-BY tank farms within the B-Complex.

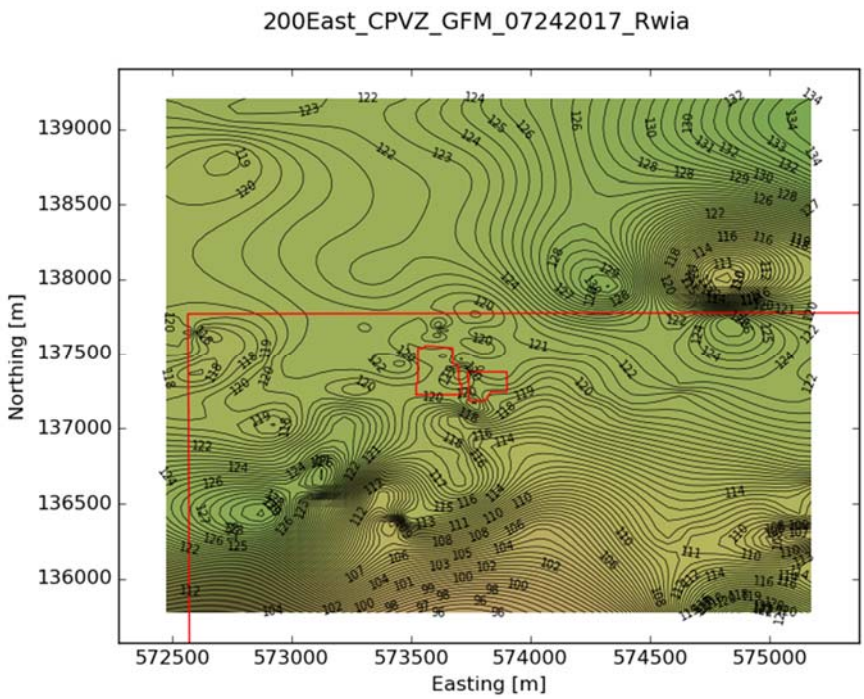

Figure A.3. Contour Map Showing Elevations of the Top of Ringold Unit A. The small red polygons in the center of the figure show outlines of the B-BX-BY tank farms within the B-Complex.

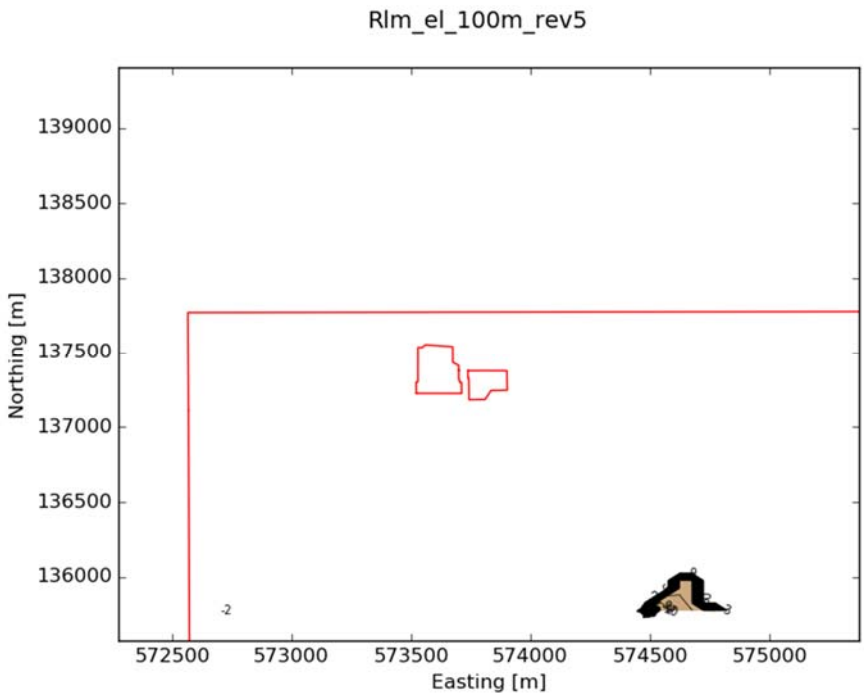

Figure A.4. Contour Map Showing Elevations of the Top of Ringold Lower Mud. The small red polygons in the center of the figure show outlines of the B-BX-BY tank farms within the B-Complex.

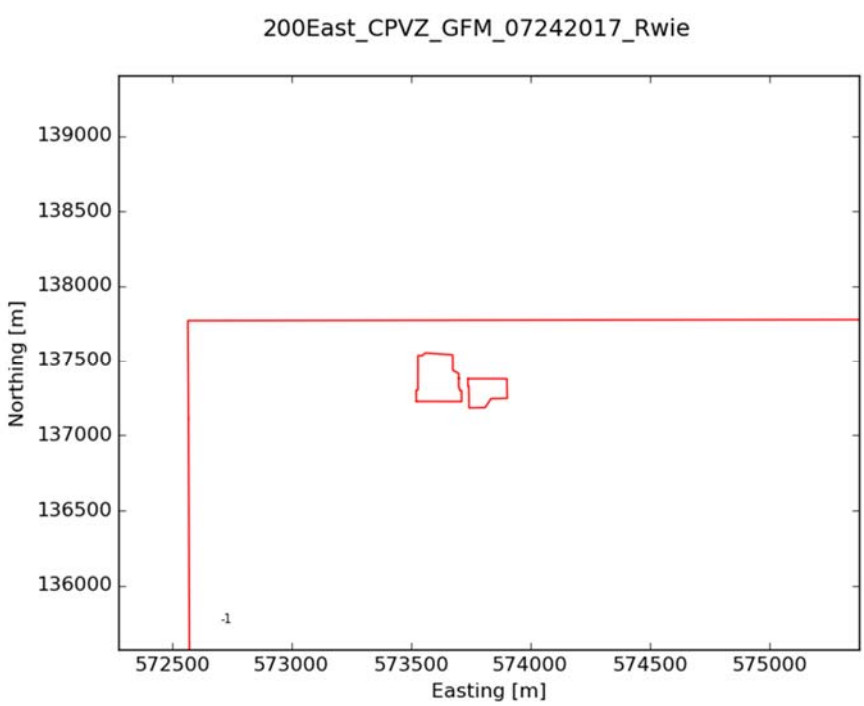

Figure A.5. Contour Map for the Top of Ringold Unit E, Which Is Absent. The small red polygons in the center of the figure show outlines of the B-BX-BY tank farms within the B-Complex.

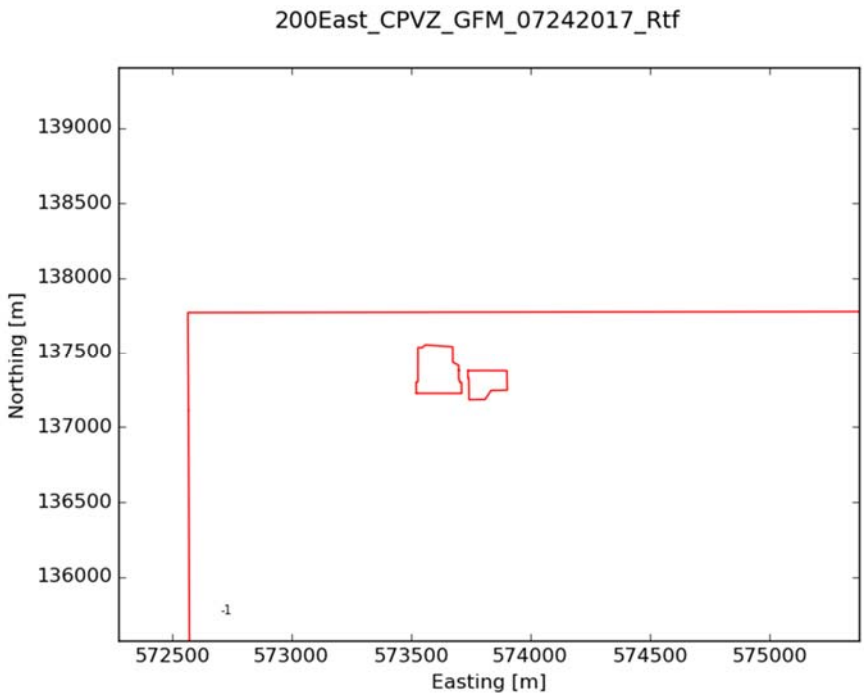

Figure A.6. Contour Map for the Top of Ringold Taylor Flats Unit, Which Is Absent. The small red polygons in the center of the figure show outlines of the B-BX-BY tank farms within the B-Complex.

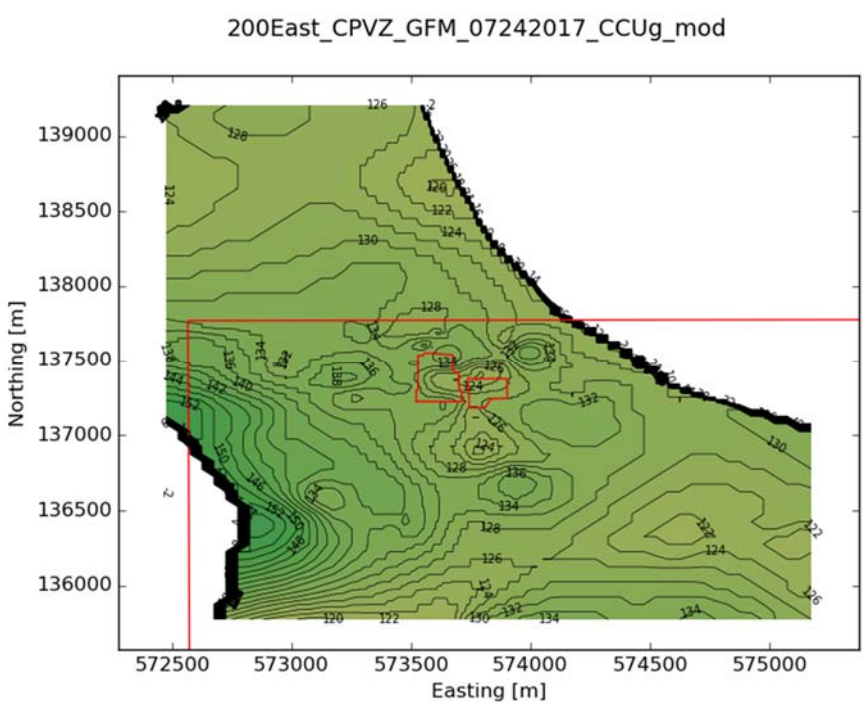

Figure A.7. Contour Map Showing Elevations of the Top of the Cold Creek Unit Gravels. The small red polygons in the center of the figure show outlines of the B-BX-BY tank farms within the B-Complex.

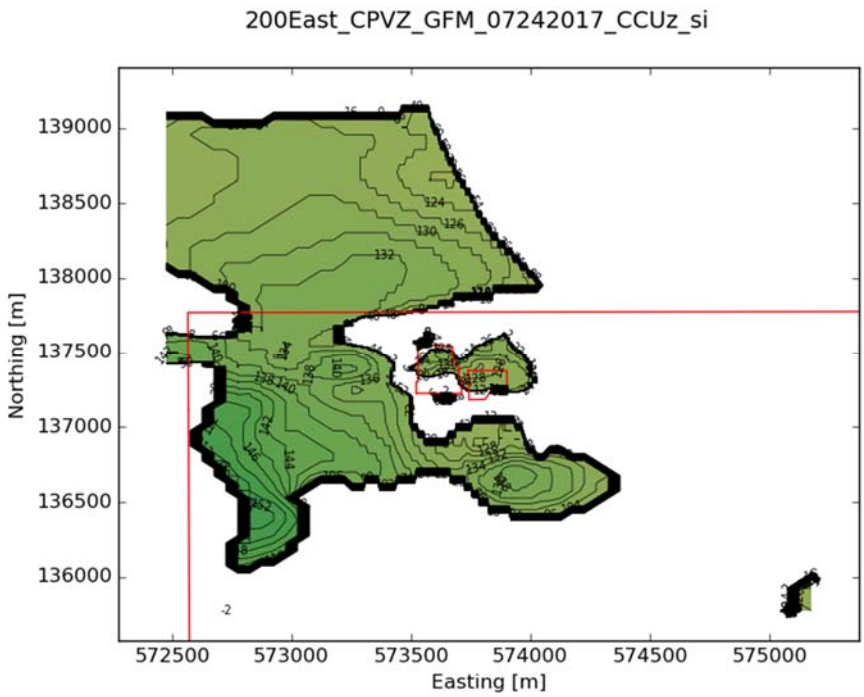

Figure A.8. Contour Map Showing Elevations of the Top of the Cold Creek Lower (perching) Silt. The small red polygons in the center of the figure show outlines of the B-BX-BY tank farms within the B-Complex.

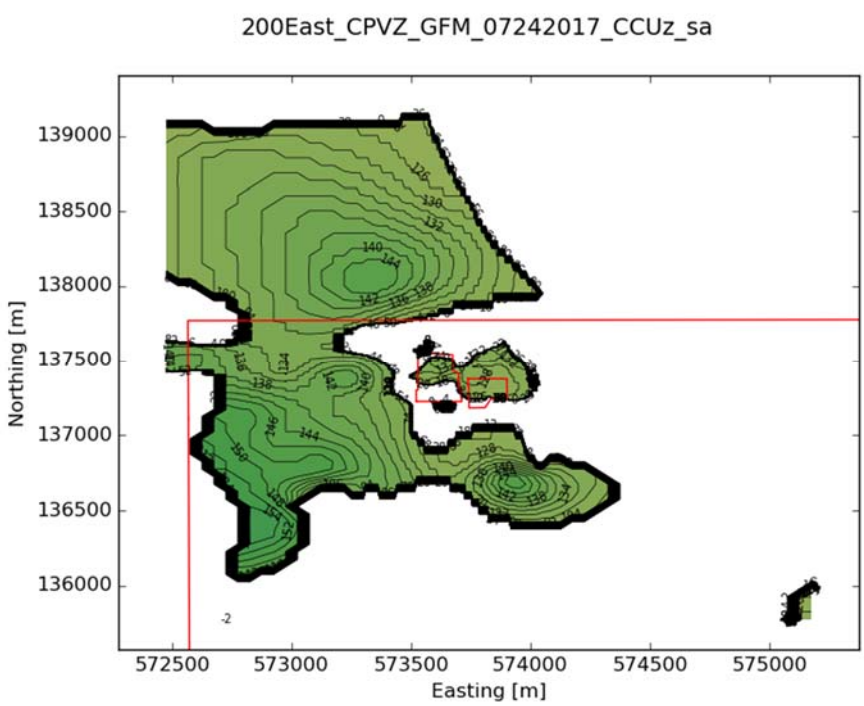

Figure A.9. Contour Map Showing Elevations of the Top of the Cold Creek Sand. The small red polygons in the center of the figure show outlines of the B-BX-BY tank farms within the B-Complex.

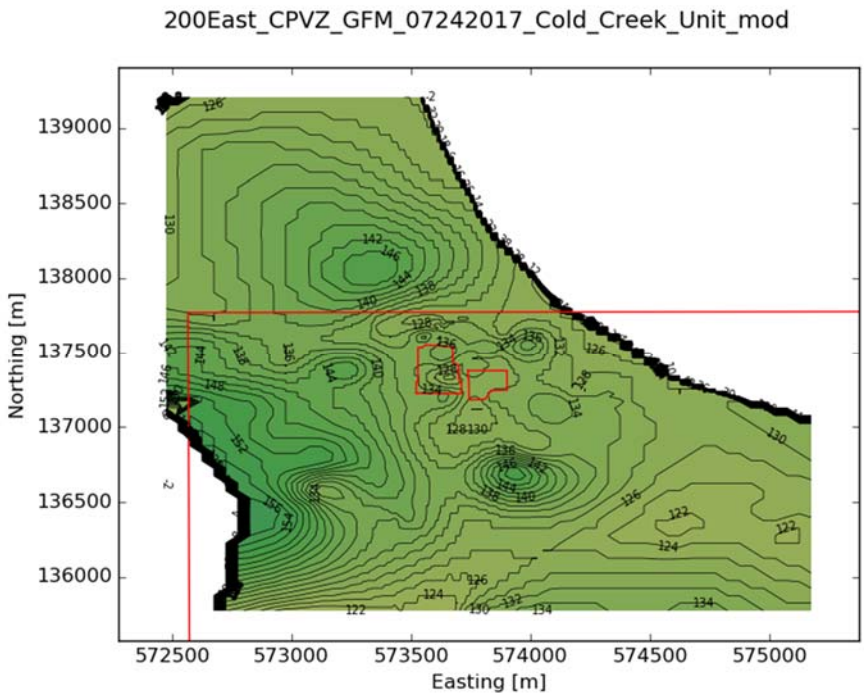

Figure A.10. Contour Map Showing Elevations of the Top of the Cold Creek Upper Silt. The small red polygons in the center of the figure show outlines of the B-BX-BY tank farms within the B-Complex.

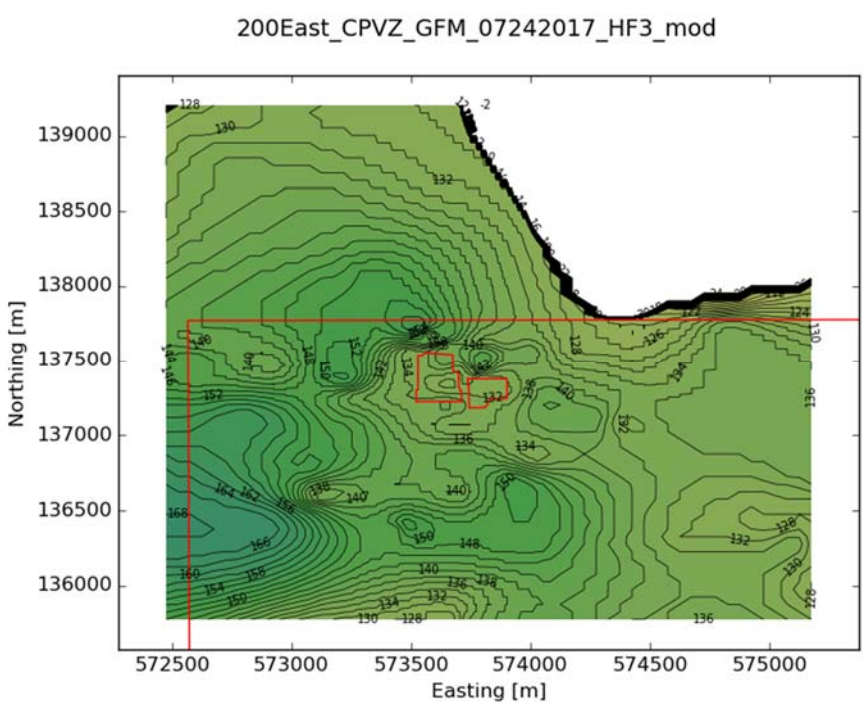

Figure A.11. Contour Map Showing Elevations of the Top of the Hanford H3 Unit. The small red polygons in the center of the figure show outlines of the B-BX-BY tank farms within the B-Complex.

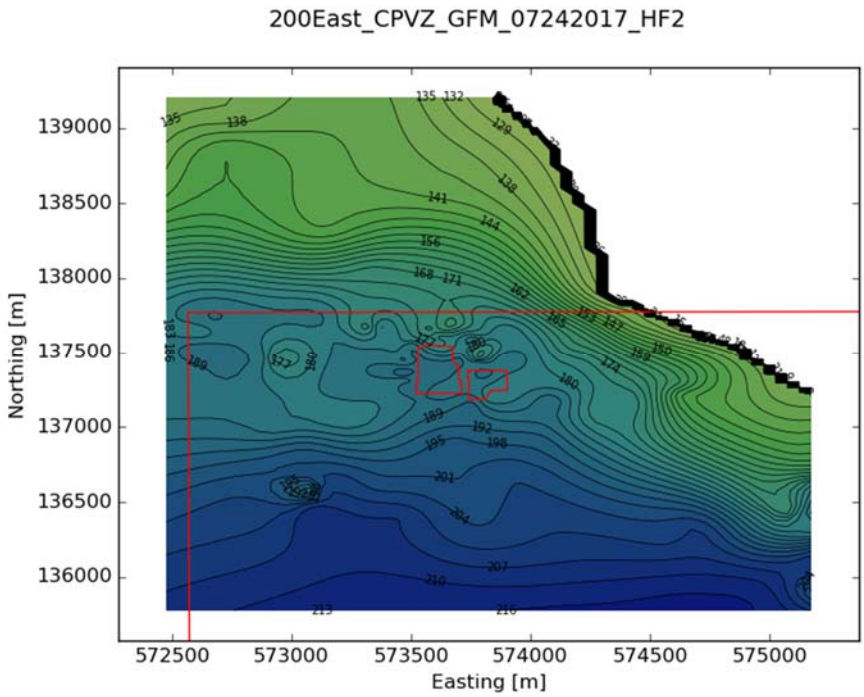

Figure A.12. Contour Map Showing Elevations of the Top of the Hanford H2 Unit. The small red polygons in the center of the figure show outlines of the B-BX-BY tank farms within the B-Complex.

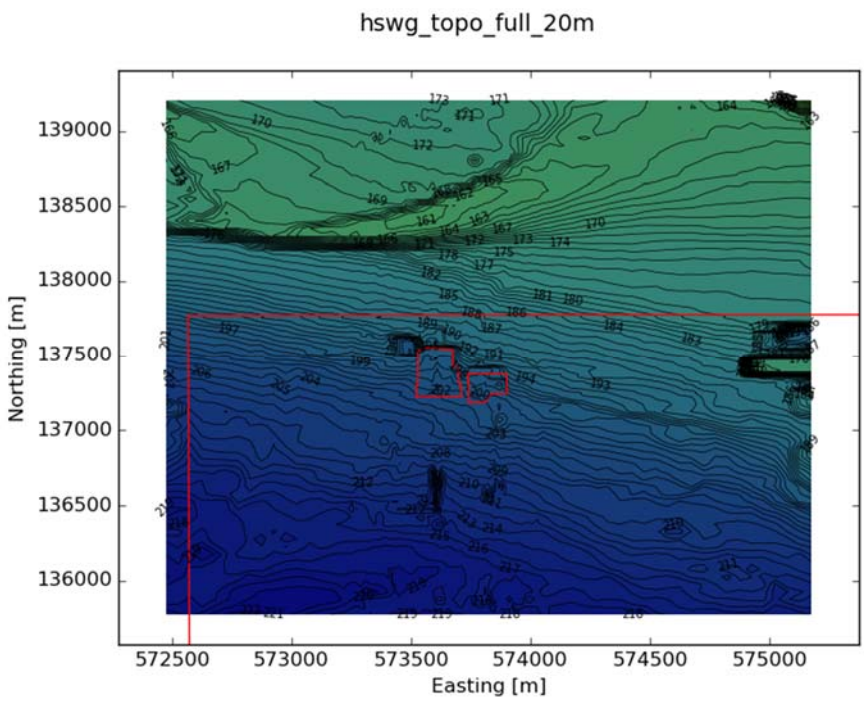

Figure A.13. Contour Map Showing Elevations of the Ground Surface (assumed top of H1). The small red polygons in the center of the figure show outlines of the B-BX-BY tank farms within the B-Complex.

Note that the ground surface elevations shown in Figure A.13 were determined by LiDAR (Aero-metric LiDAR 2008).

A.2 Zonation of Three-Dimensional Flow and Transport Model

Figure A.14 shows an oblique view (looking south-southwest) of the three-dimensional hydrostratigraphy of the modeled domain, constructed from the GFM gridded surface files. The domain spans 2750 m, 3478 m, and 132 m in the x-, y-, and z-directions, respectively, covering the 94 to 226 m elevation range. The domain was discretized into 162, 190, and 81 grid blocks in the x-, y-, and z-directions, respectively, for a total of about 2.5M grid blocks. Grid blocks lying above the top of the ground surface were specified as inactive. Non-uniform grid spacing was used in all directions, with grid block sizes ranging from 4 to 50 m in the x- and y-directions, and 0.5 to 2 m in the vertical (z-) direction.

Figure A.15 shows cross-sections of the three-dimensional model through the perched water aquifer zone underlying the B-Complex. Note that Unit 13 shown in Figure A.15, is part of the Cold Creek silt – lower silt subunit, but it was designated as a separate zone to account for potential local differences in properties for this particular region of interest (Oostrom et al. 2013).

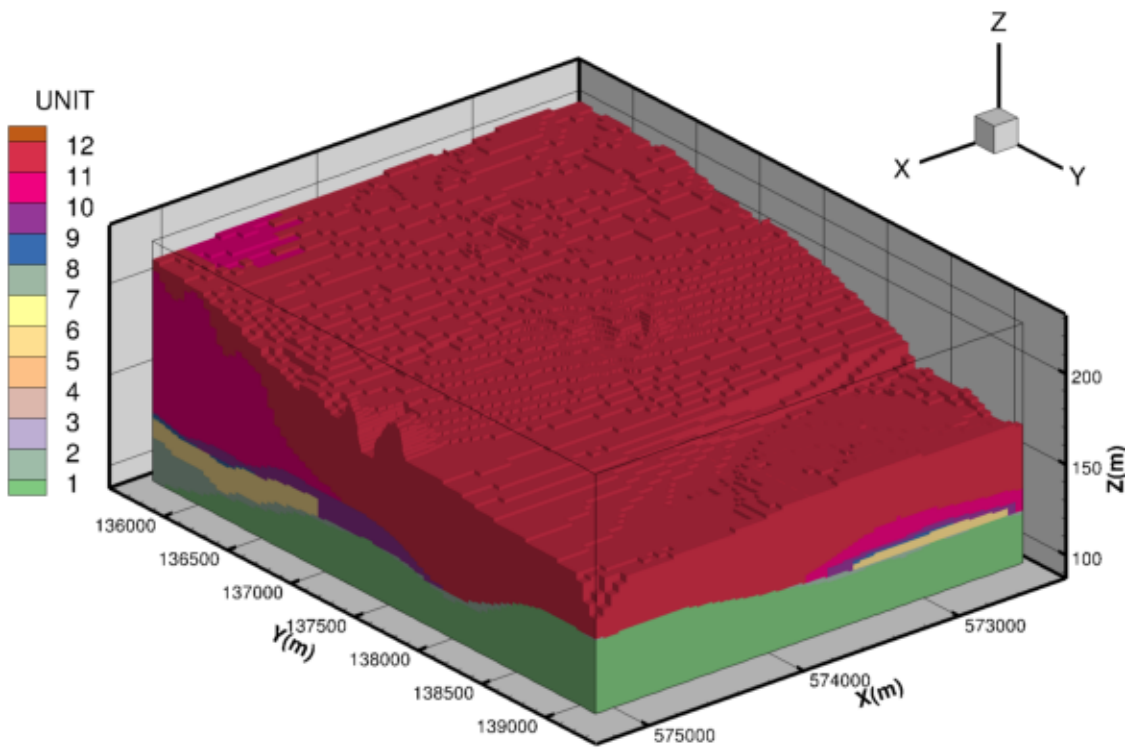

Figure A.14. Oblique View of Three-Dimensional Model of the Region around B-Complex Showing Hydrostratigraphic Units. Units: 1= Basalt, 2=Ringold unit A, 3=Ringold lower mud, 4=Ringold unit E, 5=Ringold Taylor Flats, 6=Cold Creek gravel, 7=Cold Creek silt - lower silt subunit, 8=Cold Creek silt – sand subunit, 9=Cold Creek silt - upper silt subunit, 10=Hanford H3, 11=Hanford H2, and 12=Hanford H1, respectively. Unit 13 is also in the Cold Creek silt – lower silt subunit, but was designated as a separate zone to better account for local properties within this region of interest. Vertical exaggeration = 5X.

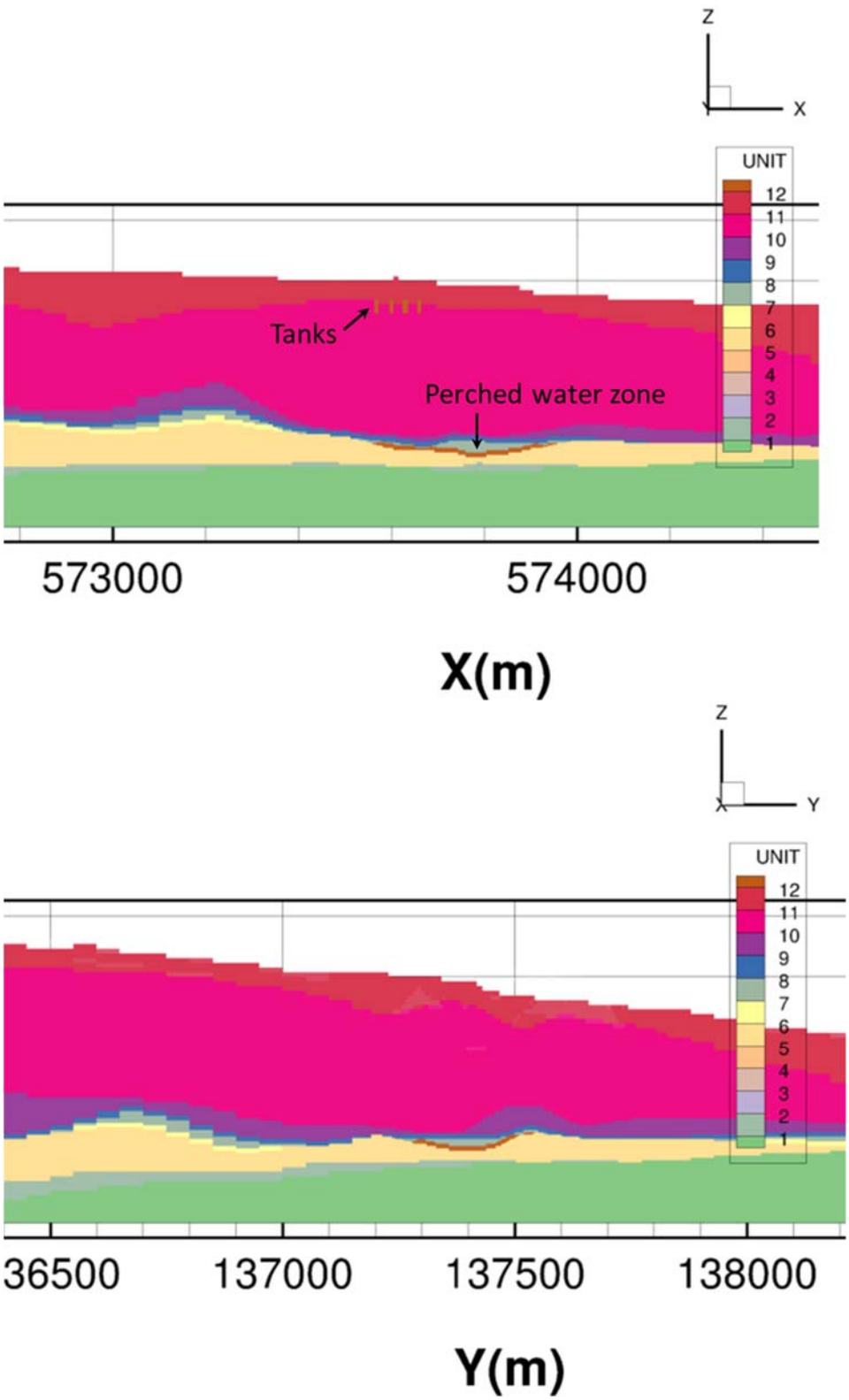

Figure A.15. West-East (top plot) and South-North (bottom plot) Cross Sections through the Three-Dimensional Model of the Region around B-Complex Showing the Location of the Perched Water Zone. Vertical exaggeration = 5X.

High-level waste storage tanks of the B-, BX-, and BY-tank farms were embedded within the model as low-porosity and low-permeability materials.

A.3 Material Properties

The material properties/parameters used in the model are listed inTable A.1.

Table A.1. Physical, Hydraulic, Transport, and Sorption Parameters Used for Model of the Hanford B-Complex Area.

Unit	Ks [a] [cm/s]	θ_s	S_r	α [1/cm]	n	ℓ [b]	ρ_s [g/cm^3]	d_L [m]	d_T [m]	K_d – Tc-99 [c] [cm^3/g]	K_d – NO_3 [c] [cm^3/g]	K_d – U-total [cm^3/g]
H1	6.65e-4 [K_s*0.01, K_s*1000]	0.28	0.14	0.014	2.12	0.5 [-0.683, 0.916]	2.59	1	1	0 [0.0, 1.0]	0 [0.0, 1.0]	0.8
H2	2.27e-3 [K_s*0.01, K_s*1000]	0.386	0.077	0.061	2.03	0.5 [-0.683, 0.916]	2.62	1	1	0 [0.0, 1.0]	0 [0.0, 1.0]	0.8
H3	6.65e-4 [K_s*0.01, K_s*1000]	0.28	0.14	0.014	2.12	0.5 [-0.683, 0.916]	2.59	1	1	0 [0.0, 1.0]	0 [0.0, 1.0]	0.8
CCUz-upper silt	5.57e-5	0.404	0.097	0.005	2.25	0.5	2.82	1	1	0	0	0.8
CCUz-sand	1.18e-4	0.252	0.134	0.017	1.73	0.5	2.82	1	1	0	0	0.8
CCUz-lower silt	5.57e-5	0.404	0.097	0.005	2.25	0.5	2.82	1	1	0	0	0.8
CCUz-lower silt under B-Complex	1.00e-7	0.376	0.066	0.0046	1.767	0.5	2.82	0.1	0.1	0	0	0.8
CCUg	3.30e-4	0.258	0.134	0.017	1.73	0.5	2.63	1	1	0	0	0.8
Rtf	5.79e-2	0.25	0.0725	0.021	1.374	0.5	2.71	10	1	0	0	0.8
Re	8.71e-2	0.3	0.0725	0.021	1.374	0.5	2.71	10	1	0	0	0.8
Rlm	4.08e-8	0.45	0.0565	0.0197	1.419	0.5	2.71	10	1	0	0	0.8
Ra	1.95e-3	0.2	0.0562	0.0197	1.419	0.5	2.71	10	1	0	0	0.8
Ba	1.62e-8	0.1	0.0725	0.021	1.374	0.5	2.71	10	1	0	0	0.8
Tanks	1.0e-25	0.01	0.0755	0.01	1.698	0.5	2.71	0	0	0	0	0.8

(d) Numbers in brackets are lower and upper limits for K_s. Six values were evaluated: 0.01*K_s, 0.1*K_s (baseline), K_s, 10*K_s, 100*K_s, 1000*K_s.

(e) Baseline model used 0.1*Ks and constant value of pore interaction term, ℓ=0.5. Alternative cases used 0.1*Ks and TCT model of moisture-dependent anisotropy (Zhang and Khaleel 2010), with $\ell xx = \ell yy = -0.683$, and $\ell zz=0.916$. These values represent an intermediate level of anisotropy for sandy sediments (Rockhold et al. 2015).

(f) Values in brackets indicate lower and upper K_d limits used in simulations, based on Serne (2007). Eleven K_d values were evaluated over this range (inclusive), in increments of 0.1 cm^3/g.

A.4 Boundary Conditions

A.4.1 Lateral Boundaries

Lateral boundary conditions for the flow equation were specified as dynamic, linked-list seepage face boundaries. This is a special mixed Dirichlet- (specified pressure) and Neuman- (zero flux) type boundary condition in eSTOMP for which time-dependent aqueous pressures are specified for the locations of reference cell faces. Aqueous pressure gradients are also specified that are applied to cell faces in a linked list of model grid blocks. Aqueous pressures are computed internally by the code from the specified pressures and gradients for boundary cell faces of grid blocks in the linked list that are fully water saturated. No-flow conditions are applied to boundary cell faces in the linked list for grid blocks that are unsaturated. If a grid block changes from saturated to unsaturated, or vice versa, during the simulation, the boundary condition type applied to the cell faces in the linked list changes automatically. The aqueous pressures specified for the reference cell faces and pressure gradients were determined by interpolating water table elevation measurements from monitoring well data reported in the Hanford Environmental Information System. Four sets of linked lists were used on each side of the model domain. Lateral boundary conditions for the transport equation were specified as outflow boundaries.

A.4.2 Upper and Lower Boundary

The area representing the top surface of the modeled domain was segmented into different land categories based on 2017 areal imagery from the National Agriculture Imagery Program (NAIP 2017; https://www.fsa.usda.gov/programs-and-services/aerial-photography/imagery-programs/naip-imagery/; last accessed 04-Sept-2018), LiDAR data (Aerometric LiDAR 2008), and rasterized features representing road and building vectors from GIS shape files for the 200 East Area (Figure A.16).

Neuman-type (prescribed aqueous flux) boundary conditions were specified for the flow equation on the upper boundary cell faces of the modeled domain to represent spatially- and temporally-variable recharge rates (Fayer and Keller 2007; Last et al. 2006). Neuman-type zero-flux boundary conditions were specified for solute transport equations for the upper boundary cell faces. Table A.2 shows a portion of the boundary conditions card from the eSTOMP input file showing the recharge rates that were applied to the different land categories. No-flow conditions were assumed for both water and solutes for the bottom boundary of the model domain.

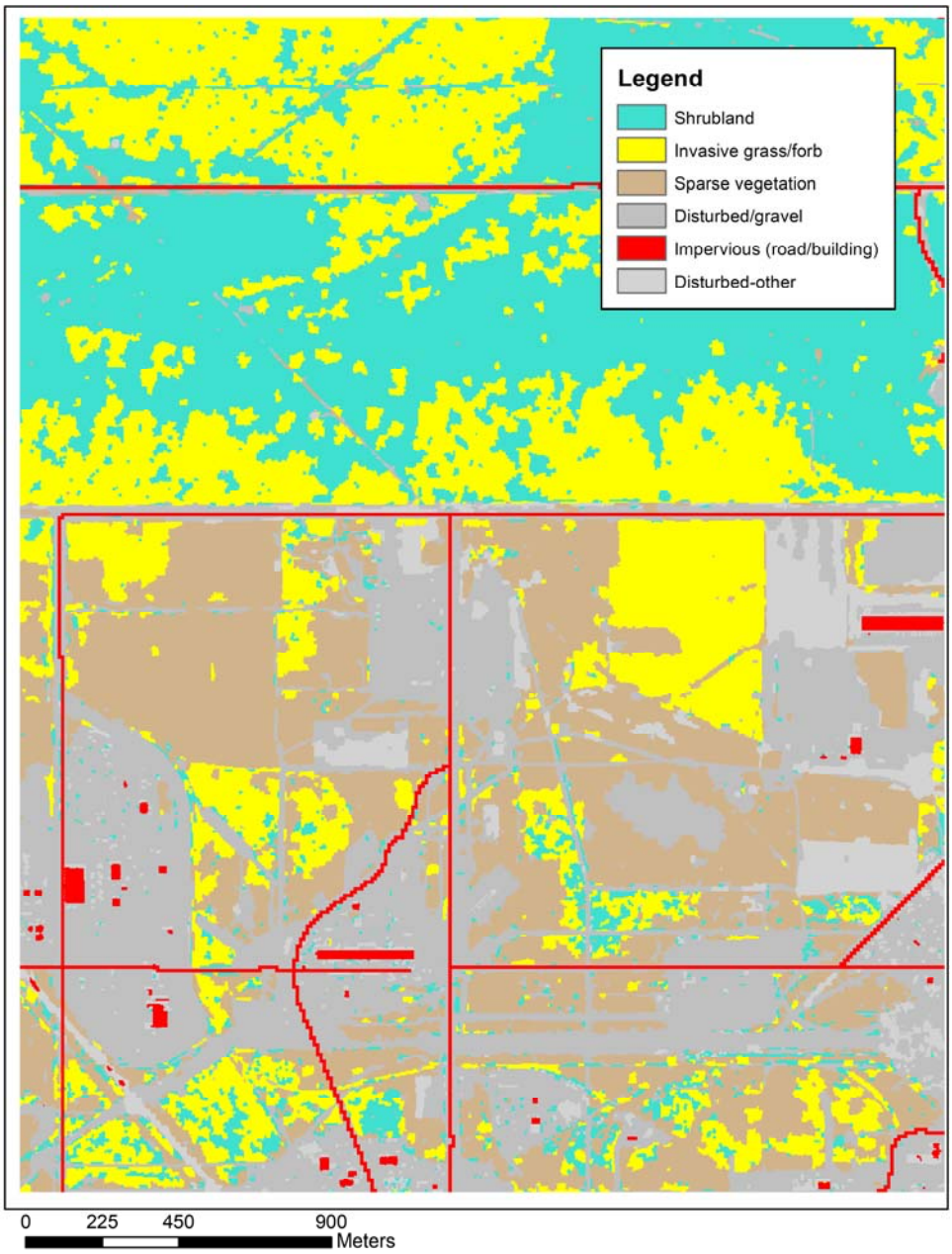

Figure A.16. Land Classification for Upper Surface of Model Domain.

Table A.2. Portion of the Boundary Conditions Card for the eSTOMP input file model of the B-Complex Area.

Recharge class: Disturbed/gravel-covered surfaces (including tank farms) # Ramping up recharge rate since B-BX-BY tanks farms were installed over a period of time. file,recharge_1.lnk,Neumann,inflow-outflow aqueous,inflow-outflow aqueous,inflow-outflow aqueous, 4, 0.0,yr,-2.8,mm/yr,0,1/m^3,0,,0,,0,, 1945.0,yr,-2.8,mm/yr,0,1/m^3,0,,0,,0,, 1950.0,yr,-92.0,mm/yr,0,1/m^3,0,,0,,0,, 3000.0,yr,-92.0,mm/yr,0,1/m^3,0,,0,,0,,
Recharge class: Sparse vegetation (e.g. native grasses and revegetated areas; BX trenches) file,recharge_2.lnk,Neumann,inflow-outflow aqueous,inflow-outflow aqueous,inflow-outflow aqueous, 6, 0.0,yr,-2.8,mm/yr,0,1/m^3,0,,0,,0,, 1953.0,yr,-2.8,mm/yr,0,1/m^3,0,,0,,0,, 1953.0,yr,-23.0,mm/yr,0,1/m^3,0,,0,,0,, 1977.0,yr,-23.0,mm/yr,0,1/m^3,0,,0,,0,, 1977.0,yr,-3.0,mm/yr,0,1/m^3,0,,0,,0,, 3000.0,yr,-3.0,mm/yr,0,1/m^3,0,,0,,0,,
Recharge class: Shrubland (Shrub-Steppe) file,recharge_3.lnk,Neumann,inflow-outflow aqueous,inflow-outflow aqueous,inflow-outflow aqueous, 2, 0.0,yr,-0.5,mm/yr,0,1/m^3,0,,0,,0,, 3000.0,yr,-0.5,mm/yr,0,1/m^3,0,,0,,0,,
Recharge class: Invasive grass/forb (e.g. cheatgrass) file,recharge_4.lnk,Neumann,inflow-outflow aqueous,inflow-outflow aqueous,inflow-outflow aqueous, 6, 0.0,yr,-2.8,mm/yr,0,1/m^3,0,,0,,0,, 1953.0,yr,-2.8,mm/yr,0,1/m^3,0,,0,,0,, 1953.0,yr,-23.0,mm/yr,0,1/m^3,0,,0,,0,, 1977.0,yr,-3.0,mm/yr,0,1/m^3,0,,0,,0,, 1977.0,yr,-3.0,mm/yr,0,1/m^3,0,,0,,0,, 3000.0,yr,-3.0,mm/yr,0,1/m^3,0,,0,,0,,
Recharge class: Disturbed-other (assumed the same as sparse vegetation areas) file,recharge_5.lnk,Neumann,inflow-outflow aqueous,inflow-outflow aqueous,inflow-outflow aqueous, 6, 0.0,yr,-2.8,mm/yr,0,1/m^3,0,,0,,0,, 1954.0,yr,-2.8,mm/yr,0,1/m^3,0,,0,,0,, 1954.0,yr,-23.0,mm/yr,0,1/m^3,0,,0,,0,, 1977.0,yr,-23.0,mm/yr,0,1/m^3,0,,0,,0,, 1977.0,yr,-3.0,mm/yr,0,1/m^3,0,,0,,0,, 3000.0,yr,-3.0,mm/yr,0,1/m^3,0,,0,,0,,
Recharge class: Impervious/roads/buildings file,recharge_6.lnk,Neumann,inflow-outflow aqueous,inflow-outflow aqueous,inflow-outflow aqueous, 4, 0.0,yr,-2.8,mm/yr,0,1/m^3,0,,0,,0,, 1945.0,yr,-2.8,mm/yr,0,1/m^3,0,,0,,0,, 1945.0,yr,-0.1,mm/yr,0,1/m^3,0,,0,,0,, 3000.0,yr,-0.1,mm/yr,0,1/m^3,0,,0,,0,,

A.5 Source Terms

Source term information was compiled from Serne et al. (2010) and references cited therein. The following tables list coordinates that were used to define polygons representing each waste site, and the liquid volumes and mass/activity of NO_3, total uranium, and Tc-99 that were released to the waste sites in the model.

Table A.3. Polygon Coordinates and Source Term Information Used to Represent Site 216-B-7A.

Easting (m, State Plane)	Northing (m, State Plane)
573789.38	137404.27
573800.25	137404.27
573800.25	137393.44
573789.38	137393.44
573789.38	137404.27

Start Date	End Date	NO_3 [kg]	U-Total [kg]	Tc-99 [Ci]	Liquid Volume [ML]
1/1/1946	12/31/1946	7.55E+04	1.79E-02	3.07E-05	8.75E-01
1/1/1947	12/31/1947	1.93E+05	4.56E-02	7.85E-05	2.24E+00
1/1/1948	12/31/1948	2.34E+05	9.75E-01	4.41E-04	2.61E+00
1/1/1949	12/31/1949	2.02E+05	4.76E-02	8.20E-05	2.34E+00
1/1/1950	12/31/1950	2.65E+05	6.25E-02	1.77E-04	3.08E+00
1/1/1951	12/31/1951	2.93E+05	6.95E-02	1.96E-04	3.41E+00
1/1/1952	12/31/1952	6.80E+04	1.61E-02	4.53E-05	7.90E-01
1/1/1953	12/31/1953	1.86E+04	8.95E-01	5.60E-04	3.86E+00
1/1/1954	12/31/1954	2.68E+03	1.29E-01	8.05E-05	5.55E-01
1/1/1966	12/31/1966	4.52E+03	7.90E+01	9.75E-05	4.65E-01
1/1/1967	12/31/1967	1.39E+03	1.73E+01	4.56E-02	1.00E-01

Table A.4. Polygon Coordinates and Source Term Information Used to Represent Site 216-B-7B.

Easting (m, State Plane)	Northing (m, State Plane)
573797.62	137389.88
573808.50	137389.88
573808.50	137379.05
573797.62	137379.05
573797.62	137389.88

Start Date	End Date	NO_3 [kg]	U-Total [kg]	Tc-99 [Ci]	Liquid Volume [ML]
1/1/1946	12/31/1946	7.55E+04	1.79E-02	3.07E-05	8.75E-01
1/1/1947	12/31/1947	1.93E+05	4.56E-02	7.85E-05	2.24E+00
1/1/1948	12/31/1948	2.34E+05	9.75E-01	4.41E-04	2.61E+00
1/1/1949	12/31/1949	2.02E+05	4.76E-02	8.20E-05	2.34E+00
1/1/1950	12/31/1950	2.65E+05	6.25E-02	1.77E-04	3.08E+00
1/1/1951	12/31/1951	2.93E+05	6.95E-02	1.96E-04	3.41E+00
1/1/1952	12/31/1952	6.80E+04	1.61E-02	4.53E-05	7.90E-01
1/1/1953	12/31/1953	1.86E+04	8.95E-01	5.60E-04	3.86E+00
1/1/1954	12/31/1954	2.68E+03	1.29E-01	8.05E-05	5.55E-01
1/1/1966	12/31/1966	4.52E+03	7.90E+01	9.75E-05	4.65E-01
1/1/1967	12/31/1967	1.39E+03	1.73E+01	4.56E-02	1.00E-01

Table A.5. Polygon Coordinates and Source Term Information Used to Represent Site 216-B-8.

Easting (m, State Plane)	Northing (m, State Plane)
573785.38	137456.06
573776.13	137461.36
573781.44	137470.63
573779.50	137496.56
573811.38	137552.11
573818.56	137554.06
573844.00	137539.48
573845.94	137532.28
573814.06	137476.88
573790.69	137465.31
573785.38	137456.06

Start Date	End Date	NO_3 [kg]	U-Total [kg]	Tc-99 [Ci]	Liquid Volume [ML]
1/1/1948	12/31/1948	5.05E+05	5.07E+01	1.91E-02	6.33E+00
1/1/1949	12/31/1949	5.40E+05	5.42E+01	2.05E-02	6.77E+00
1/1/1950	12/31/1950	6.96E+05	6.98E+01	3.00E-02	6.81E+00
1/1/1951	12/31/1951	1.66E+05	1.53E+01	9.47E-03	1.83E+00
1/1/1952	12/31/1952	2.13E+04	1.03E+00	6.41E-04	4.42E+00
1/1/1953	12/31/1953	9.45E+03	4.55E-01	2.84E-04	1.96E+00

Table A.6. Polygon Coordinates and Source Term Information Used to Represent Site 216-B-11A.

Easting (m, State Plane)	Northing (m, State Plane)
573849.57	137420.27
573851.97	137420.27
573851.97	137417.87
573849.57	137417.87
573849.57	137420.27

Start Date	End Date	NO_3 [kg]	U-Total [kg]	Tc-99 [Ci]	Liquid Volume [ML]
1/1/1952	12/31/1952	4.28E+01	7.85E-03	5.45E-04	7.15E+00
1/1/1953	12/31/1953	4.00E+01	6.65E-03	5.40E-04	4.01E+00
1/1/1954	12/31/1954	3.97E+01	6.55E-03	5.40E-04	3.66E+00

Table A.7. Polygon Coordinates and Source Term Information Used to Represent Site 216-B-11B.

Easting (m, State Plane)	Northing (m, State Plane)
573849.61	137401.97
573852.01	137401.97
573852.01	137399.57
573849.61	137399.57
573849.61	137401.97

Start Date	End Date	NO_3 [kg]	U-Total [kg]	Tc-99 [Ci]	Liquid Volume [ML]
1/1/1952	12/31/1952	4.28E+01	7.85E-03	5.45E-04	7.15E+00
1/1/1953	12/31/1953	4.00E+01	6.65E-03	5.40E-04	4.01E+00
1/1/1954	12/31/1954	3.97E+01	6.55E-03	5.40E-04	3.66E+00

Table A.8. Polygon Coordinates and Source Term Information Used to Represent Site 216-B-35.

Easting (m, State Plane)	Northing (m, State Plane)
573399.50	137279.28
573476.25	137279.28
573476.25	137275.94
573399.50	137275.94
573399.50	137279.28

Start Date	End Date	NO3 [kg]	U-Total [kg]	Tc-99 [Ci]	Liquid Volume [ML]
2/1/1954	2/28/1954	1.14E+05	3.63E+01	2.14E-01	1.06E+00

Table A.9. Polygon Coordinates and Source Term Information Used to Represent Site 216-B-36.

Easting (m, State Plane)	Northing (m, State Plane)
573399.44	137294.52
573476.31	137294.52
573476.31	137291.17
573399.44	137291.17
573399.44	137294.52

Start Date	End Date	NO_3 [kg]	U-Total [kg]	Tc-99 [Ci]	Liquid Volume [ML]
3/1/1954	4/30/1954	2.08E+05	6.64E+01	3.92E-01	1.94E+00

Table A.10. Polygon Coordinates and Source Term Information Used to Represent Site 216-B-37.

Easting (m, State Plane)	Northing (m, State Plane)
573399.38	137321.94
573476.13	137321.94
573476.13	137318.59
573399.38	137318.59
573399.38	137321.94

Start Date	End Date	NO_3 [kg]	U-Total [kg]	Tc-99 [Ci]	Liquid Volume [ML]
8/1/1954	9/30/1954	4.63E+05	1.48E+02	8.73E-01	4.32E+00

Table A.11. Polygon Coordinates and Source Term Information Used to Represent Site 216-B-38.

Easting (m, State Plane)	Northing (m, State Plane)
573399.25	137349.34
573476.00	137349.34
573476.00	137346.02
573399.25	137346.02
573399.25	137349.34

Start Date	End Date	NO_3 [kg]	U-Total [kg]	Tc-99 [Ci]	Liquid Volume [ML]
7/1/1954	7/30/1954	1.53E+05	4.90E+01	2.89E-01	1.43E+00

Table A.12. Polygon Coordinates and Source Term Information Used to Represent Site 216-B-39.

Easting (m, State Plane)	Northing (m, State Plane)
573399.19	137377.19
573476.00	137377.19
573476.00	137373.75
573399.19	137373.75
573399.19	137377.19

Start Date	End Date	NO_3 [kg]	U-Total [kg]	Tc-99 [Ci]	Liquid Volume [ML]
12/1/1953	12/31/1953	8.36E+04	2.67E+01	1.58E-01	7.80E-01
1/1/1954	11/30/1954	8.14E+04	2.60E+01	1.54E-01	7.60E-01

Table A.13. Polygon Coordinates and Source Term Information Used to Represent Site 216-B-40.

Easting (m, State Plane)	Northing (m, State Plane)
573399.13	137404.23
573475.87	137404.23
573475.87	137400.94
573399.13	137400.94
573399.13	137404.23

Start Date	End Date	NO_3 [kg]	U-Total [kg]	Tc-99 [Ci]	Liquid Volume [ML]
4/1/1954	7/31/1954	1.76E+05	5.62E+01	3.32E-01	1.64E+00

Table A.14. Polygon Coordinates and Source Term Information Used to Represent Site 216-B-41.

Easting (m, State Plane)	Northing (m, State Plane)
573399.06	137431.45
573476.06	137431.45
573476.06	137428.09
573399.06	137428.09
573399.06	137431.45

Start Date	End Date	NO_3 [kg]	U-Total [kg]	Tc-99 [Ci]	Liquid Volume [ML]
11/1/1954	11/30/1954	1.54E+05	4.93E+01	2.91E-01	1.44E+00

Table A.15. Polygon Coordinates and Source Term Information Used to Represent Site 216-B-42.

Easting (m, State Plane)	Northing (m, State Plane)
573307.50	137278.95
573384.25	137278.95
573384.25	137275.61
573307.50	137275.61
573307.50	137278.95

Start Date	End Date	NO_3 [kg]	U-Total [kg]	Tc-99 [Ci]	Liquid Volume [ML]
1/1/1954	12/31/1954	2.98E+05	4.65E+01	5.70E+00	1.50E+00

Table A.16. Polygon Coordinates and Source Term Information Used to Represent Site 216-B-43.

Easting (m, State Plane)	Northing (m, State Plane)
573616.25	137622.36
573633.44	137622.36
573633.44	137605.23
573616.25	137605.23
573616.25	137622.36

Start Date	End Date	NO_3 [kg]	U-Total [kg]	Tc-99 [Ci]	Liquid Volume [ML]
11/1/1954	11/30/1954	4.21E+05	6.58E+01	8.05E+00	2.12E+00

Table A.17. Polygon Coordinates and Source Term Information Used to Represent Site 216-B-44.

Easting (m, State Plane)	Northing (m, State Plane)
573616.25	137648.28
573633.38	137648.28
573633.38	137631.14
573616.25	137631.14
573616.25	137648.28

Start Date	End Date	NO_3 [kg]	U-Total [kg]	Tc-99 [Ci]	Liquid Volume [ML]
11/1/1954	12/31/1954	6.12E+05	9.55E+01	1.17E+01	3.08E+00
1/1/1955	3/30/1955	5.00E+05	7.81E+01	9.57E+00	2.52E+00

Table A.18. Polygon Coordinates and Source Term Information Used to Represent Site 216-B-45.

Easting (m, State Plane)	Northing (m, State Plane)
573616.19	137657.06
573633.31	137657.06
573633.31	137674.19
573616.19	137674.19
573616.19	137657.06

Start Date	End Date	NO_3 [kg]	U-Total [kg]	Tc-99 [Ci]	Liquid Volume [ML]
4/1/1955	6/30/1955	9.77E+05	1.65E+02	1.87E+01	4.92E+00

Table A.19. Polygon Coordinates and Source Term Information Used to Represent Site 216-B-46.

Easting (m, State Plane)	Northing (m, State Plane)
573616.13	137700.11
573633.25	137700.11
573633.25	137682.98
573616.13	137682.98
573616.13	137700.11

Start Date	End Date	NO_3 [kg]	U-Total [kg]	Tc-99 [Ci]	Liquid Volume [ML]
9/1/1955	12/31/1955	1.33E+06	2.08E+02	2.55E+01	6.70E+00

Table A.20. Polygon Coordinates and Source Term Information Used to Represent Site 216-B-47.

Easting (m, State Plane)	Northing (m, State Plane)
573573.62	137622.23
573590.75	137622.23
573590.75	137605.09
573573.62	137605.09
573573.62	137622.23

Start Date	End Date	NO_3 [kg]	U-Total [kg]	Tc-99 [Ci]	Liquid Volume [ML]
9/1/1955	9/30/1955	7.32E+05	1.14E+02	1.40E+01	3.68E+00

Table A.21. Polygon Coordinates and Source Term Information Used to Represent Site 216-B-48.

Easting (m, State Plane)	Northing (m, State Plane)
573573.56	137648.14
573590.69	137648.14
573590.69	137631.02
573573.56	137631.02
573573.56	137648.14

Start Date	End Date	NO_3 [kg]	U-Total [kg]	Tc-99 [Ci]	Liquid Volume [ML]
11/1/1955	11/30/1955	8.12E+05	1.27E+02	1.55E+01	4.09E+00

Table A.22. Polygon Coordinates and Source Term Information Used to Represent Site 216-B-49.

Easting (m, State Plane)	Northing (m, State Plane)
573573.56	137674.06
573590.63	137674.06
573590.63	137656.92
573573.56	137656.92
573573.56	137674.06

Start Date	End Date	NO_3 [kg]	U-Total [kg]	Tc-99 [Ci]	Liquid Volume [ML]
11/1/1955	12/31/1955	1.33E+06	2.08E+02	2.55E+01	6.70E+00

Table A.23. Polygon Coordinates and Source Term Information Used to Represent Site 216-B-50.

Easting (m, State Plane)	Northing (m, State Plane)
573573.50	137699.97
573590.56	137699.97
573590.56	137682.84
573573.50	137682.84
573573.50	137699.97

Start Date	End Date	NO_3 [kg]	U-Total [kg]	Tc-99 [Ci]	Liquid Volume [ML]
1/1/1965	12/31/1965	1.12E+01	2.90E-03	6.60E-03	5.56E+00
1/1/1966	12/31/1966	1.10E+01	2.82E-03	6.62E-03	5.30E+00
1/1/1967	12/31/1967	1.36E+01	4.07E-03	6.60E-03	9.00E+00
1/1/1968	12/31/1968	1.23E+01	3.45E-03	6.59E-03	7.16E+00
1/1/1969	12/31/1969	1.36E+01	4.07E-03	6.56E-03	9.00E+00
1/1/1970	12/31/1970	1.33E+01	3.90E-03	6.59E-03	8.50E+00
1/1/1971	12/31/1971	1.15E+01	3.09E-03	6.62E-03	6.10E+00
1/1/1972	12/31/1972	9.30E+00	2.04E-03	6.58E-03	2.99E+00
1/1/1973	12/31/1973	8.02E+00	1.41E-03	6.60E-03	1.11E+00
1/1/1974	1/31/1974	7.21E+00	1.04E-03	6.61E-03	2.25E-02

Table A.24. Polygon Coordinates and Source Term Information Used to Represent Site 216-B-51.

Easting (m, State Plane)	Northing (m, State Plane)
573836.04	137585.78
573864.83	137613.93
573866.83	137611.93
573838.04	137583.78

Start Date	End Date	NO_3 [kg]	U-Total [kg]	Tc-99 [Ci]	Liquid Volume [ML]
1/1/1956	12/31/1956	9.56E+01	1.49E-02	1.82E-03	4.80E-04
1/1/1957	12/31/1957	9.56E+01	1.49E-02	1.82E-03	4.80E-04
1/1/1958	1/31/1958	7.97E+00	1.24E-03	1.52E-04	4.00E-05

Table A.25. Polygon Coordinates and Source Term Information Used to Represent Site 216-B-57.

Easting (m, State Plane)	Northing (m, State Plane)
573486.19	137621.23
573510.81	137621.23
573510.81	137578.54
573486.19	137578.54
573486.19	137621.23

Start Date	End Date	NO_3 [kg]	U-Total [kg]	Tc-99 [Ci]	Liquid Volume [ML]
1/1/1968	12/31/1968	4.49E+01	9.39E-03	3.29E-02	1.25E+01
1/1/1969	12/31/1969	5.04E+01	1.19E-02	3.28E-02	2.00E+01
1/1/1970	12/31/1970	4.98E+01	1.17E-02	3.29E-02	1.93E+01
1/1/1971	12/31/1971	4.52E+01	9.58E-03	3.29E-02	1.30E+01
1/1/1972	12/31/1972	4.63E+01	1.00E-02	3.30E-02	1.44E+01
1/1/1973	12/31/1973	3.96E+01	6.86E-03	3.29E-02	5.13E+00

Table A.26. Polygon Coordinates and Source Term Information Used to Represent Site 216-BY-201.

Easting (m, State Plane)	Northing (m, State Plane)
573605.96	137601.62
573607.86	137601.62
573607.86	137589.02
573605.96	137589.02

Start Date	End Date	NO_3 [kg]	U-Total [kg]	Tc-99 [Ci]	Liquid Volume [ML]
1/1/1954	12/31/1954	1.18E+03	1.85E-01	2.26E-02	5.95E-03
1/1/1955	12/31/1955	7.09E+03	1.11E+00	1.36E-01	3.57E-02

Table A.27. Polygon Coordinates and Source Term Information Used to Represent Site 241-B-107.

Easting (m, State Plane)	Northing (m, State Plane)
573853.00	137261.00
573853.10	137261.00
573853.10	137260.90
573853.00	137260.90

Start Date	End Date	NO_3 [kg]	U-Total [kg]	Tc-99 [Ci]	Liquid Volume [ML]
1/1/1965	12/31/1965	2.35E+03	1.47E+00	2.83E-01	3.03E-02

Table A.28. Polygon Coordinates and Source Term Information Used to Represent Site 241-B-110.

Easting (m, State Plane)	Northing (m, State Plane)
573781.00	137281.00
573781.10	137281.00
573781.10	137280.90
573781.00	137280.90

Start Date	End Date	NO_3 [kg]	U-Total [kg]	Tc-99 [Ci]	Liquid Volume [ML]
1/1/1969	12/31/1969	3.40E+02	1.10E-01	5.42E-01	3.79E-02

Table A.29. Polygon Coordinates and Source Term Information Used to Represent Site 241-B-112.

Easting (m, State Plane)	Northing (m, State Plane)
573765.00	137325.00
573765.10	137325.00
573765.10	137324.90
573765.00	137324.90

Start Date	End Date	NO_3 [kg]	U-Total [kg]	Tc-99 [Ci]	Liquid Volume [ML]
1/1/1972	12/31/1972	5.00E+02	2.17E-01	1.02E+00	7.57E-03

Table A.30. Polygon Coordinates and Source Term Information Used to Represent Site 241-B-201.

Easting (m, State Plane)	Northing (m, State Plane)
573821.00	137357.00
573821.10	137357.00
573821.10	137356.90
573821.00	137356.90

Start Date	End Date	NO_3 [kg]	U-Total [kg]	Tc-99 [Ci]	Liquid Volume [ML]
1/1/1965	12/31/1965	2.93E+02	1.24E-04	1.19E-07	3.03E-02

Table A.31. Polygon Coordinates and Source Term Information Used to Represent Site 241-B-203.

Easting (m, State Plane)	Northing (m, State Plane)
573797.00	137357.00
573797.10	137357.00
573797.10	137356.90
573797.00	137356.90

Start Date	End Date	NO_3 [kg]	U-Total [kg]	Tc-99 [Ci]	Liquid Volume [ML]
1/1/1965	12/31/1965	8.92E+01	2.43E-05	3.62E-08	1.14E-03

Table A.32. Polygon Coordinates and Source Term Information Used to Represent Site 241-B-204.

Easting (m, State Plane)	Northing (m, State Plane)
573777.00	137357.00
573777.10	137357.00
573777.10	137356.90
573777.00	137356.90

Start Date	End Date	NO_3 [kg]	U-Total [kg]	Tc-99 [Ci]	Liquid Volume [ML]
1/1/1965	12/31/1965	9.43E+00	2.93E-05	1.28E-09	1.51E-03

Table A.33. Polygon Coordinates and Source Term Information Used to Represent Site 241-BX-101.

Easting (m, State Plane)	Northing (m, State Plane)
573674.00	137321.00
573674.10	137321.00
573674.10	137320.90
573674.00	137320.90

Start Date	End Date	NO_3 [kg]	U-Total [kg]	Tc-99 [Ci]	Liquid Volume [ML]
1/1/1972	12/31/1972	7.24E+02	4.54E-01	2.48E-01	1.51E-02

Table A.34. Polygon Coordinates and Source Term Information Used to Represent Site 241-BX-102.

Easting (m, State Plane)	Northing (m, State Plane)
573674.00	137341.00
573674.10	137341.00
573674.10	137340.90
573674.00	137340.90

Start Date	End Date	NO_3 [kg]	U-Total [kg]	Tc-99 [Ci]	Liquid Volume [ML]
1/1/1951	12/31/1951	3.80E+03	1.01E+04	2.27E+00	3.47E-01

Table A.35. Polygon Coordinates and Source Term Information Used to Represent Site 241-BX-108.

Easting (m, State Plane)	Northing (m, State Plane)
573589.00	137337.00
573589.10	137337.00
573589.10	137336.90
573589.00	137336.90

Start Date	End Date	NO_3 [kg]	U-Total [kg]	Tc-99 [Ci]	Liquid Volume [ML]
1/1/1972	12/31/1972	6.98E+02	2.87E-01	1.18E+00	9.46E-03

Table A.36. Polygon Coordinates and Source Term Information Used to Represent Site 241-BY-103.

Easting (m, State Plane)	Northing (m, State Plane)
573657.00	137517.00
573657.10	137517.00
573657.10	137516.90
573657.00	137516.90

Start Date	End Date	NO_3 [kg]	U-Total [kg]	Tc-99 [Ci]	Liquid Volume [ML]
1/1/1973	12/31/1973	3.27E+02	4.70E-02	2.99E-01	1.89E-02

Table A.37. Polygon Coordinates and Source Term Information Used to Represent Site 241-BY-107.

Easting (m, State Plane)	Northing (m, State Plane)
573597.00	137481.00
573597.10	137481.00
573597.10	137480.90
573597.00	137480.90

Start Date	End Date	NO_3 [kg]	U-Total [kg]	Tc-99 [Ci]	Liquid Volume [ML]
1/1/1974	12/31/1974	9.80E+02	1.41E-01	8.98E-01	5.72E-02

Table A.38. Polygon Coordinates and Source Term Information Used to Represent Site 241-BY-108.

Easting (m, State Plane)	Northing (m, State Plane)
573597.00	137513.00
573597.10	137513.00
573597.10	137512.90
573597.00	137512.90

Start Date	End Date	NO_3 [kg]	U-Total [kg]	Tc-99 [Ci]	Liquid Volume [ML]
1/1/1972	12/31/1972	3.27E+02	4.70E-02	2.99E-01	1.89E-02

A.6 References

Aero-Metric LiDAR, 2008. *RCCC-Hanford Battelle/PNNL/DOE, Digital Orthophotography and LiDAR Surveys Photogrammetric Report*, Aero-Metric, Seattle, Washington.

Fayer MJ and JM Keller. 2007. *Recharge Data Package for Hanford Single-Shell Tank Waste Management Areas*. PNNL-16688, Pacific Northwest National Laboratory, Richland, Washington.

Hammond TB. 2017. *Development of the Hanford South Geologic Framework Model, Hanford Site, Washington*. ECF-HANFORD-13-0029, Revision 4. CH2MHill Plateau Remediation Company, Richland, Washington.

Hammond TB and D Lupton. 2015. *Development of the Hanford South Geologic Framework Model, Hanford Site, Washington*. ECF-HANFORD-13-0029, Revision 2. CH2MHill Plateau Remediation Company, Richland, Washington.

Last GV, EJ Freeman, KJ Cantrell, MJ Fayer, GW Gee, WE Nichols, BN Bjornstad, and DG Horton. 2006. *Vadose Zone Hydrogeology Data Package for Hanford Assessments*. PNNL-14702, Rev. 1. Pacific Northwest National Laboratory, Richland, Washington.

NAIP 2017. https://www.fsa.usda.gov/programs-and-services/aerial-photography/imagery-programs/naip-imagery/ (last accessed 04-Sept-2018).

Oostrom M, MJ Truex, KC Carroll, and GB Chronister. 2013. "Perched-water analysis related to deep vadose zone contaminant transport and impact to groundwater." *J. Hydrol.* 505:228-239.

Oostrom M, MJ Truex, ML Rockhold, and TC Johnson. 2017. "Deep vadose zone contaminant flux evaluation at the Hanford BY-cribs site using forward and imposed concentration modeling approaches." Environ. Process. 4:771-797.

Serne RJ, BN Bjornstad, JM Keller, PD Thorne, DC Lanigan, JN Christensen, and GS Thomas. 2010. *Conceptual Models for Migration of Key Groundwater Contaminants through the Vadose Zone and Into the Unconfined Aquifer Below the B-Complex*. PNNL-19277, Pacific Northwest National Laboratory, Richland, Washington.

Springer SD. 2018. *Model Package Report: Central Plateau Vadose Zone Geoframework, Version 1.0*. CP-60925, Revision 0. CH2MHill Plateau Remediation Company, Richland, Washington.

Weber MC. 2018. Development of the Hanford South Geologic Framework Model, Hanford Site, Washington. ECF-HANFORD-13-0029, Revision 5. CH2MHill Plateau Remediation Company, Richland, Washington.

Appendix B

Simulation Results from Baseline Model

Appendix B

Simulation Results from Baseline Model

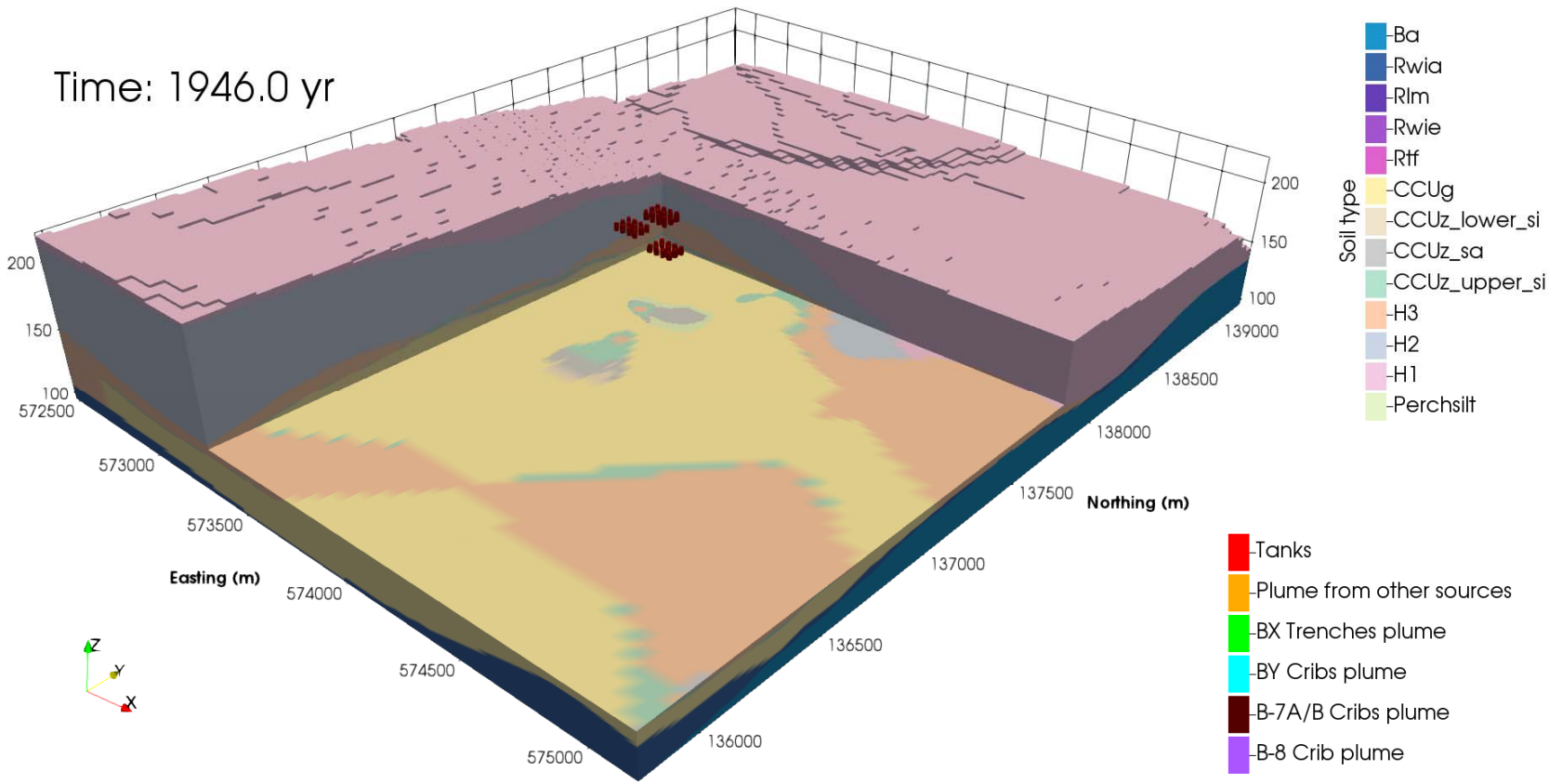

Figure B.1. Cutaway View of Hydrostratigraphic Units Underlying the B-Complex Showing Waste Storage Tanks of the B-BX-BY Tank Farms and Isosurfaces of Simulated Tc-99 Plumes [1 pCi/L] from Different Source Areas in 1946.

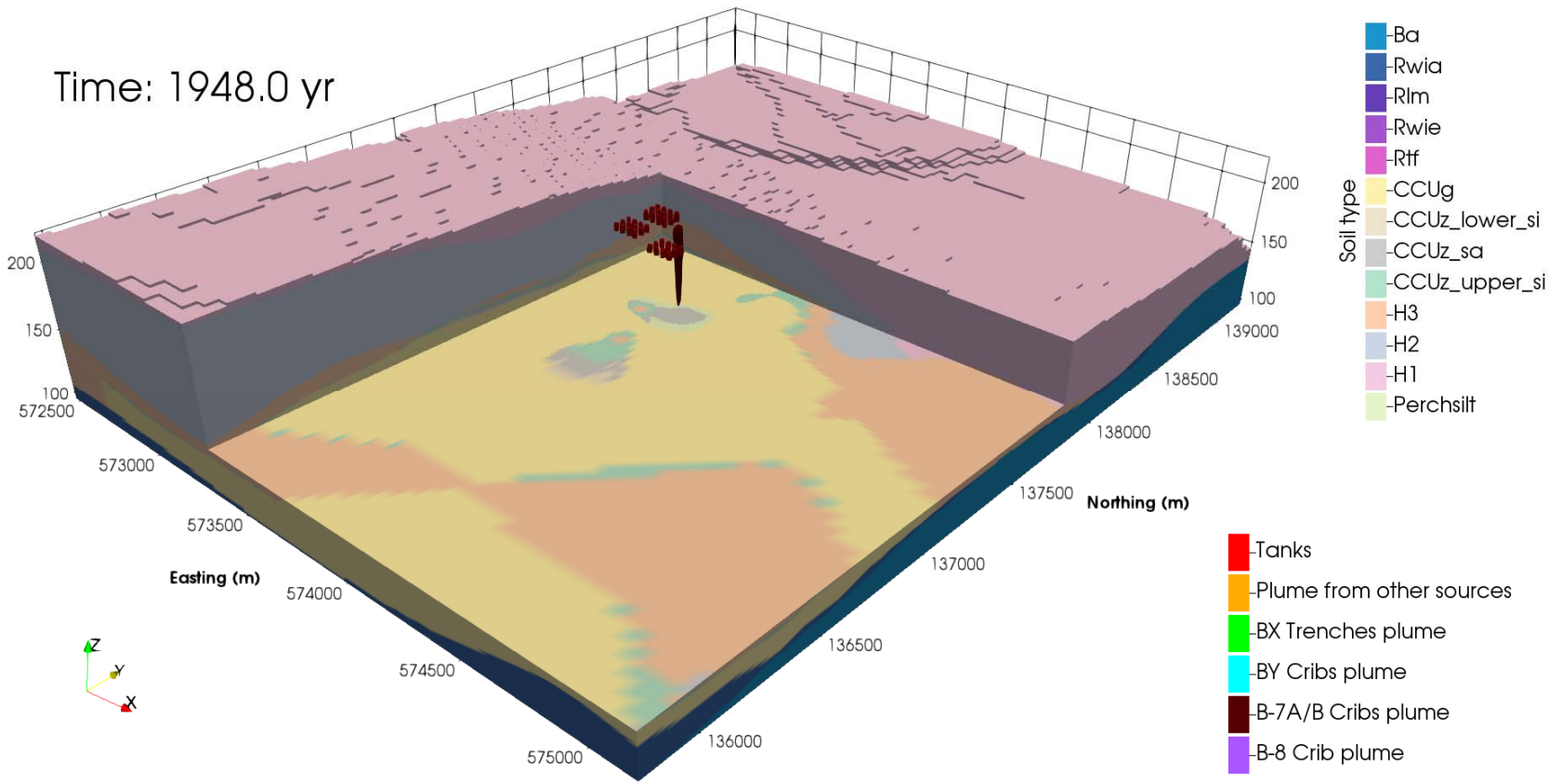

Figure B.2. Cutaway View of Hydrostratigraphic Units Underlying the B-Complex Showing Waste Storage Tanks of the B-BX-BY Tank Farms and Isosurfaces of Simulated Tc-99 Plumes [1 pCi/L] from Different Source Areas in 1948.

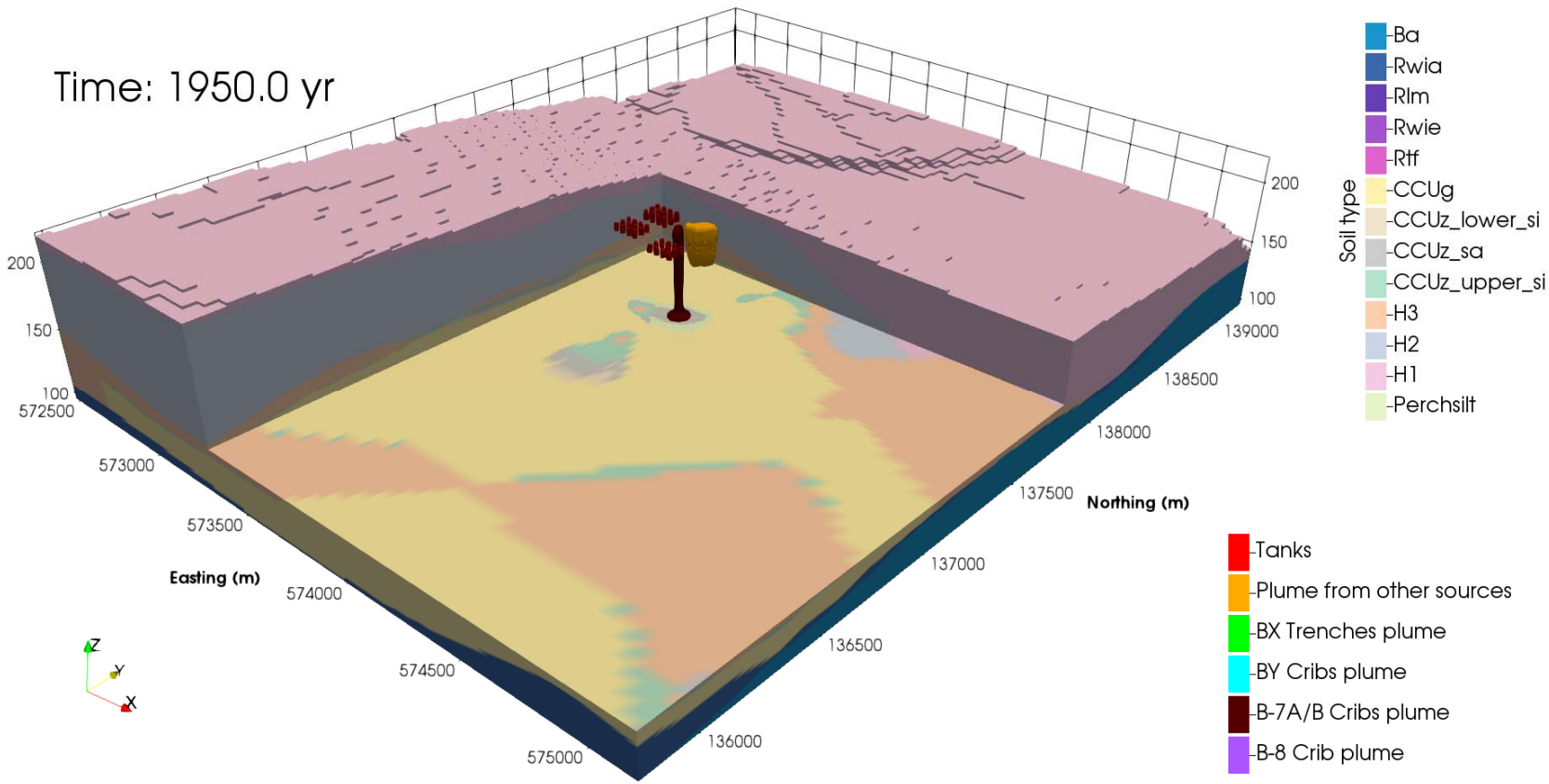

Figure B.3. Cutaway View of Hydrostratigraphic Units Underlying the B-Complex Showing Waste Storage Tanks of the B-BX-BY Tank Farms and Isosurfaces of Simulated Tc-99 Plumes [1 pCi/L] from Different Source Areas in 1950.

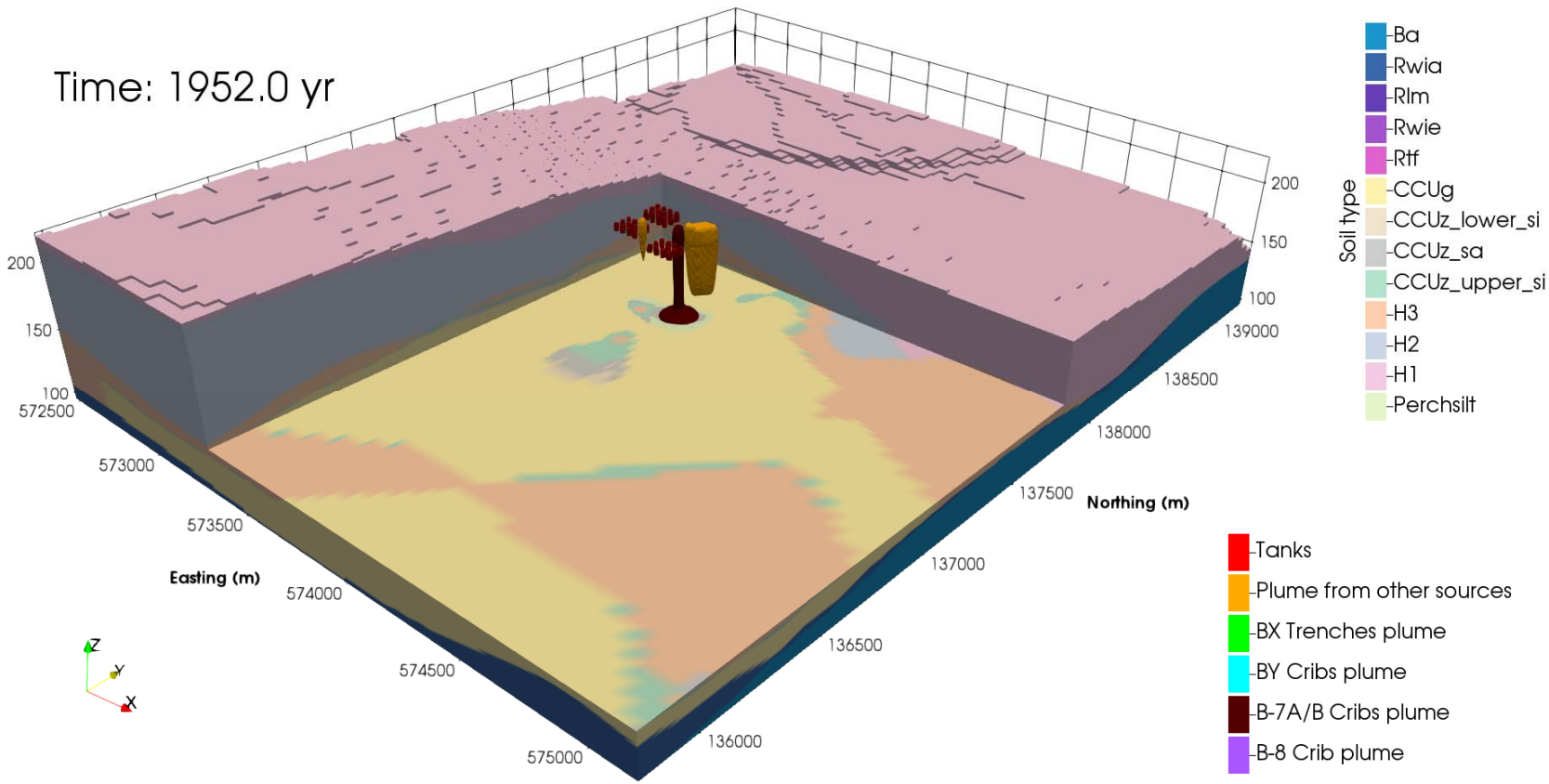

Figure B.4. Cutaway View of Hydrostratigraphic Units Underlying the B-Complex Showing Waste Storage Tanks of the B-BX-BY Tank Farms and Isosurfaces of Simulated Tc-99 Plumes [1 pCi/L] from Different Source Areas in 1952.

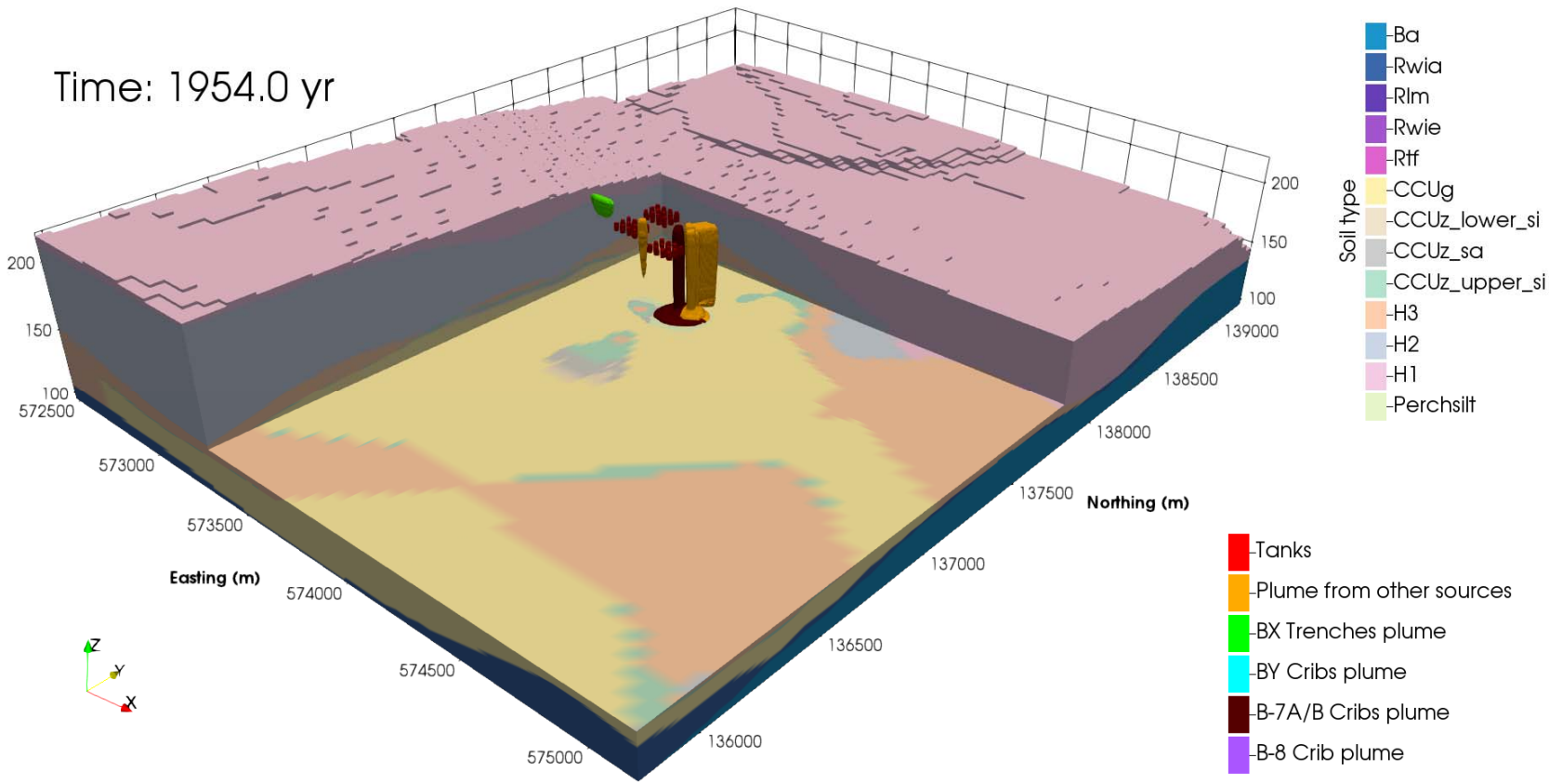

Figure B.5. Cutaway View of Hydrostratigraphic Units Underlying the B-Complex Showing Waste Storage Tanks of the B-BX-BY Tank Farms and Isosurfaces of Simulated Tc-99 Plumes [1 pCi/L] from Different Source Areas in 1954.

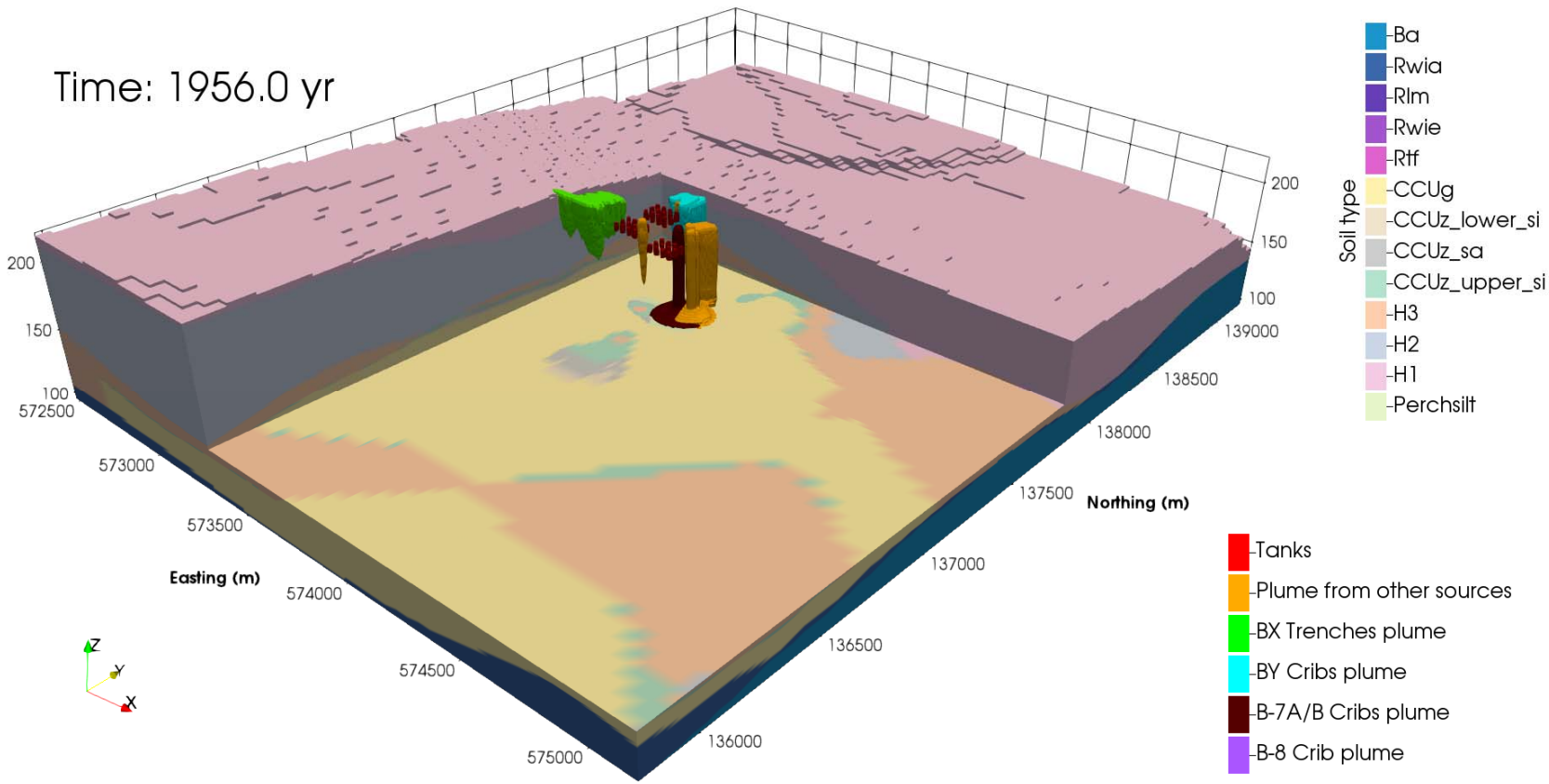

Figure B.6. Cutaway View of Hydrostratigraphic Units Underlying the B-Complex Showing Waste Storage Tanks of the B-BX-BY Tank Farms and Isosurfaces of Simulated Tc-99 Plumes [1 pCi/L] from Different Source Areas in 1956.

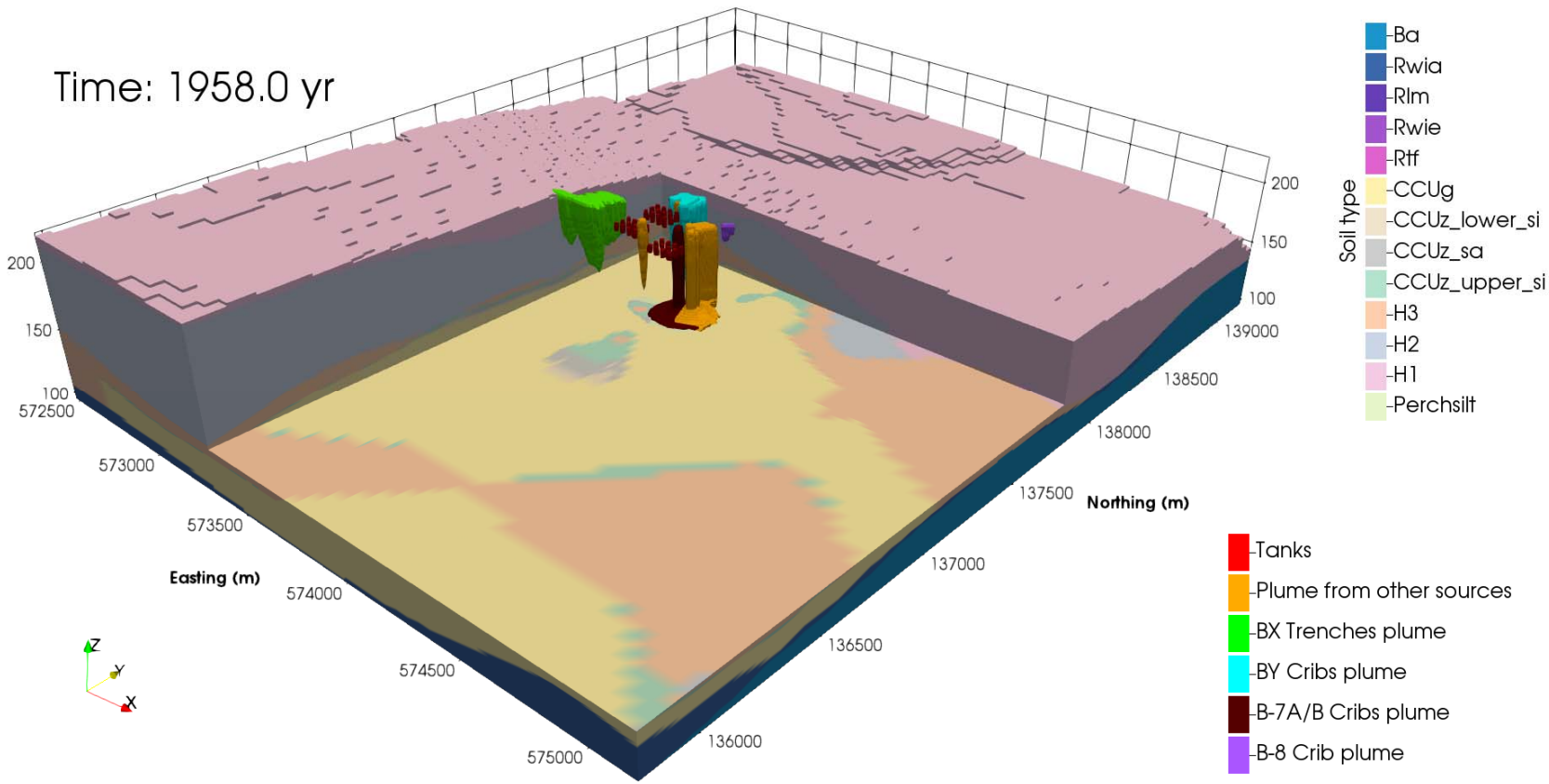

Figure B.7. Cutaway View of Hydrostratigraphic Units Underlying the B-Complex Showing Waste Storage Tanks of the B-BX-BY Tank Farms and Isosurfaces of Simulated Tc-99 Plumes [1 pCi/L] from Different Source Areas in 1958.

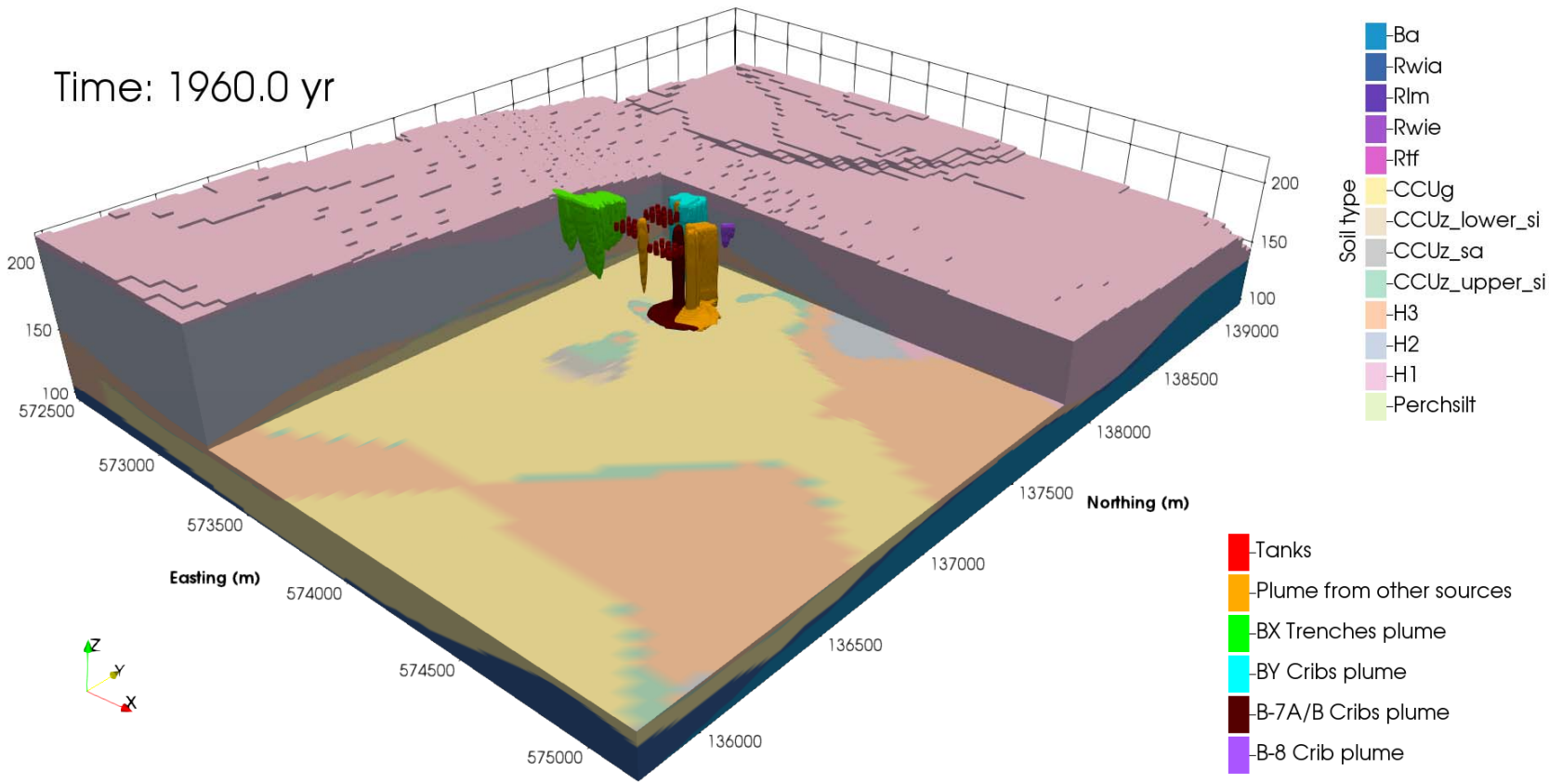

Figure B.8. Cutaway View of Hydrostratigraphic Units Underlying the B-Complex Showing Waste Storage Tanks of the B-BX-BY Tank Farms and Isosurfaces of Simulated Tc-99 Plumes [1 pCi/L] from Different Source Areas in 1960.

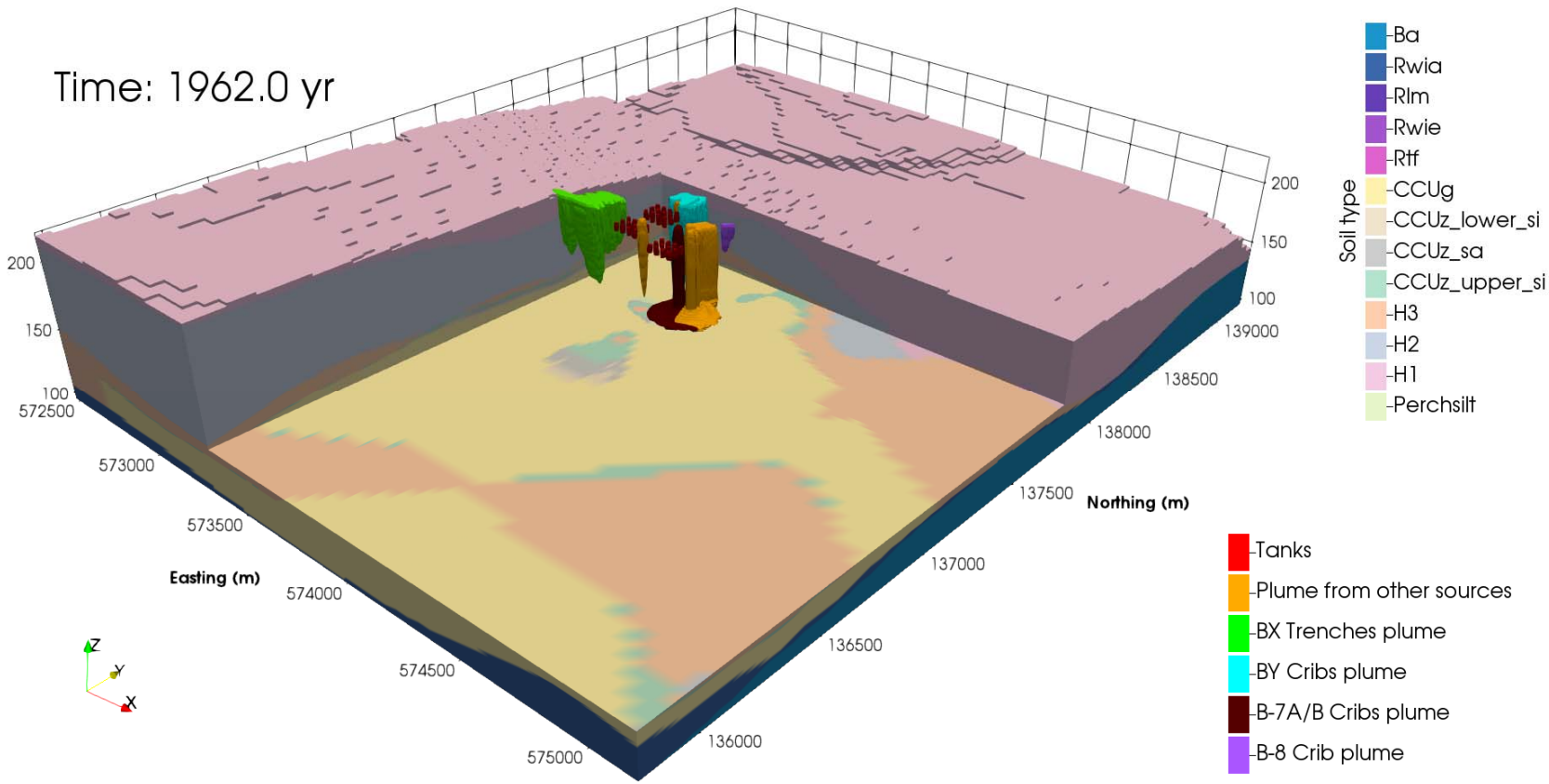

Figure B.9. Cutaway View of Hydrostratigraphic Units Underlying the B-Complex Showing Waste Storage Tanks of the B-BX-BY Tank Farms and Isosurfaces of Simulated Tc-99 Plumes [1 pCi/L] from Different Source Areas in 1962.

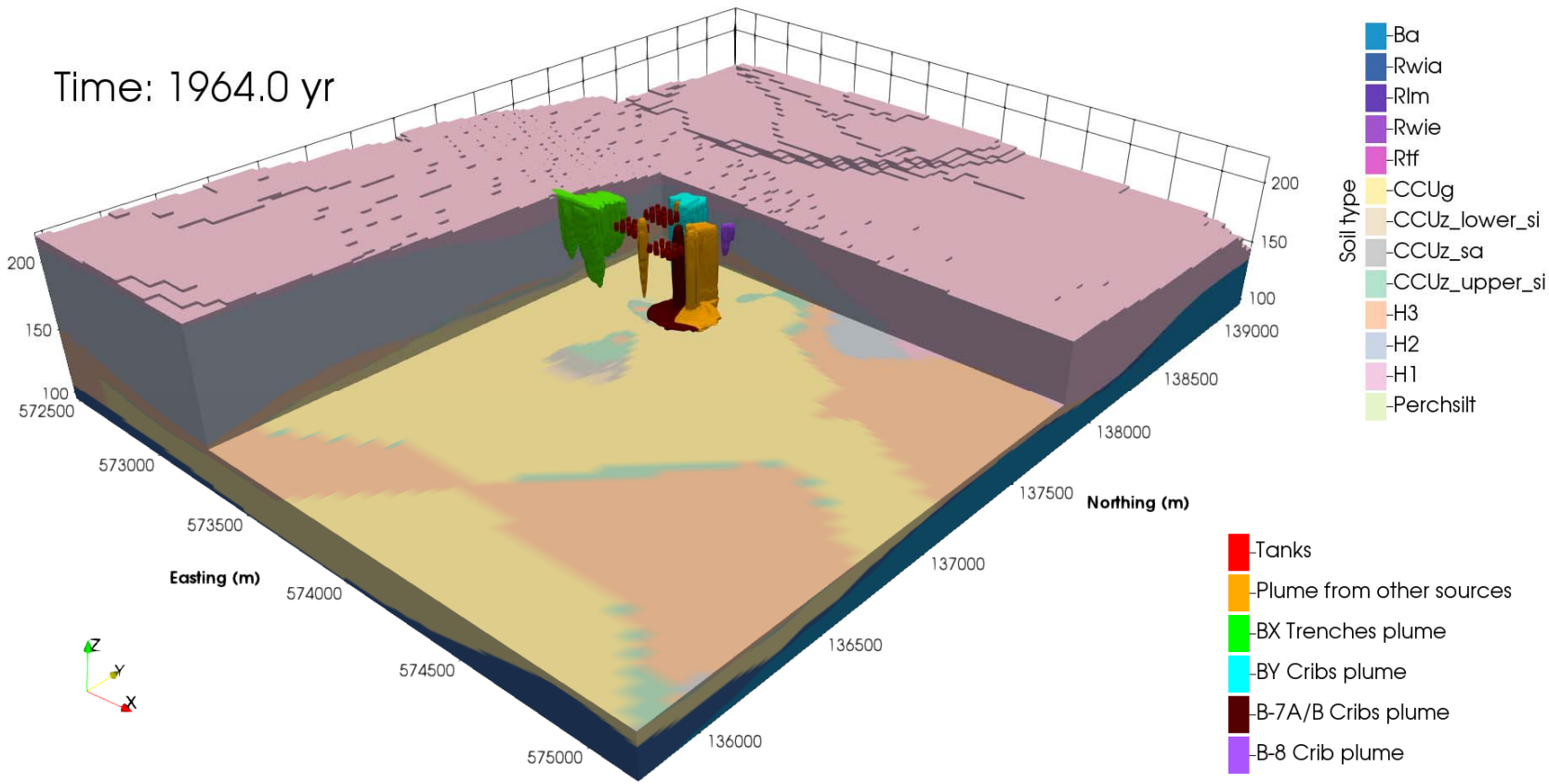

Figure B.10. Cutaway View of Hydrostratigraphic Units Underlying the B-Complex Showing Waste Storage Tanks of the B-BX-BY Tank Farms and Isosurfaces of Simulated Tc-99 Plumes [1 pCi/L] from Different Source Areas in 1964.

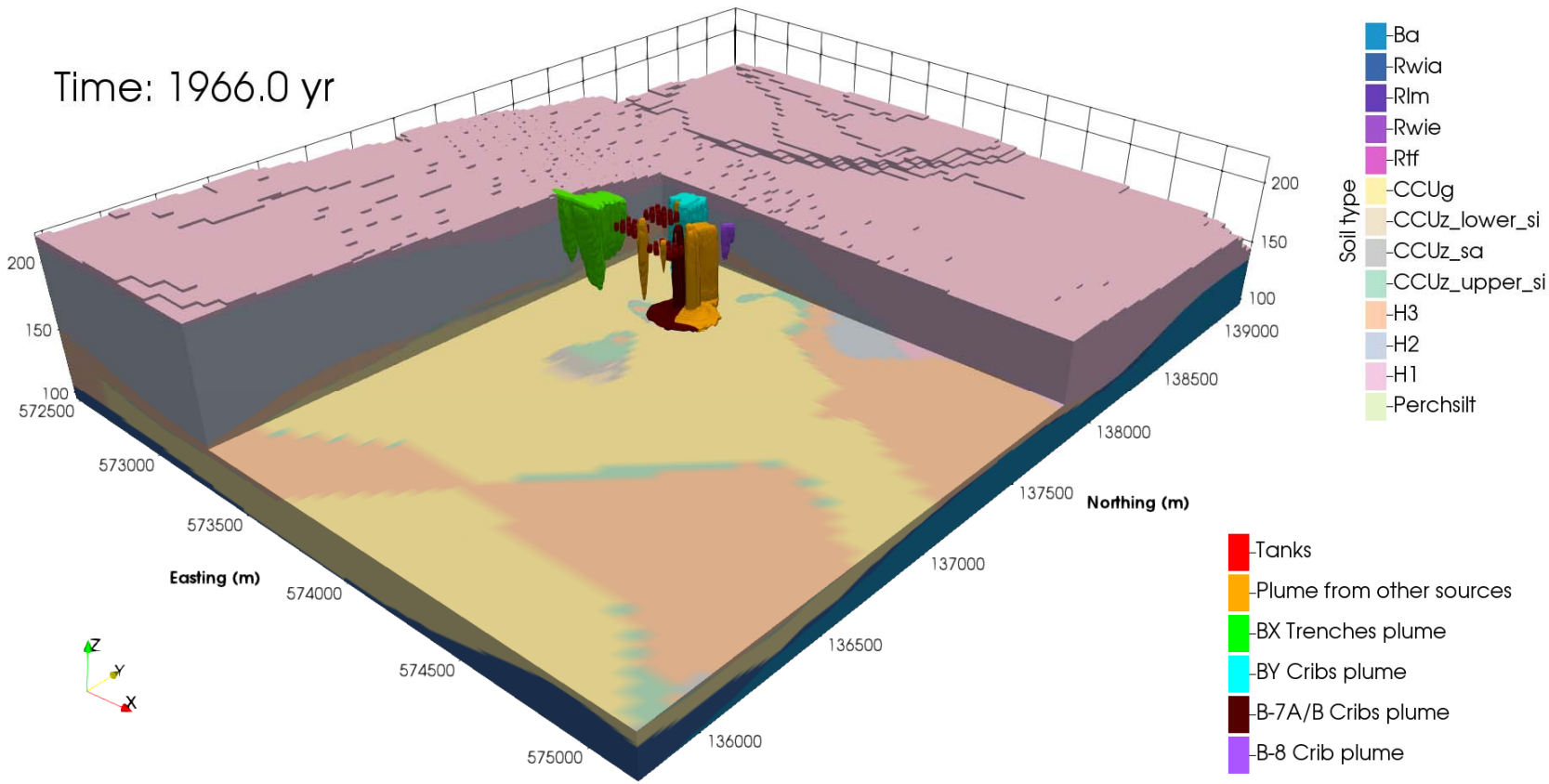

Figure B.11. Cutaway View of Hydrostratigraphic Units Underlying the B-Complex Showing Waste Storage Tanks of the B-BX-BY Tank Farms and Isosurfaces of Simulated Tc-99 Plumes [1 pCi/L] from Different Source Areas in 1966.

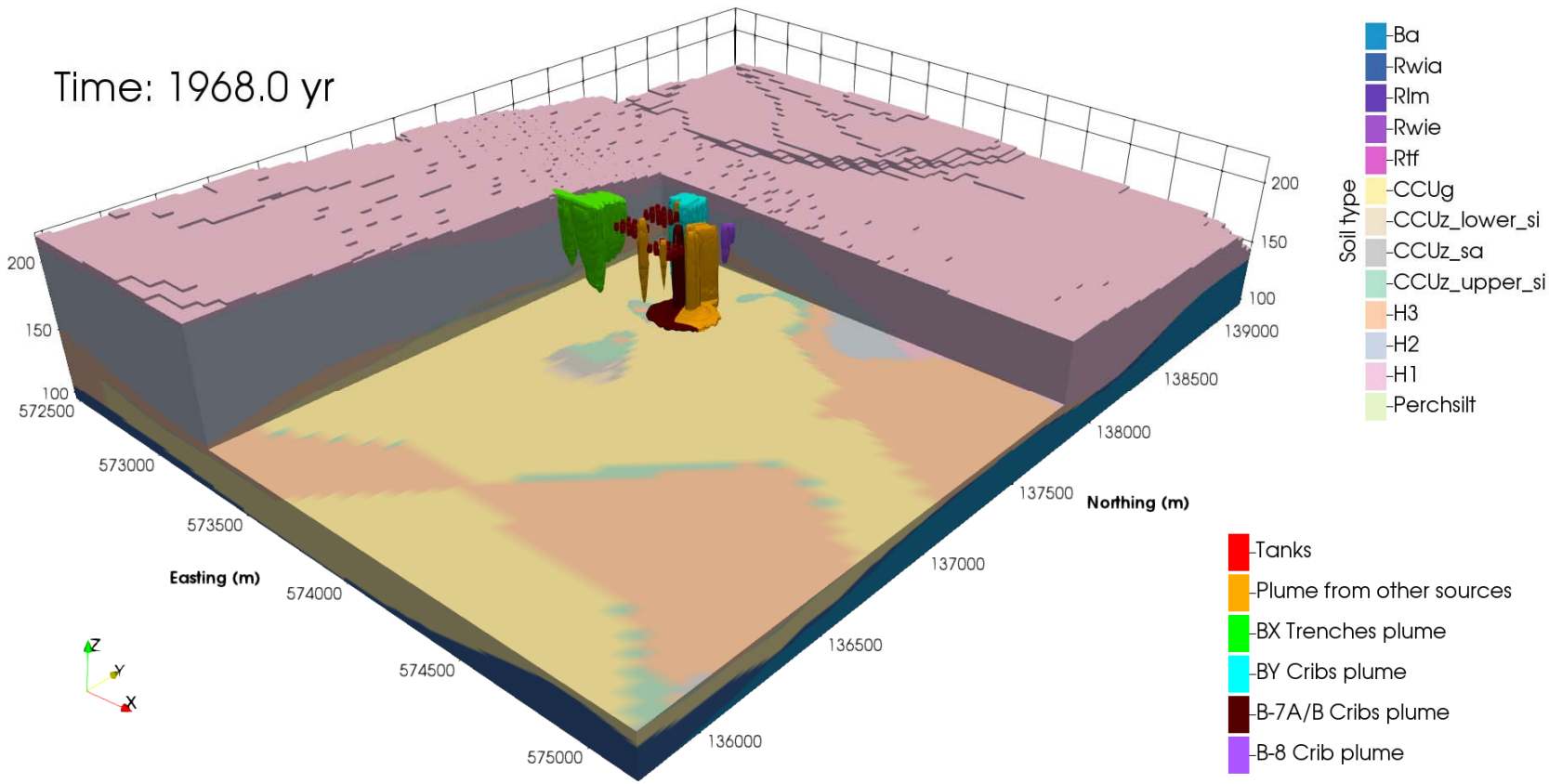

Figure B.12. Cutaway View of Hydrostratigraphic Units Underlying the B-Complex Showing Waste Storage Tanks of the B-BX-BY Tank Farms and Isosurfaces of Simulated Tc-99 Plumes [1 pCi/L] from Different Source Areas in 1968.

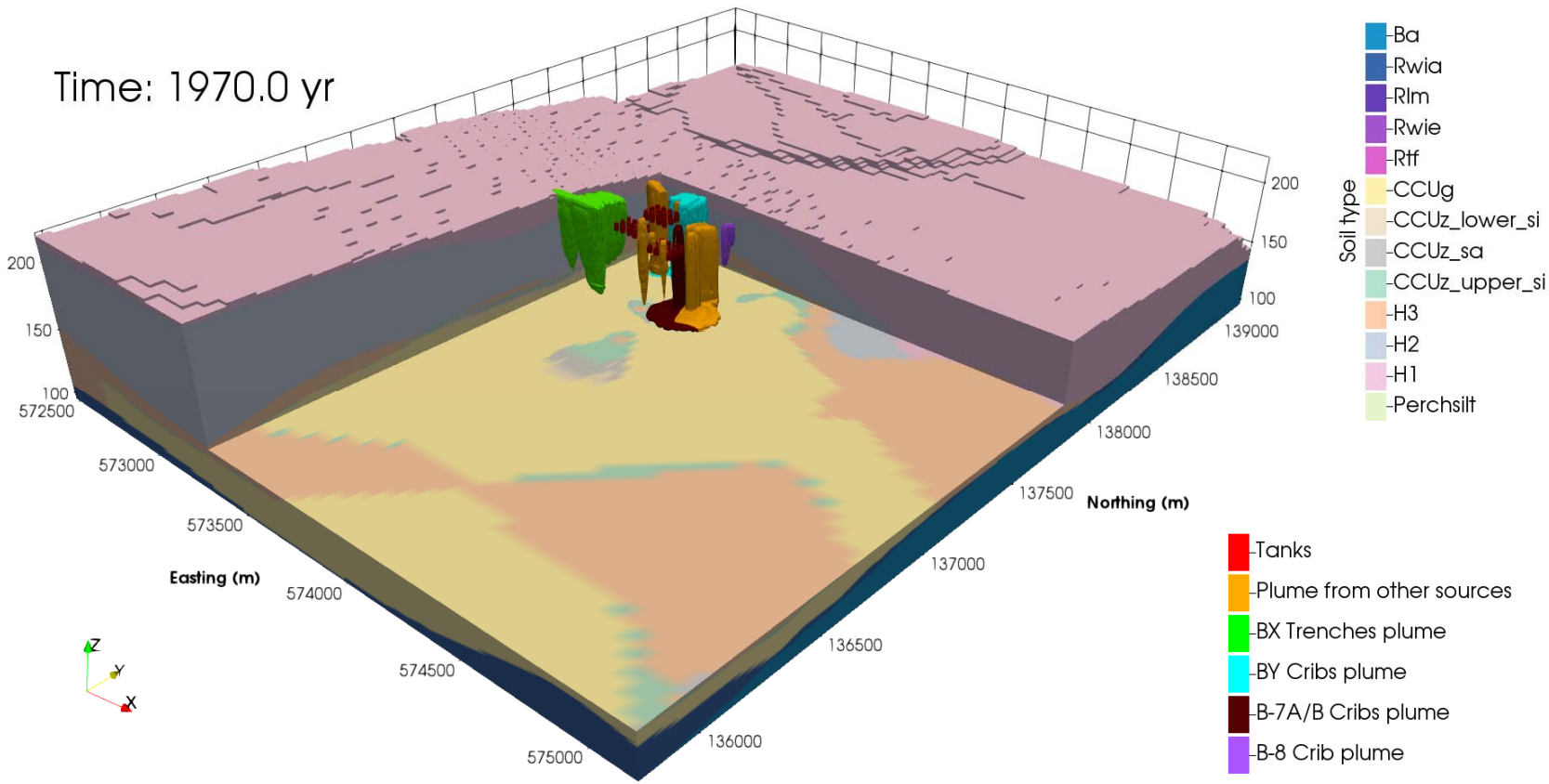

Figure B.13. Cutaway View of Hydrostratigraphic Units Underlying the B-Complex Showing Waste Storage Tanks of the B-BX-BY Tank Farms and Isosurfaces of Simulated Tc-99 Plumes [1 pCi/L] from Different Source Areas in 1970.

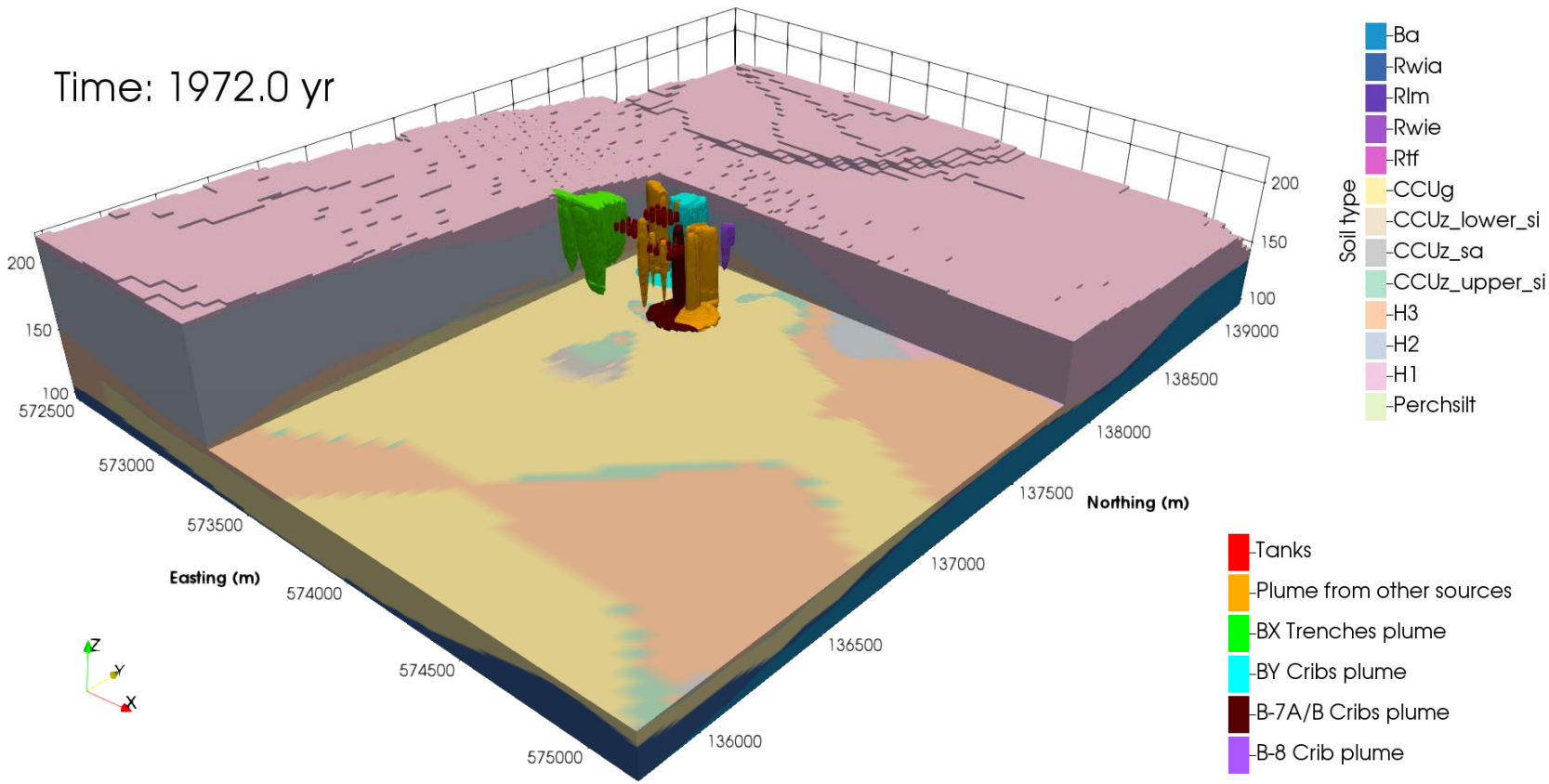

Figure B.14. Cutaway View of Hydrostratigraphic Units Underlying the B-Complex Showing Waste Storage Tanks of the B-BX-BY Tank Farms and Isosurfaces of Simulated Tc-99 Plumes [1 pCi/L] from Different Source Areas in 1972.

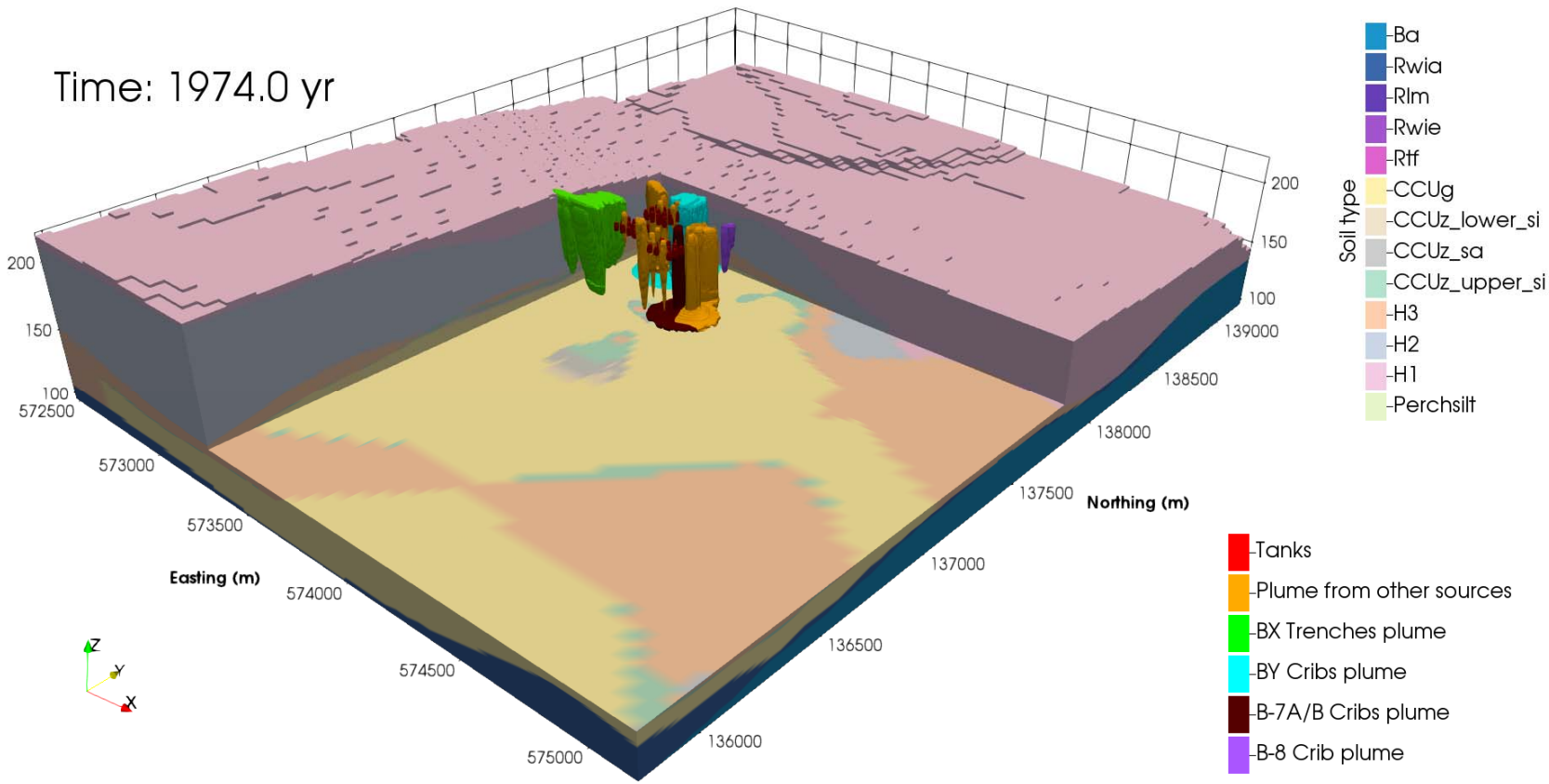

Figure B.15. Cutaway View of Hydrostratigraphic Units Underlying the B-Complex Showing Waste Storage Tanks of the B-BX-BY Tank Farms and Isosurfaces of Simulated Tc-99 Plumes [1 pCi/L] from Different Source Areas in 1974.

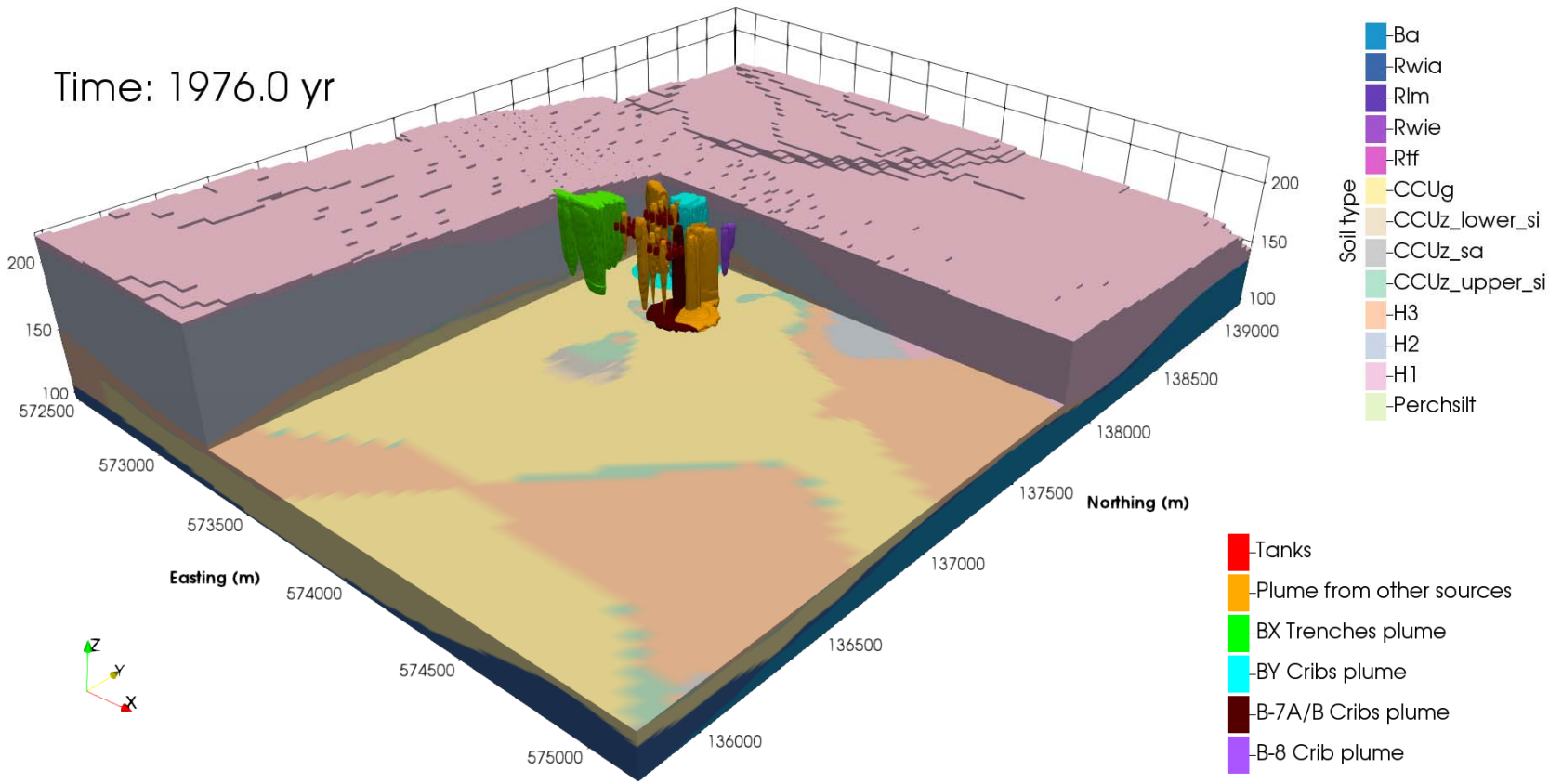

Figure B.16. Cutaway View of Hydrostratigraphic Units Underlying the B-Complex Showing Waste Storage Tanks of the B-BX-BY Tank Farms and Isosurfaces of Simulated Tc-99 Plumes [1 pCi/L] from Different Source Areas in 1976.

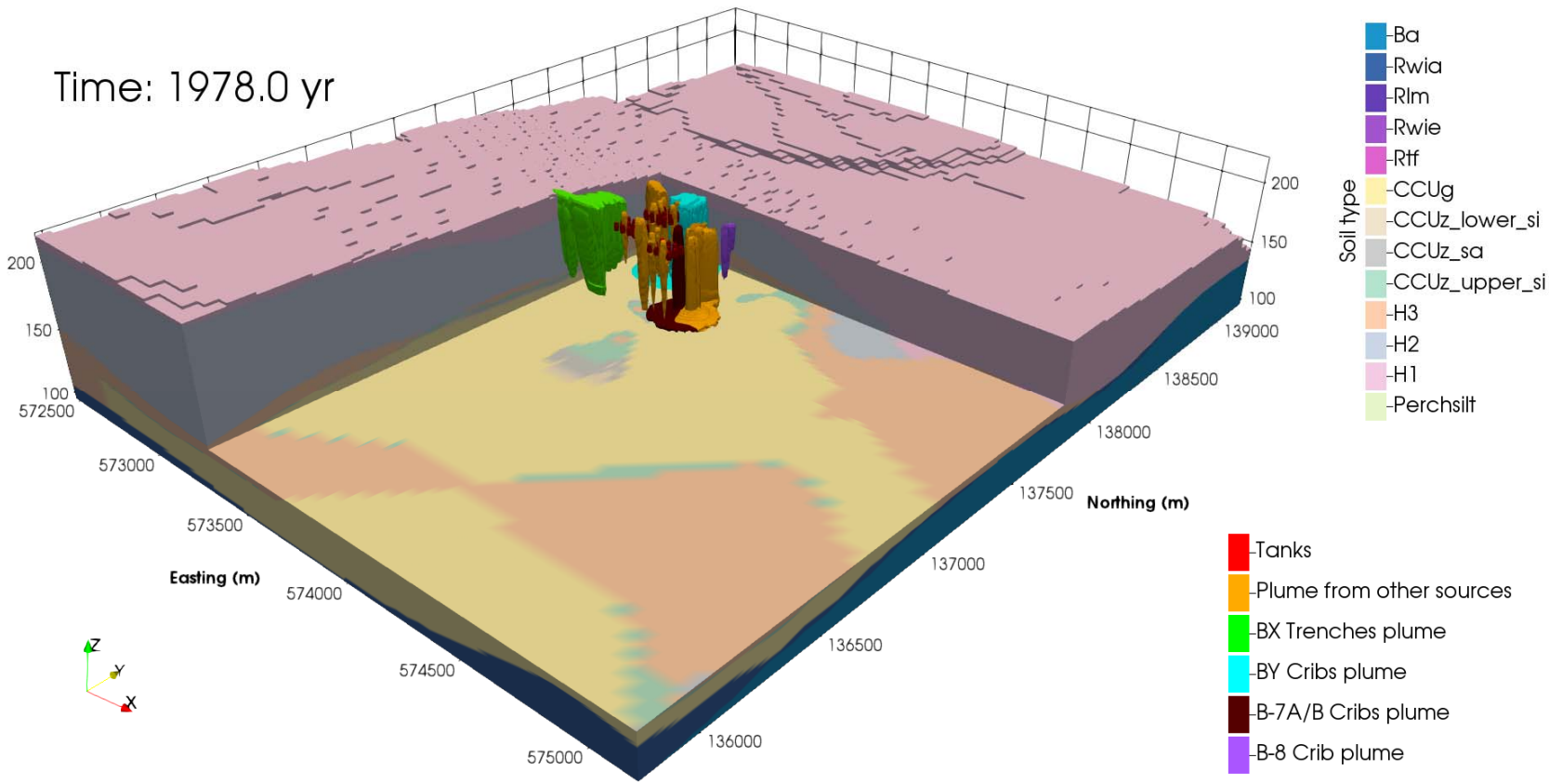

Figure B.17. Cutaway View of Hydrostratigraphic Units Underlying the B-Complex Showing Waste Storage Tanks of the B-BX-BY Tank Farms and Isosurfaces of Simulated Tc-99 Plumes [1 pCi/L] from Different Source Areas in 1978.

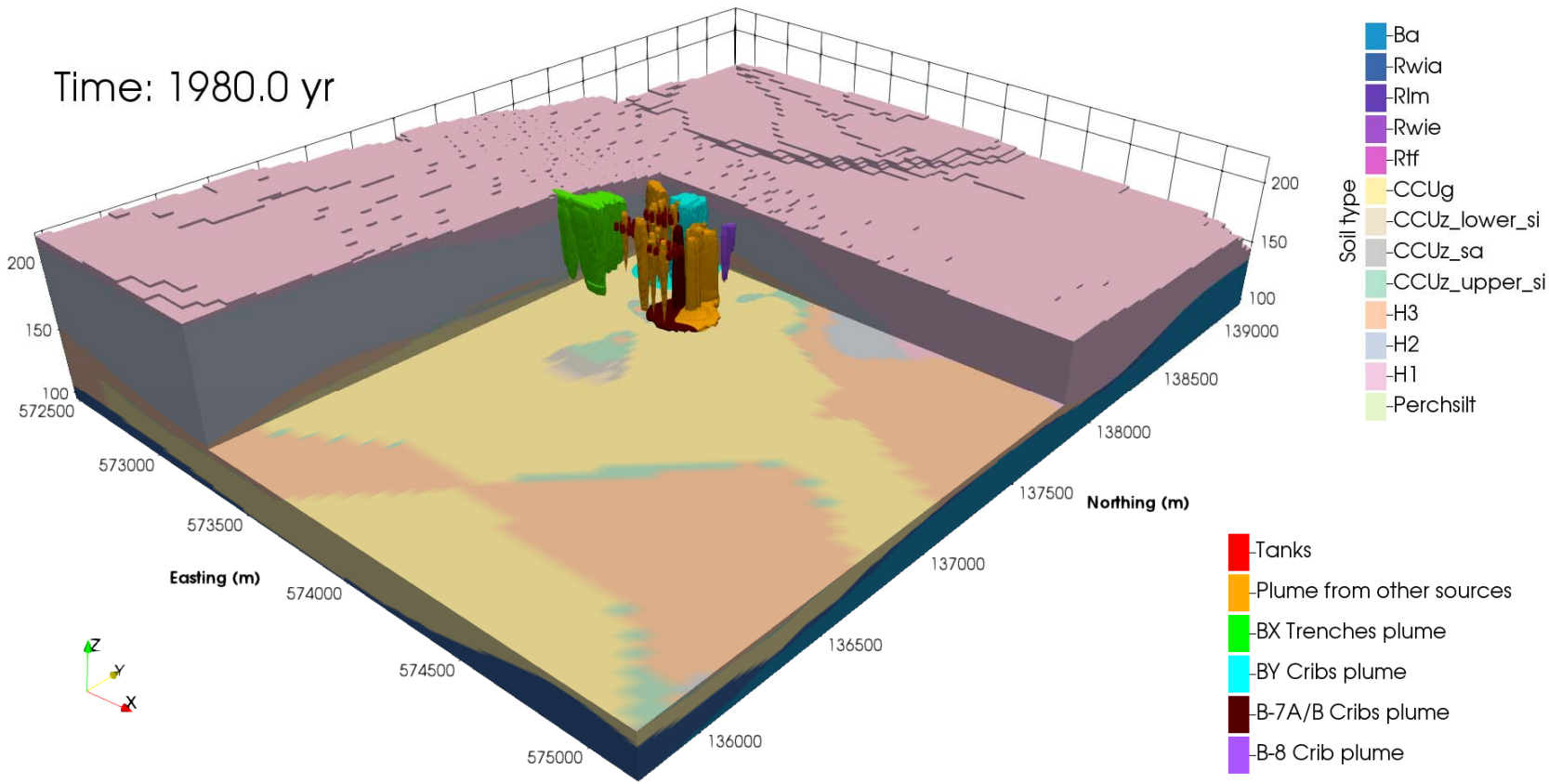

Figure B.18. Cutaway View of Hydrostratigraphic Units Underlying the B-Complex Showing Waste Storage Tanks of the B-BX-BY Tank Farms and Isosurfaces of Simulated Tc-99 Plumes [1 pCi/L] from Different Source Areas in 1980.

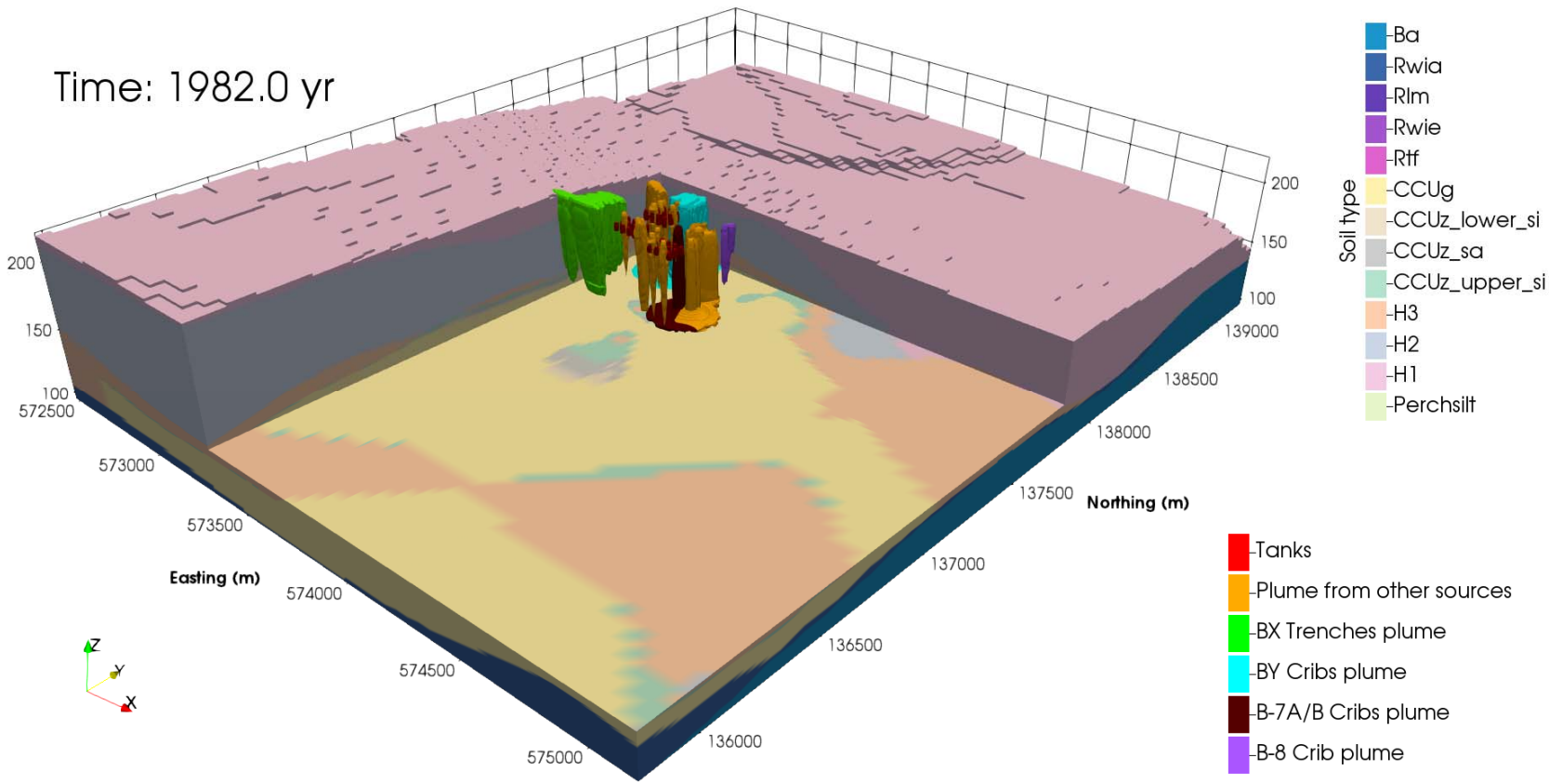

Figure B.19. Cutaway View of Hydrostratigraphic Units Underlying the B-Complex Showing Waste Storage Tanks of the B-BX-BY Tank Farms and Isosurfaces of Simulated Tc-99 Plumes [1 pCi/L] from Different Source Areas in 1982.

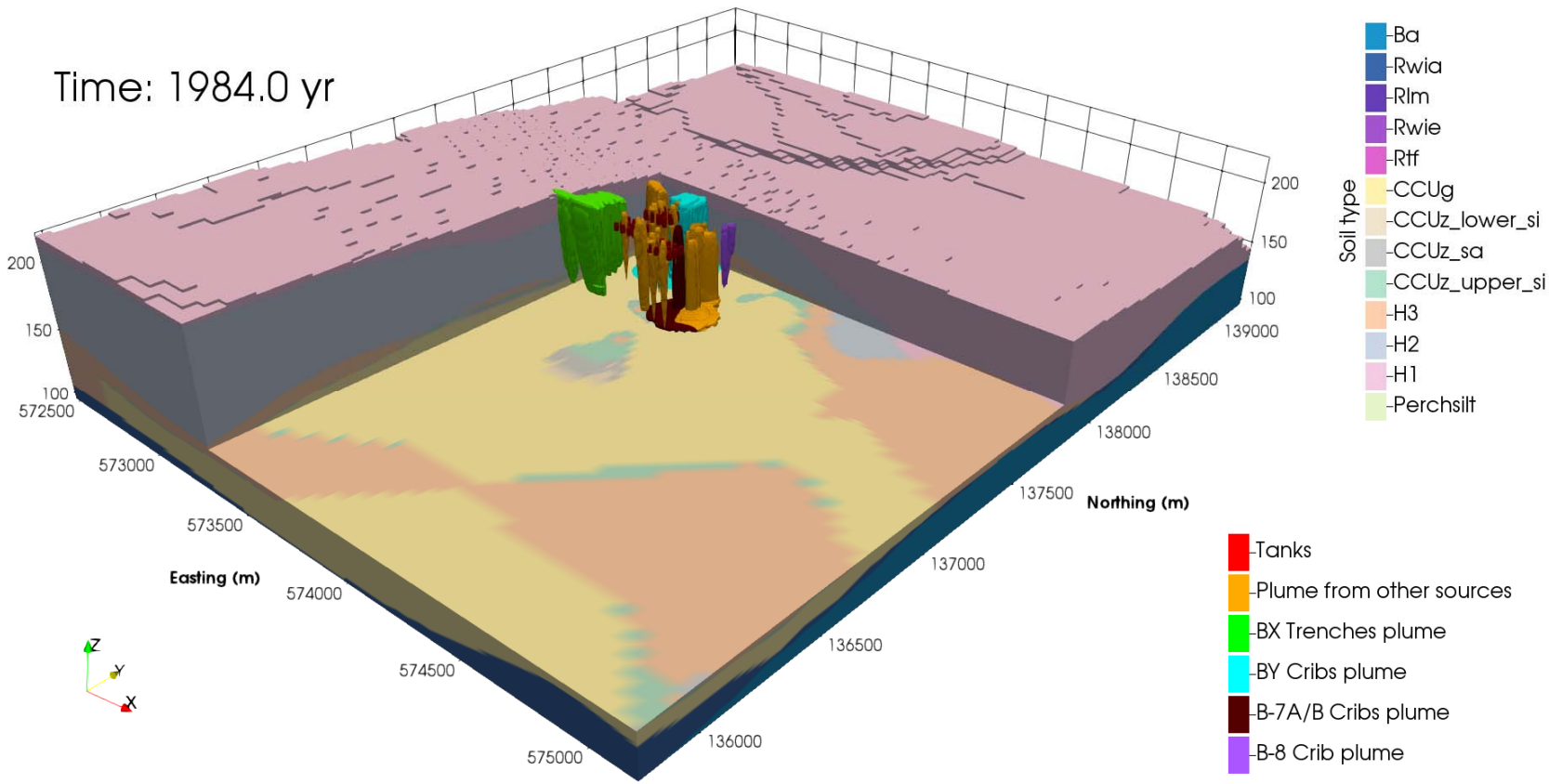

Figure B.20. Cutaway View of Hydrostratigraphic Units Underlying the B-Complex Showing Waste Storage Tanks of the B-BX-BY Tank Farms and Isosurfaces of Simulated Tc-99 Plumes [1 pCi/L] from Different Source Areas in 1984.

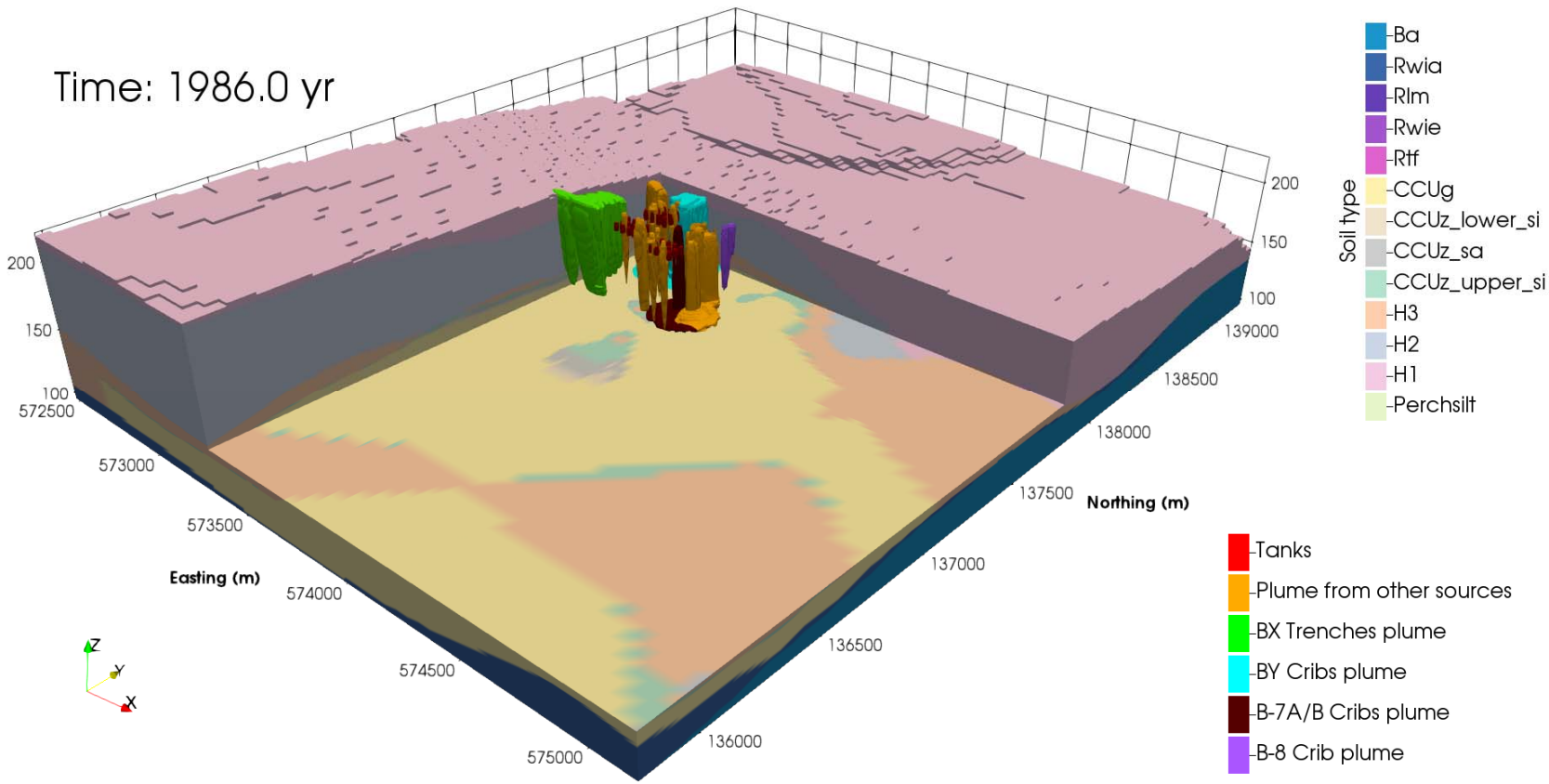

Figure B.21. Cutaway View of Hydrostratigraphic Units Underlying the B-Complex Showing Waste Storage Tanks of the B-BX-BY Tank Farms and Isosurfaces of Simulated Tc-99 Plumes [1 pCi/L] from Different Source Areas in 1986.

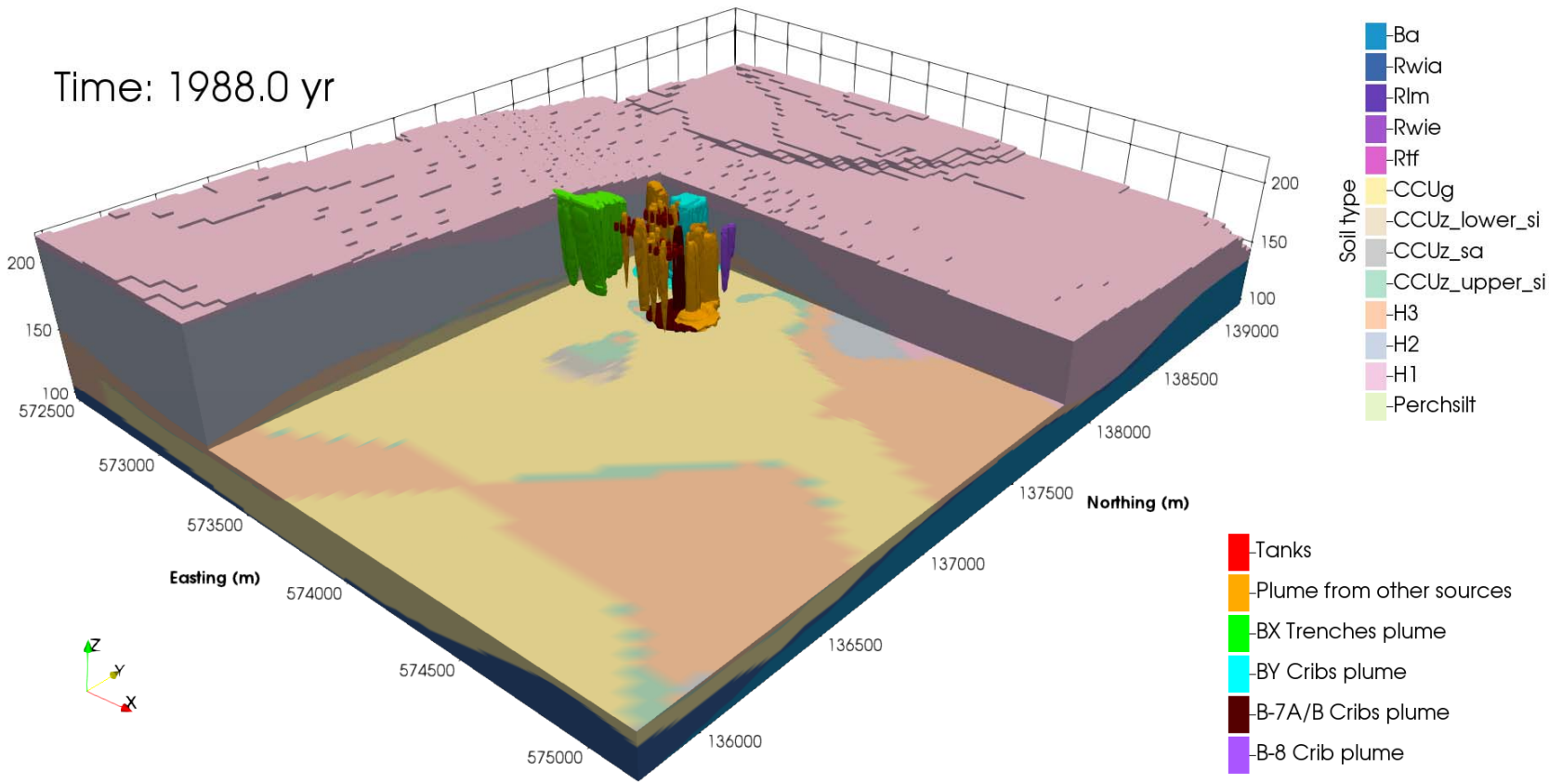

Figure B.22. Cutaway View of Hydrostratigraphic Units Underlying the B-Complex Showing Waste Storage Tanks of the B-BX-BY Tank Farms and Isosurfaces of Simulated Tc-99 Plumes [1 pCi/L] from Different Source Areas in 1988.

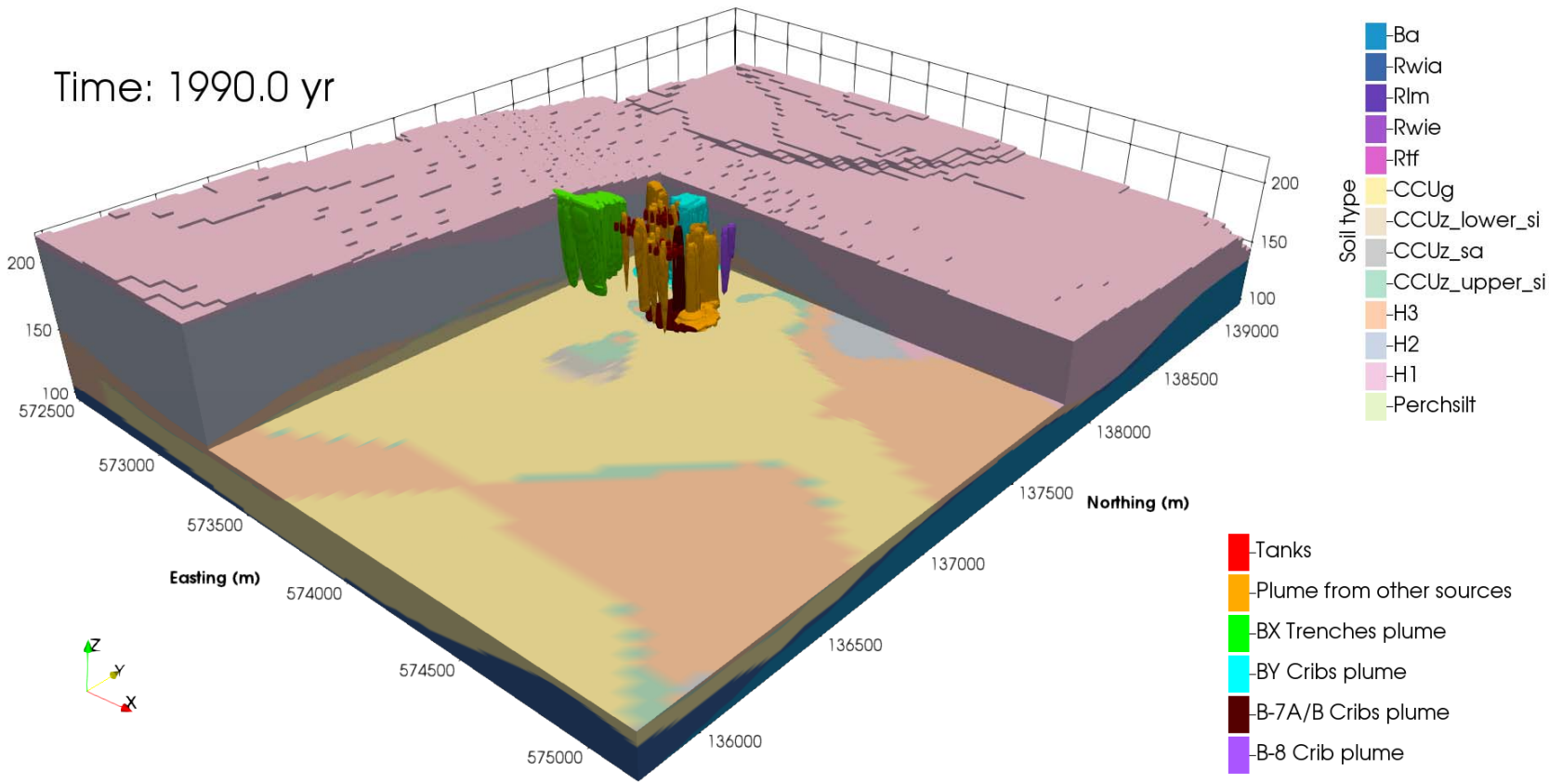

Figure B.23. Cutaway View of Hydrostratigraphic Units Underlying the B-Complex Showing Waste Storage Tanks of the B-BX-BY Tank Farms and Isosurfaces of Simulated Tc-99 Plumes [1 pCi/L] from Different Source Areas in 1990.

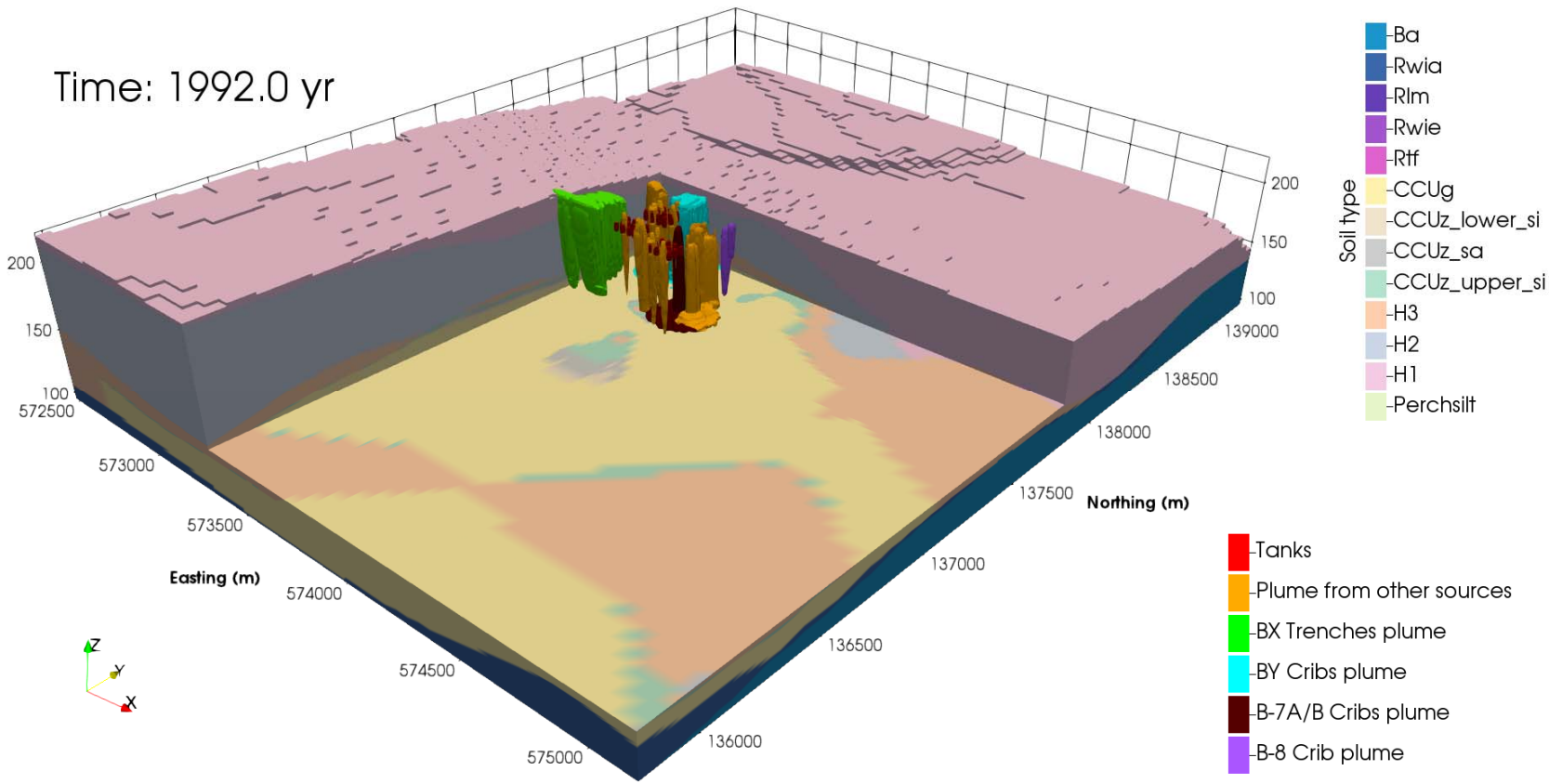

Figure B.24. Cutaway View of Hydrostratigraphic Units Underlying the B-Complex Showing Waste Storage Tanks of the B-BX-BY Tank Farms and Isosurfaces of Simulated Tc-99 Plumes [1 pCi/L] from Different Source Areas in 1992.

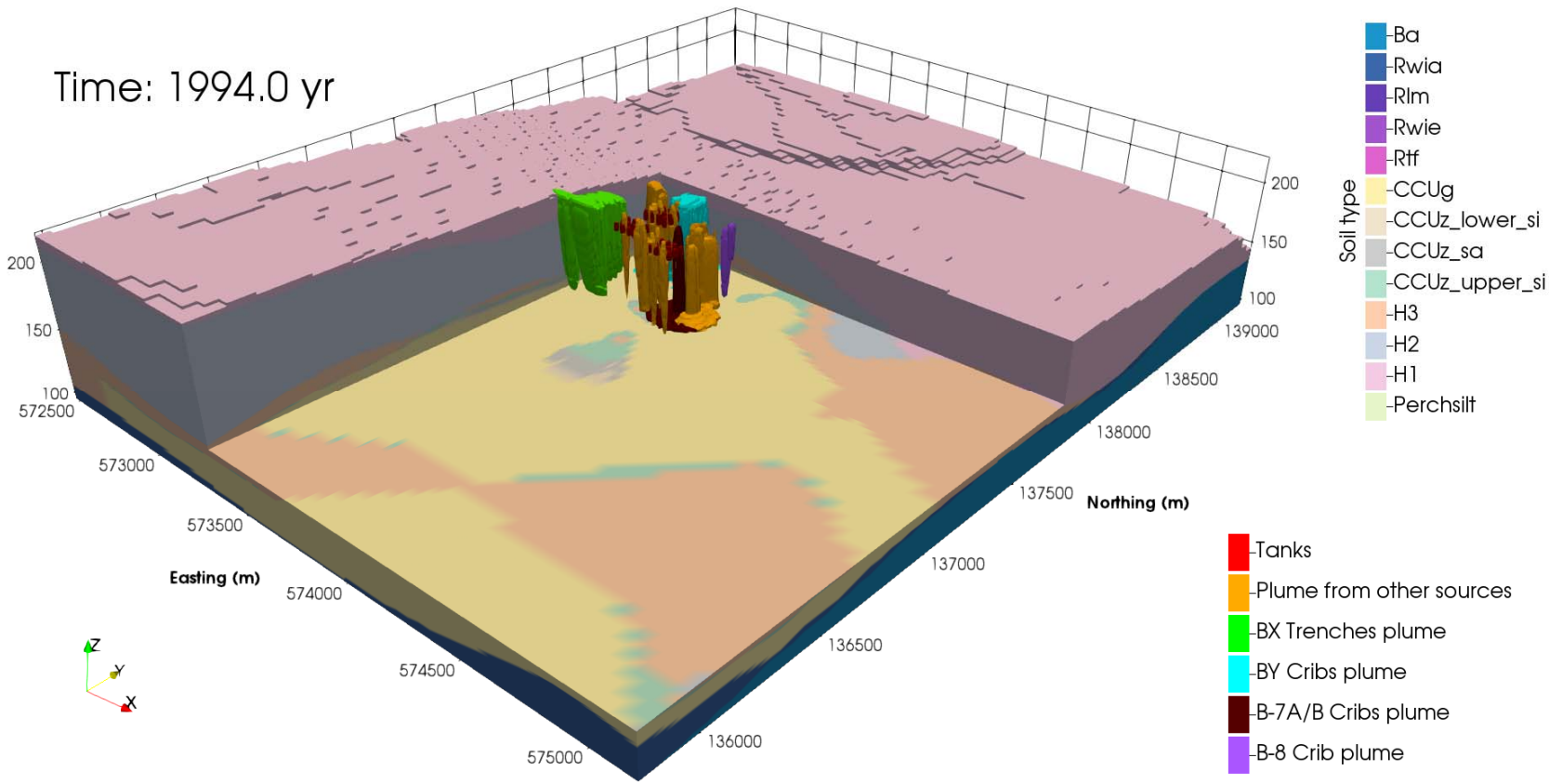

Figure B.25. Cutaway View of Hydrostratigraphic Units Underlying the B-Complex Showing Waste Storage Tanks of the B-BX-BY Tank Farms and Isosurfaces of Simulated Tc-99 Plumes [1 pCi/L] from Different Source Areas in 1994.

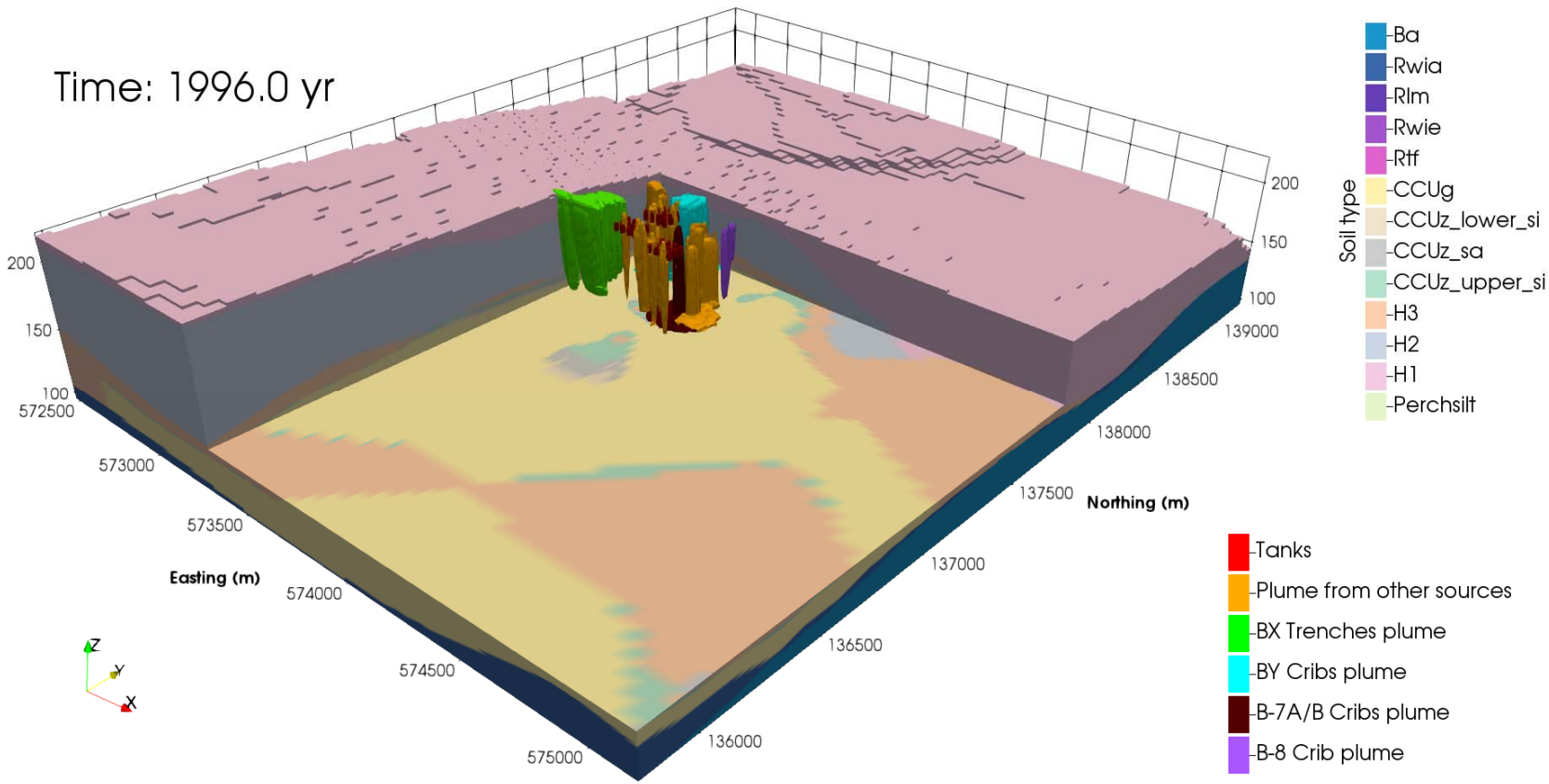

Figure B.26. Cutaway View of Hydrostratigraphic Units Underlying the B-Complex Showing Waste Storage Tanks of the B-BX-BY Tank Farms and Isosurfaces of Simulated Tc-99 Plumes [1 pCi/L] from Different Source Areas in 1996.

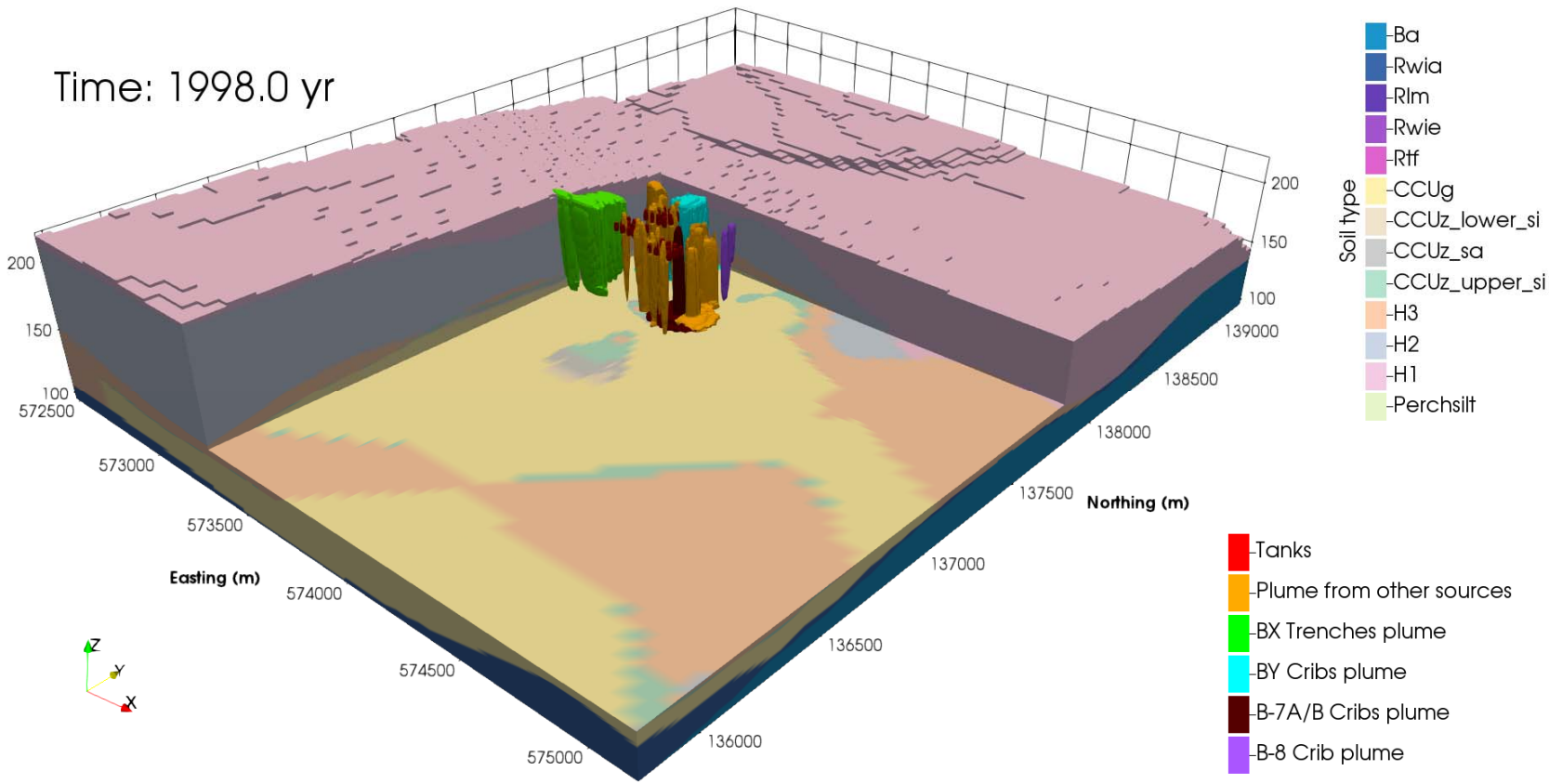

Figure B.27. Cutaway View of Hydrostratigraphic Units Underlying the B-Complex Showing Waste Storage Tanks of the B-BX-BY Tank Farms and Isosurfaces of Simulated Tc-99 Plumes [1 pCi/L] from Different Source Areas in 1998.

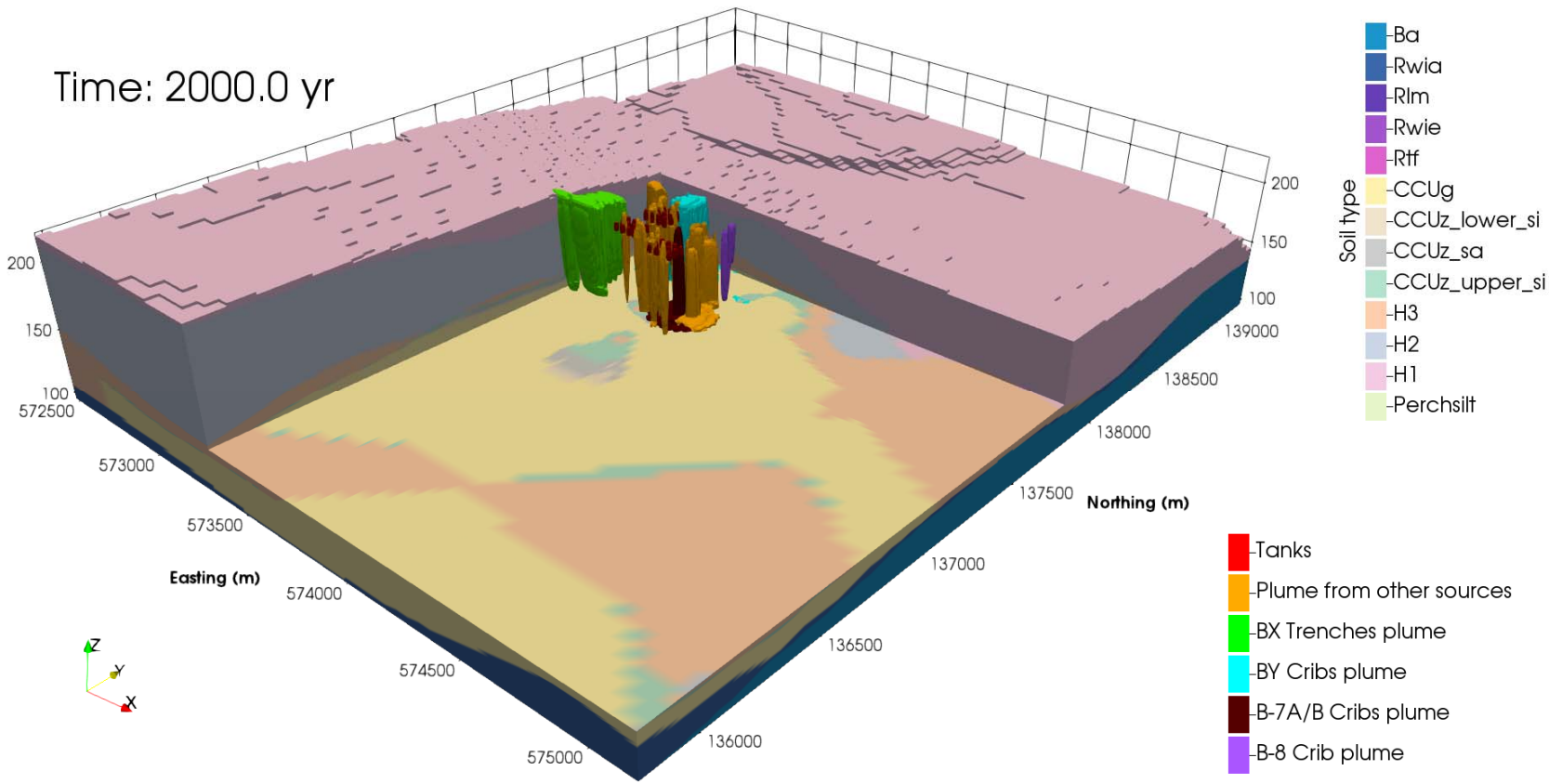

Figure B.28. Cutaway View of Hydrostratigraphic Units Underlying the B-Complex Showing Waste Storage Tanks of the B-BX-BY Tank Farms and Isosurfaces of Simulated Tc-99 Plumes [1 pCi/L] from Different Source Areas in 2000.

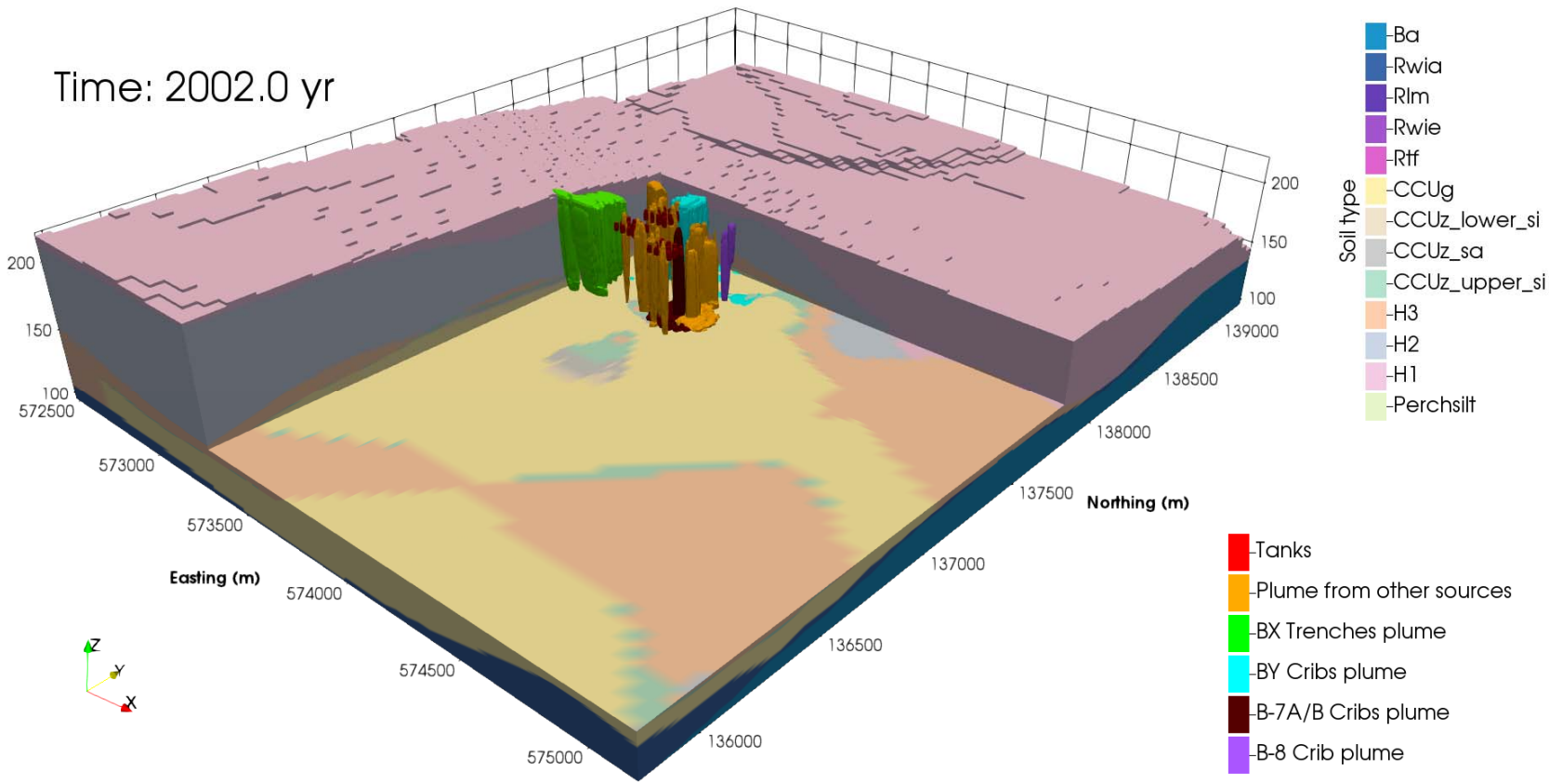

Figure B.29. Cutaway View of Hydrostratigraphic Units Underlying the B-Complex Showing Waste Storage Tanks of the B-BX-BY Tank Farms and Isosurfaces of Simulated Tc-99 Plumes [1 pCi/L] from Different Source Areas in 2002.

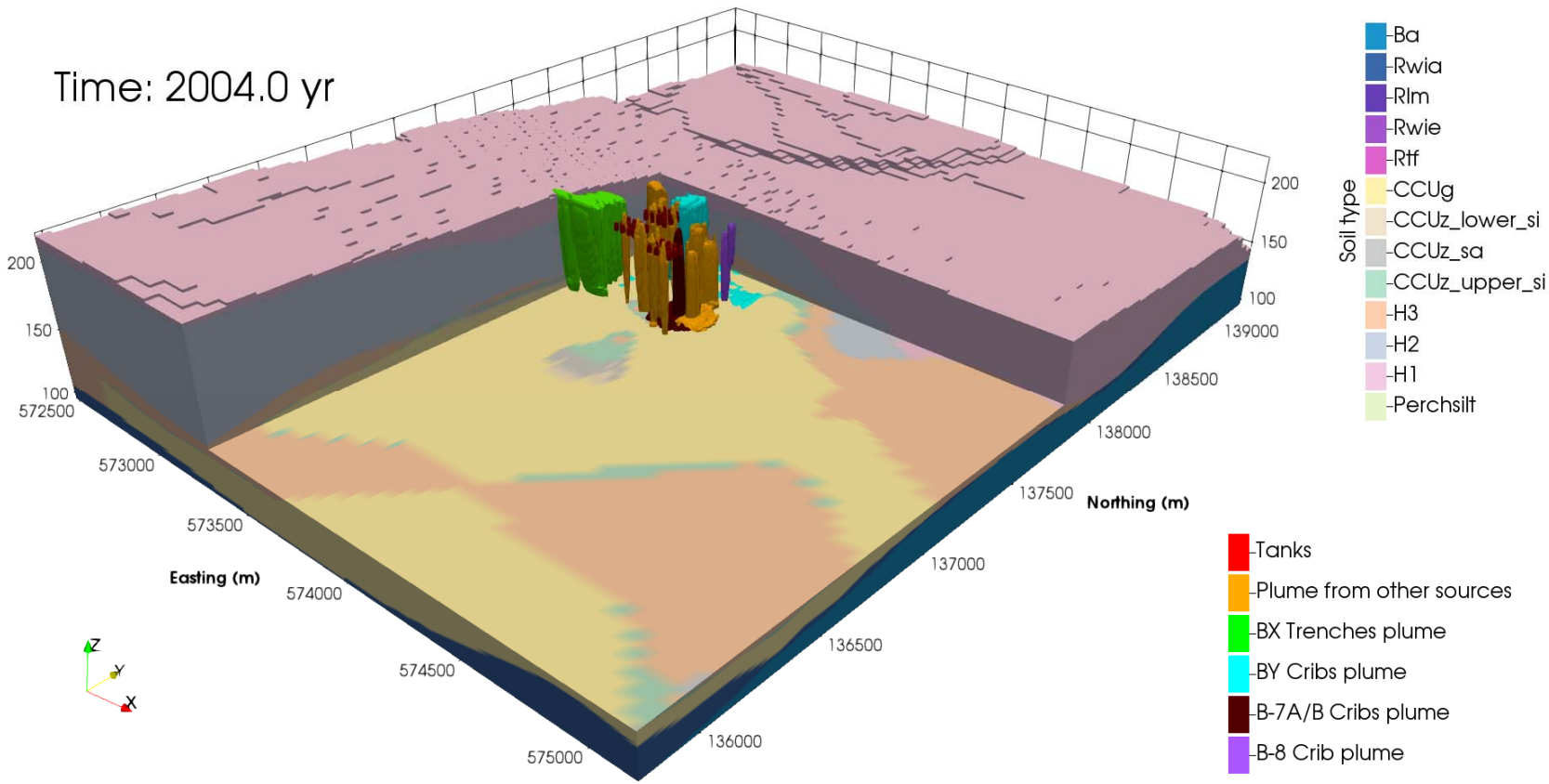

Figure B.30. Cutaway View of Hydrostratigraphic Units Underlying the B-Complex Showing Waste Storage Tanks of the B-BX-BY Tank Farms and Isosurfaces of Simulated Tc-99 Plumes [1 pCi/L] from Different Source Areas in 2004.

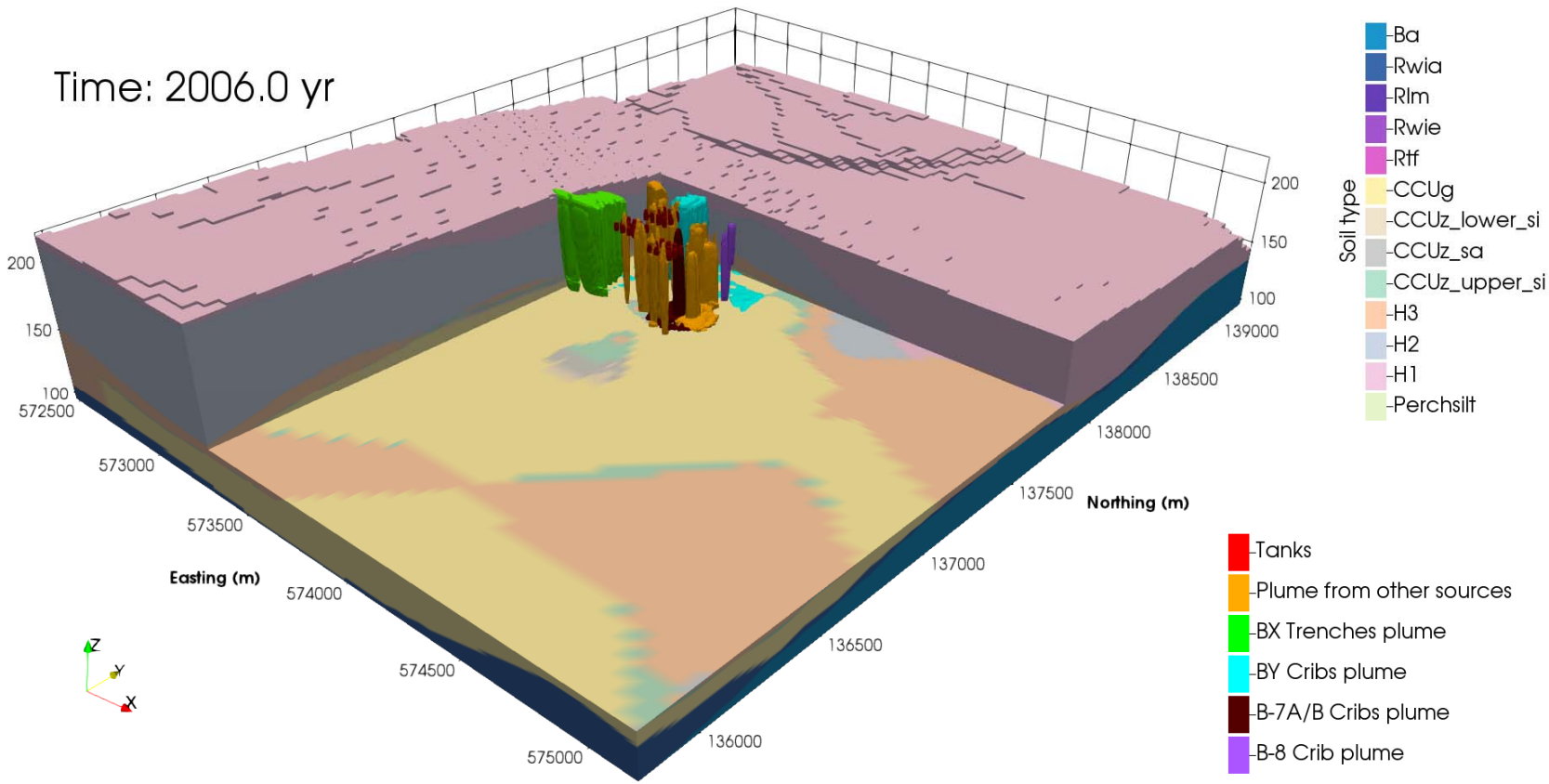

Figure B.31. Cutaway View of Hydrostratigraphic Units Underlying the B-Complex Showing Waste Storage Tanks of the B-BX-BY Tank Farms and Isosurfaces of Simulated Tc-99 Plumes [1 pCi/L] from Different Source Areas in 2006.

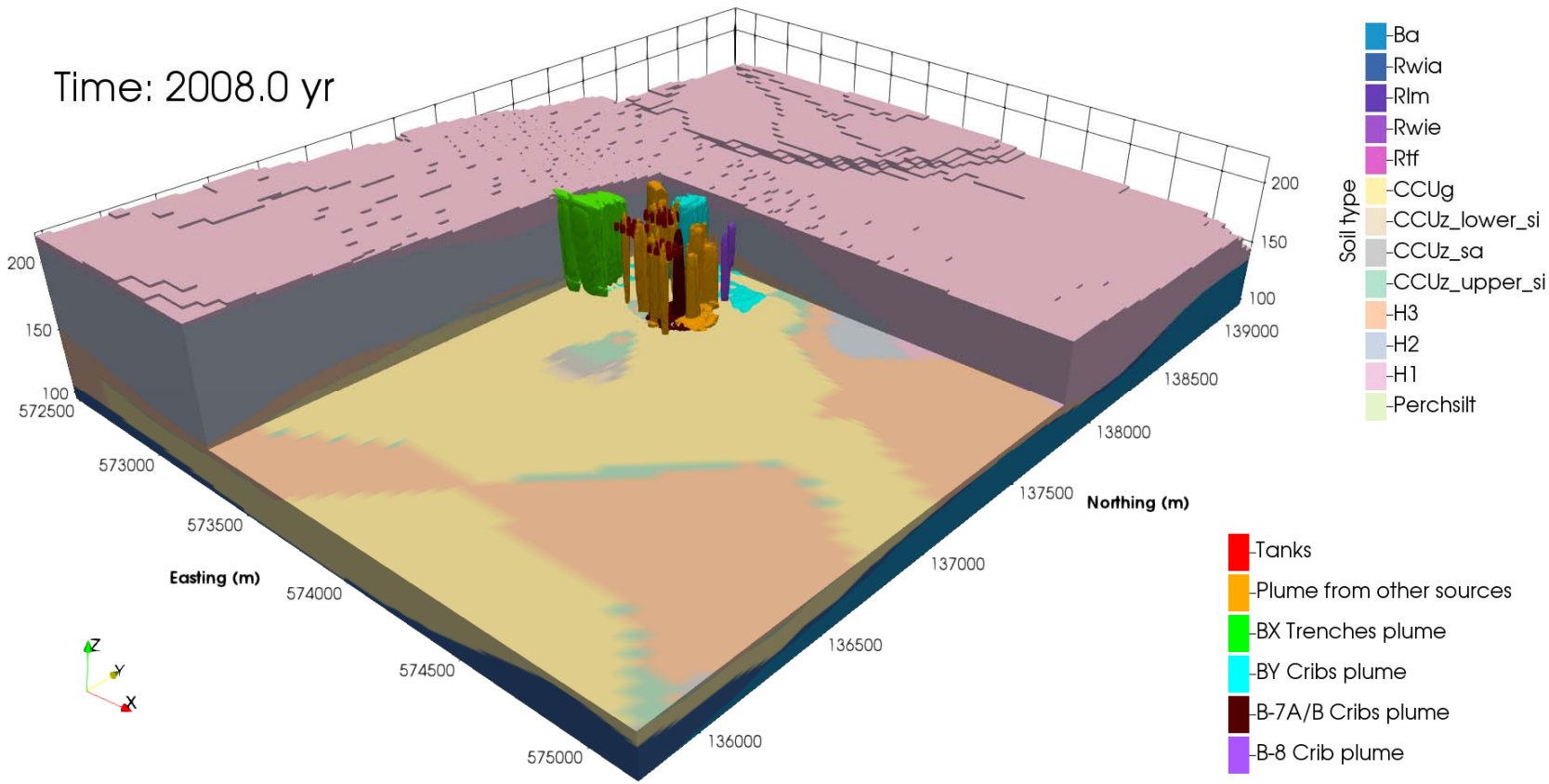

Figure B.32. Cutaway View of Hydrostratigraphic Units Underlying the B-Complex Showing Waste Storage Tanks of the B-BX-BY Tank Farms and Isosurfaces of Simulated Tc-99 Plumes [1 pCi/L] from Different Source Areas in 2008.

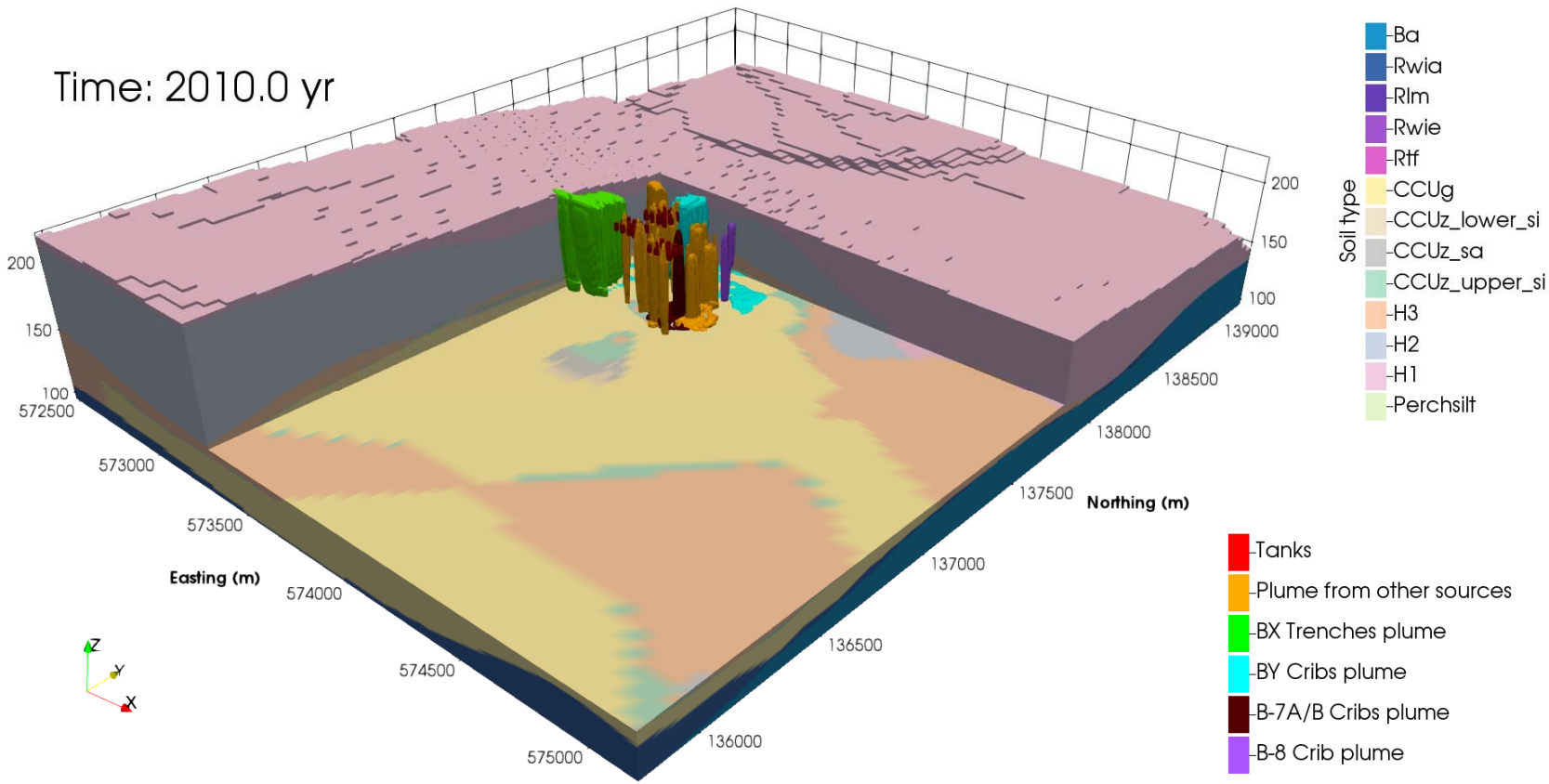

Figure B.33. Cutaway View of Hydrostratigraphic Units Underlying the B-Complex Showing Waste Storage Tanks of the B-BX-BY Tank Farms and Isosurfaces of Simulated Tc-99 Plumes [1 pCi/L] from Different Source Areas in 2010.

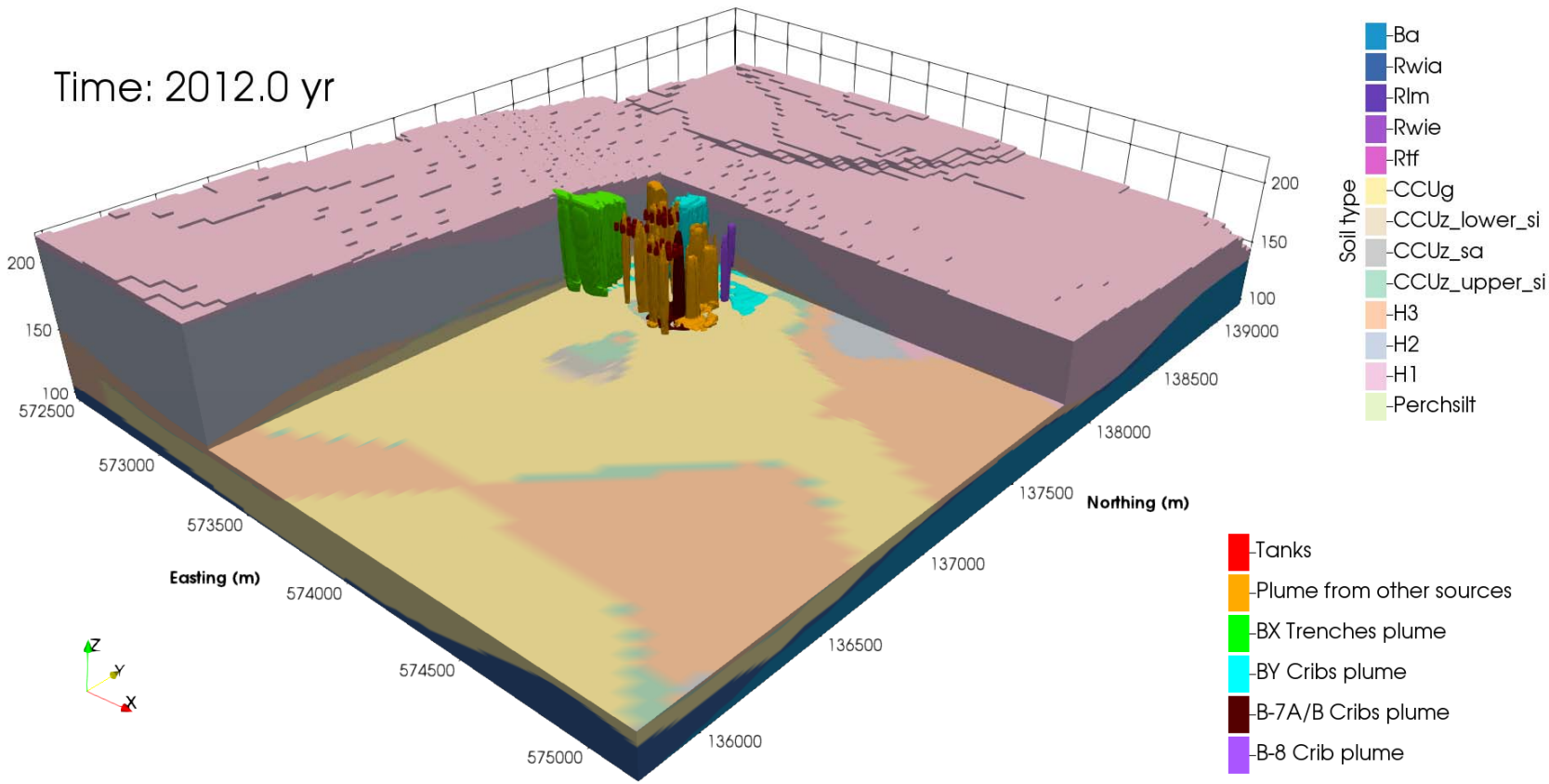

Figure B.34. Cutaway View of Hydrostratigraphic Units Underlying the B-Complex Showing Waste Storage Tanks of the B-BX-BY Tank Farms and Isosurfaces of Simulated Tc-99 Plumes [1 pCi/L] from Different Source Areas in 2012.

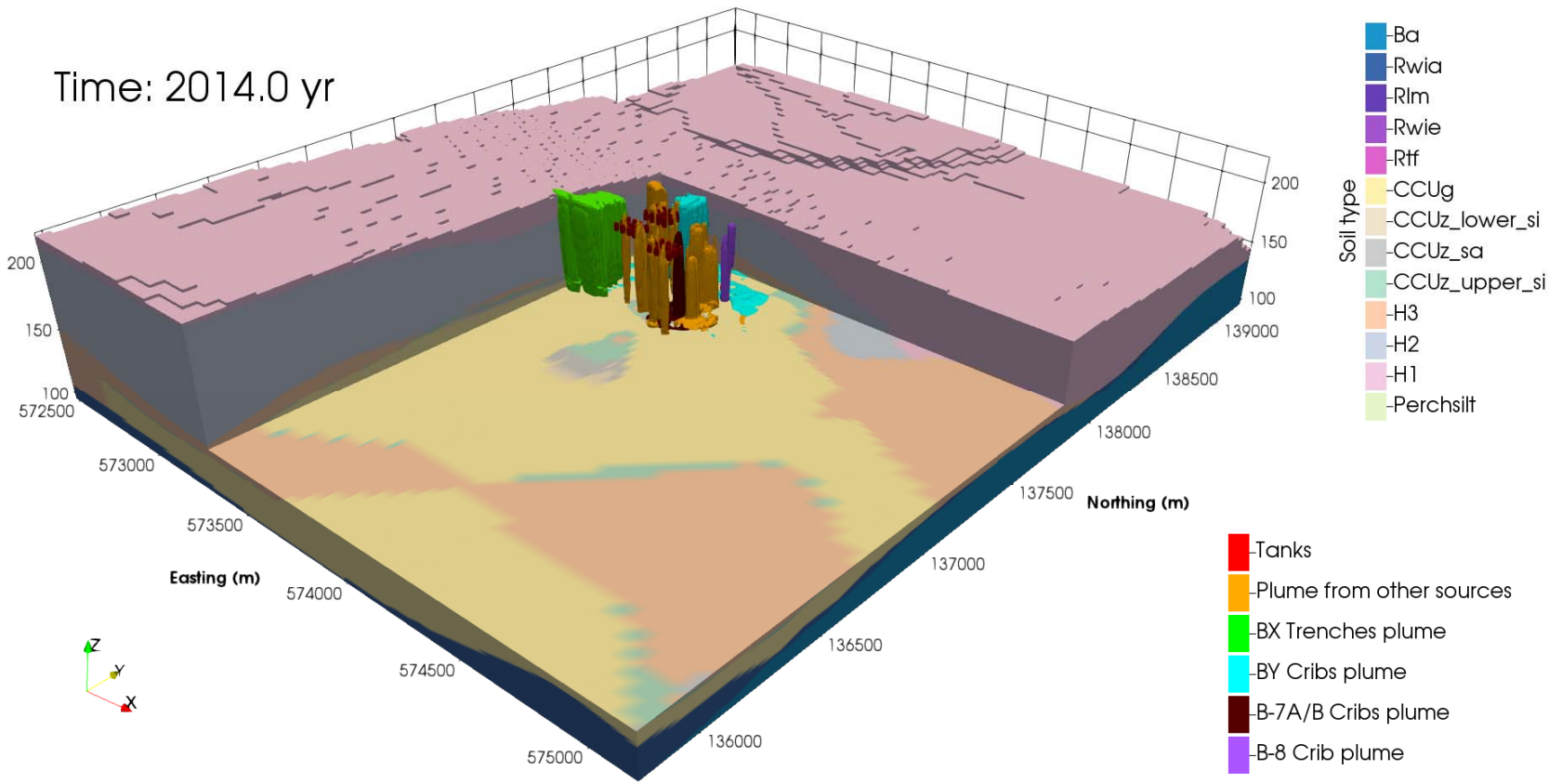

Figure B.35. Cutaway View of Hydrostratigraphic Units Underlying the B-Complex Showing Waste Storage Tanks of the B-BX-BY Tank Farms and Isosurfaces of Simulated Tc-99 Plumes [1 pCi/L] from Different Source Areas in 2014.

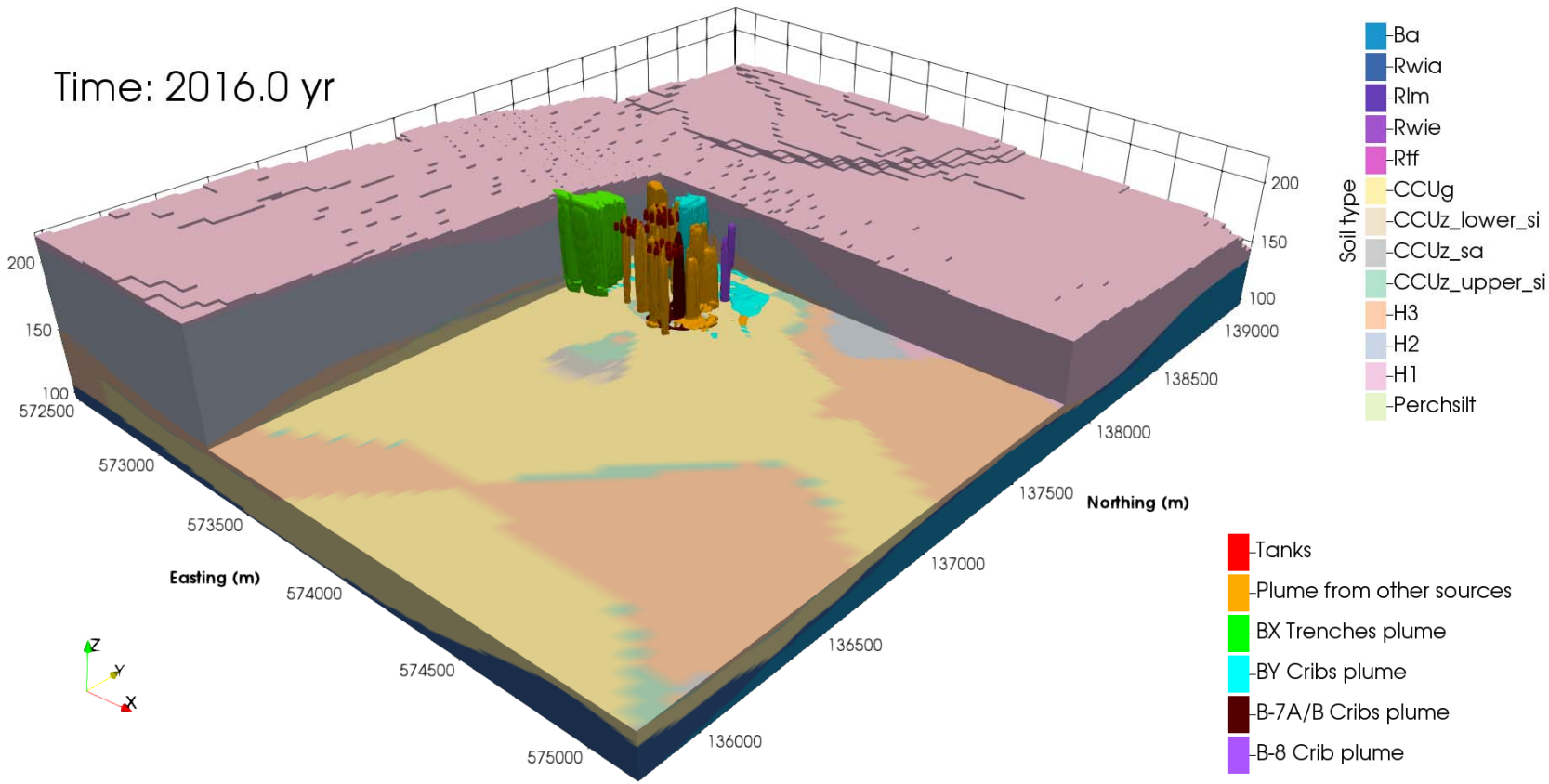

Figure B.36. Cutaway View of Hydrostratigraphic Units Underlying the B-Complex Showing Waste Storage Tanks of the B-BX-BY Tank Farms and Isosurfaces of Simulated Tc-99 Plumes [1 pCi/L] from Different Source Areas in 2016.

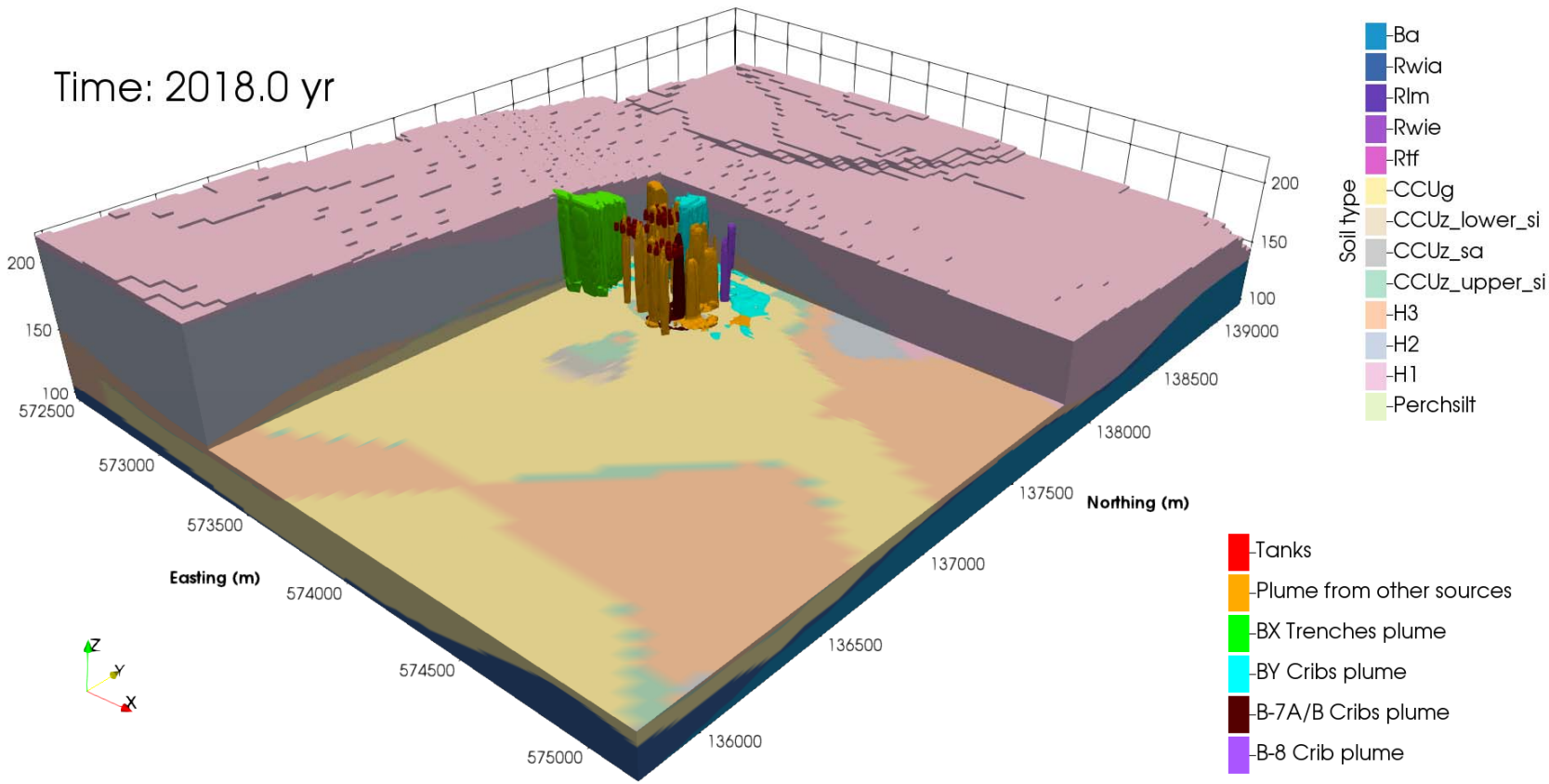

Figure B.37. Cutaway View of Hydrostratigraphic Units Underlying the B-Complex Showing Waste Storage Tanks of the B-BX-BY Tank Farms and Isosurfaces of Simulated Tc-99 Plumes [1 pCi/L] from Different Source Areas in 2018.

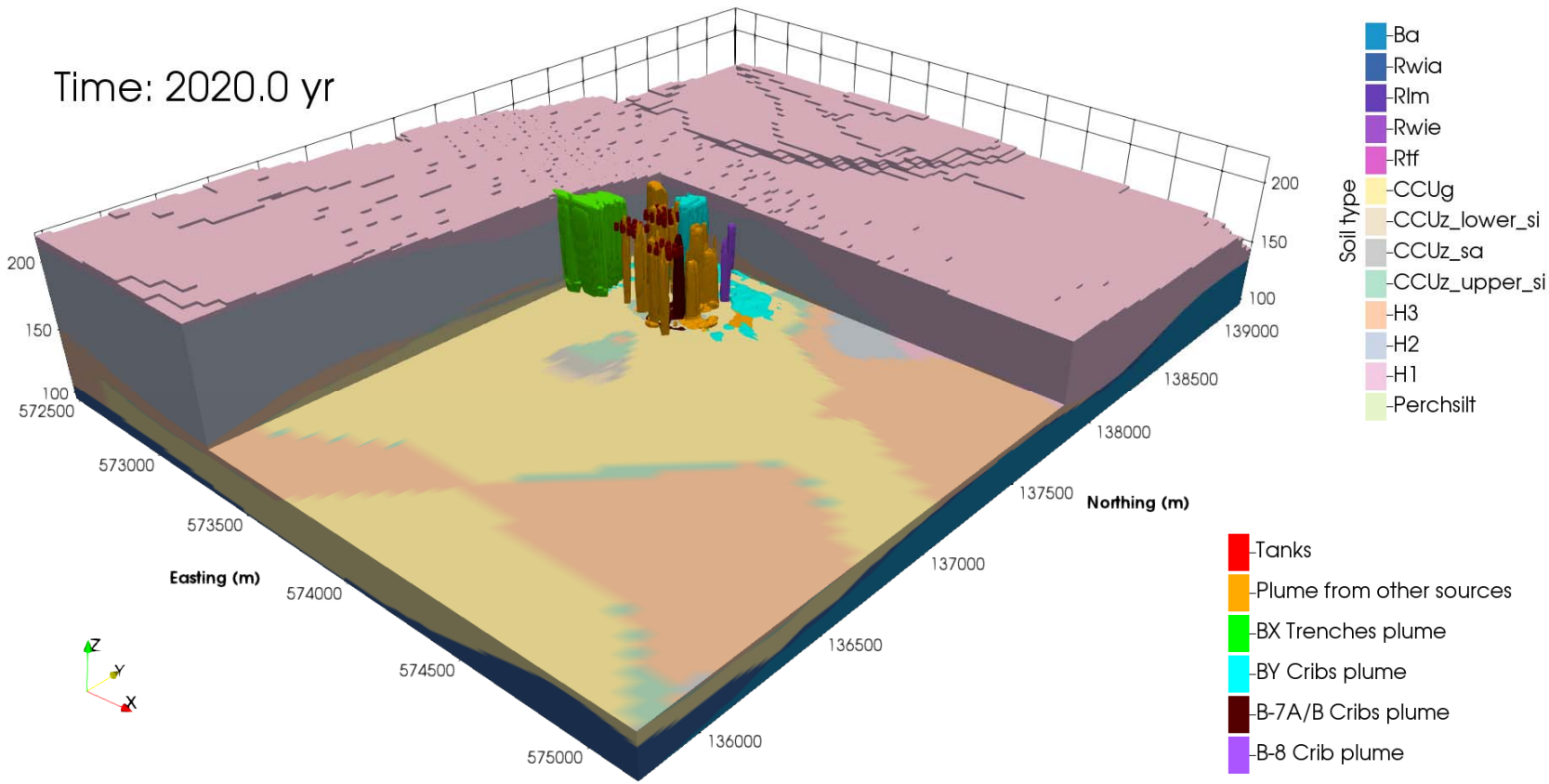

Figure B.38. Cutaway View of Hydrostratigraphic Units Underlying the B-Complex Showing Waste Storage Tanks of the B-BX-BY Tank Farms and Isosurfaces of Simulated Tc-99 Plumes [1 pCi/L] from Different Source Areas in 2020.

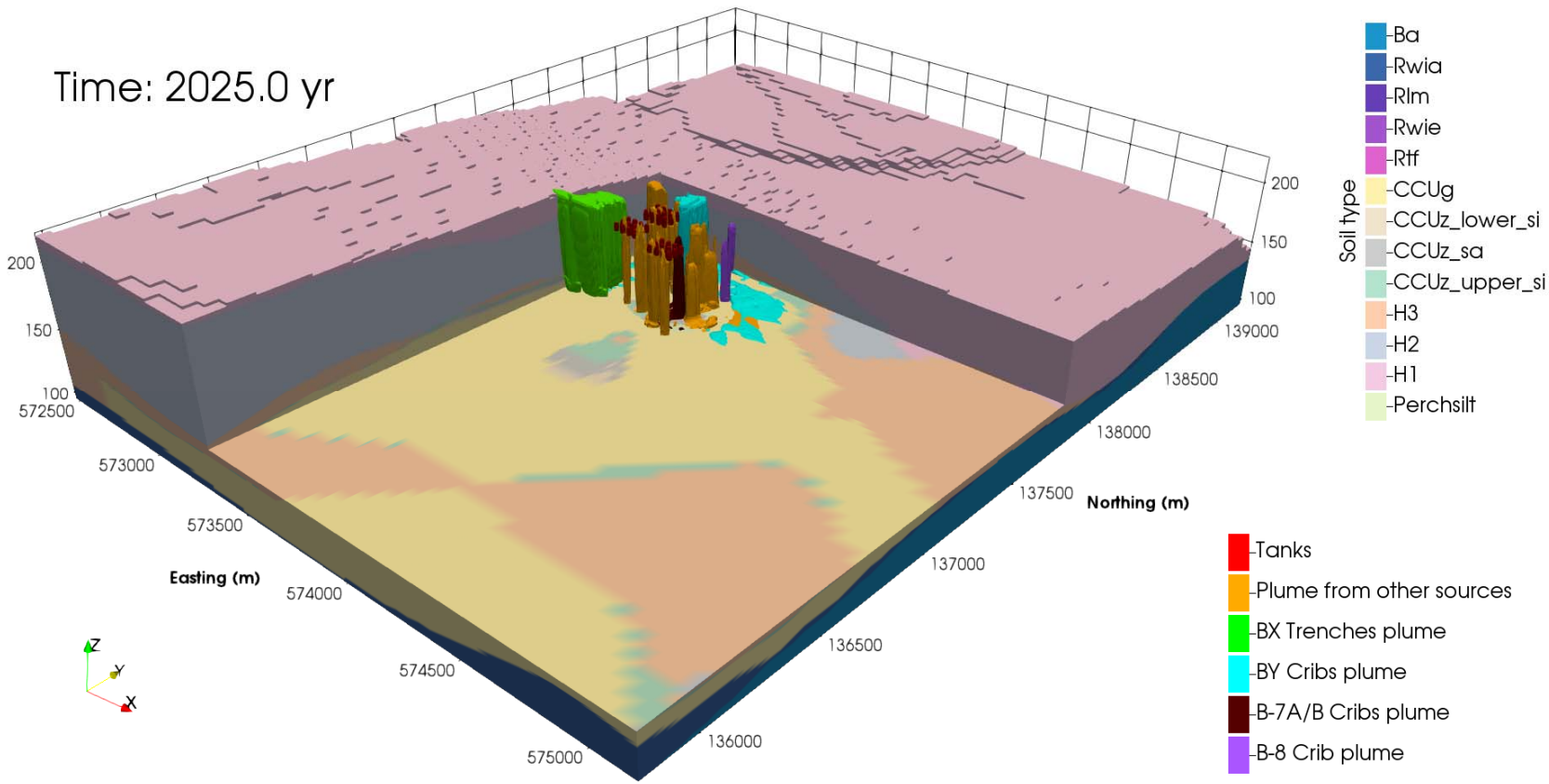

Figure B.39. Cutaway View of Hydrostratigraphic Units Underlying the B-Complex Showing Waste Storage Tanks of the B-BX-BY Tank Farms and Isosurfaces of Simulated Tc-99 Plumes [1 pCi/L] from Different Source Areas in 2025.

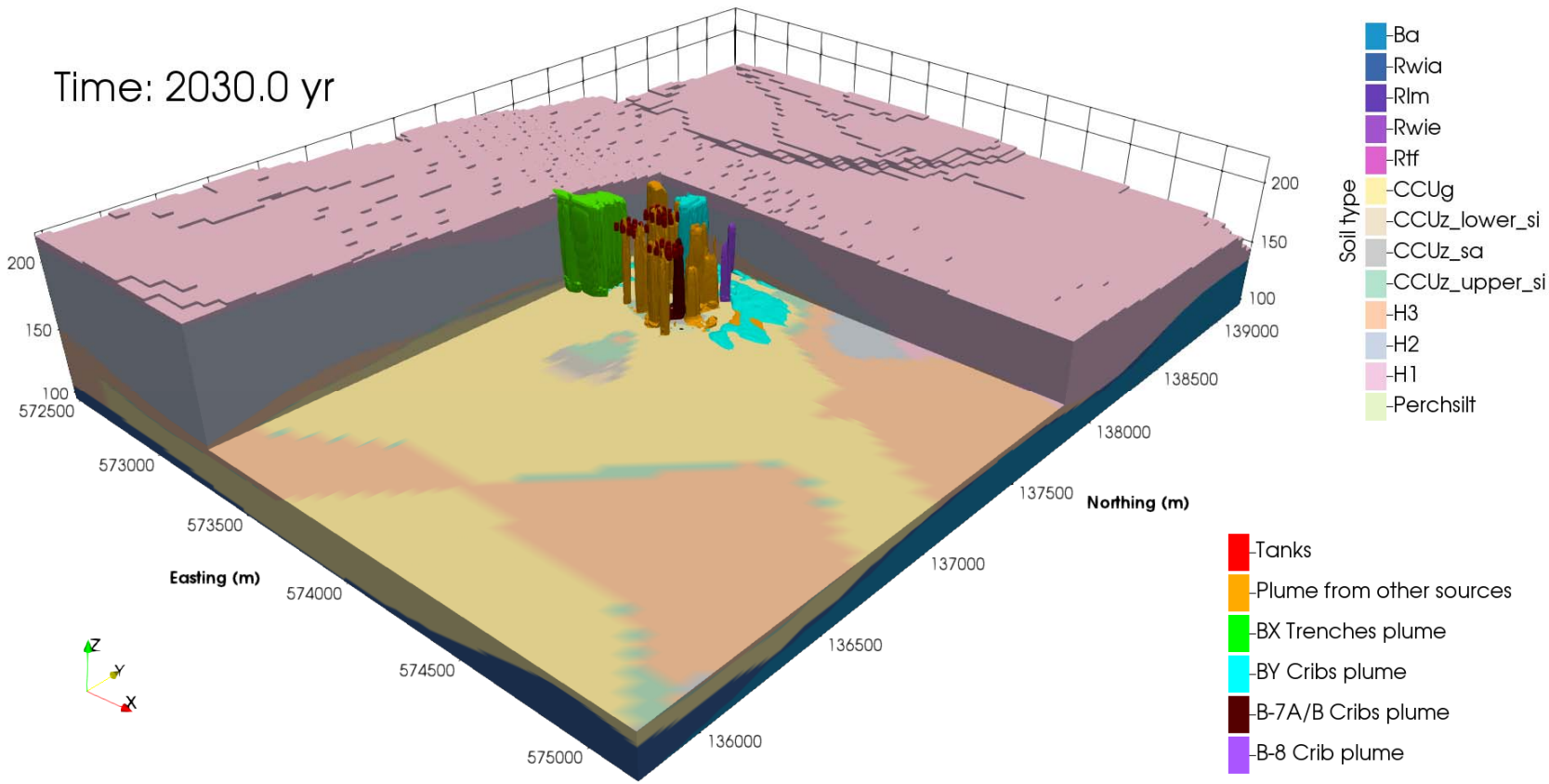

Figure B.40. Cutaway View of Hydrostratigraphic Units Underlying the B-Complex Showing Waste Storage Tanks of the B-BX-BY Tank Farms and Isosurfaces of Simulated Tc-99 Plumes [1 pCi/L] from Different Source Areas in 2030.

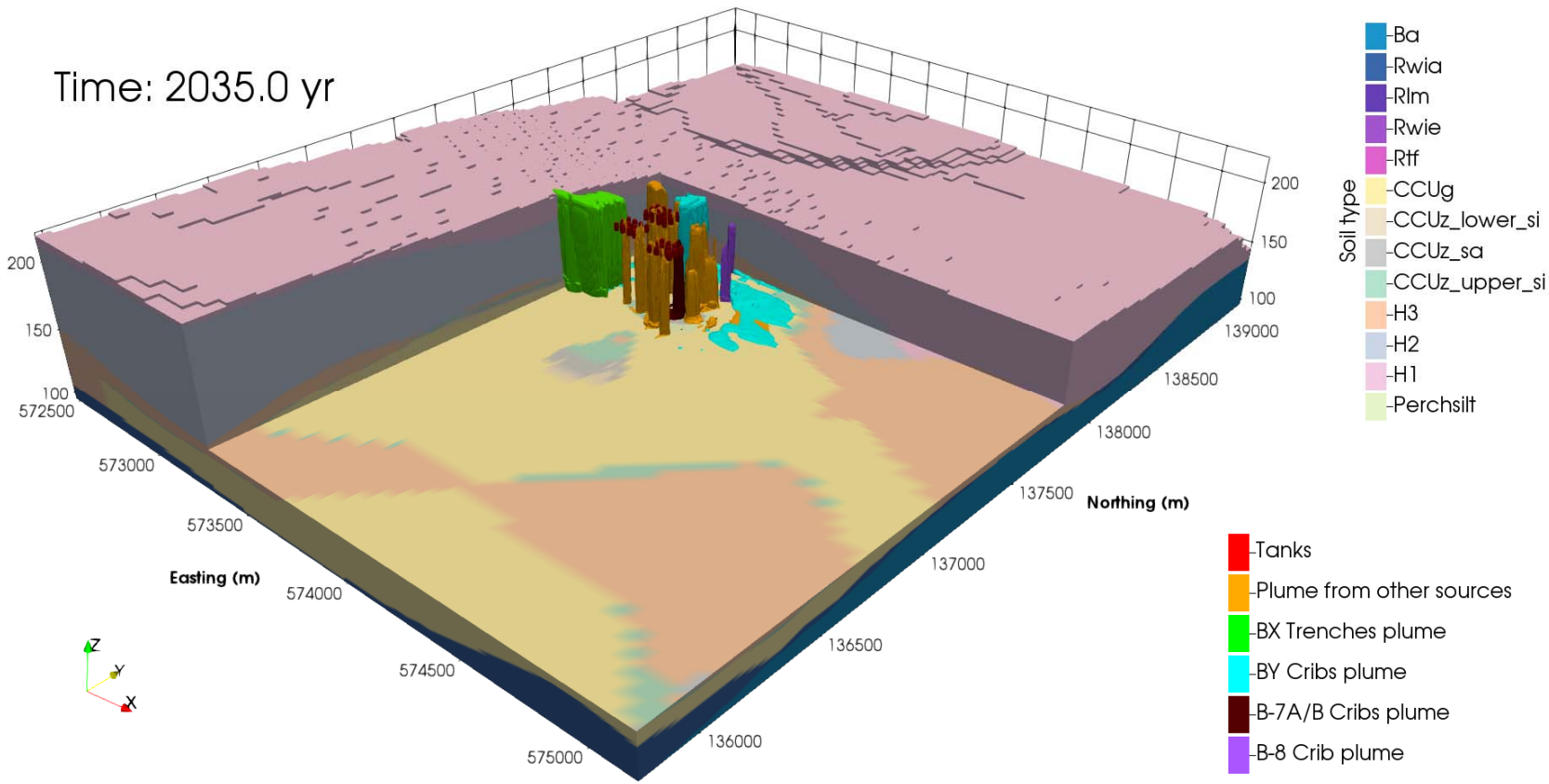

Figure B.41. Cutaway View of Hydrostratigraphic Units Underlying the B-Complex Showing Waste Storage Tanks of the B-BX-BY Tank Farms and Isosurfaces of Simulated Tc-99 Plumes [1 pCi/L] from Different Source Areas in 2035.

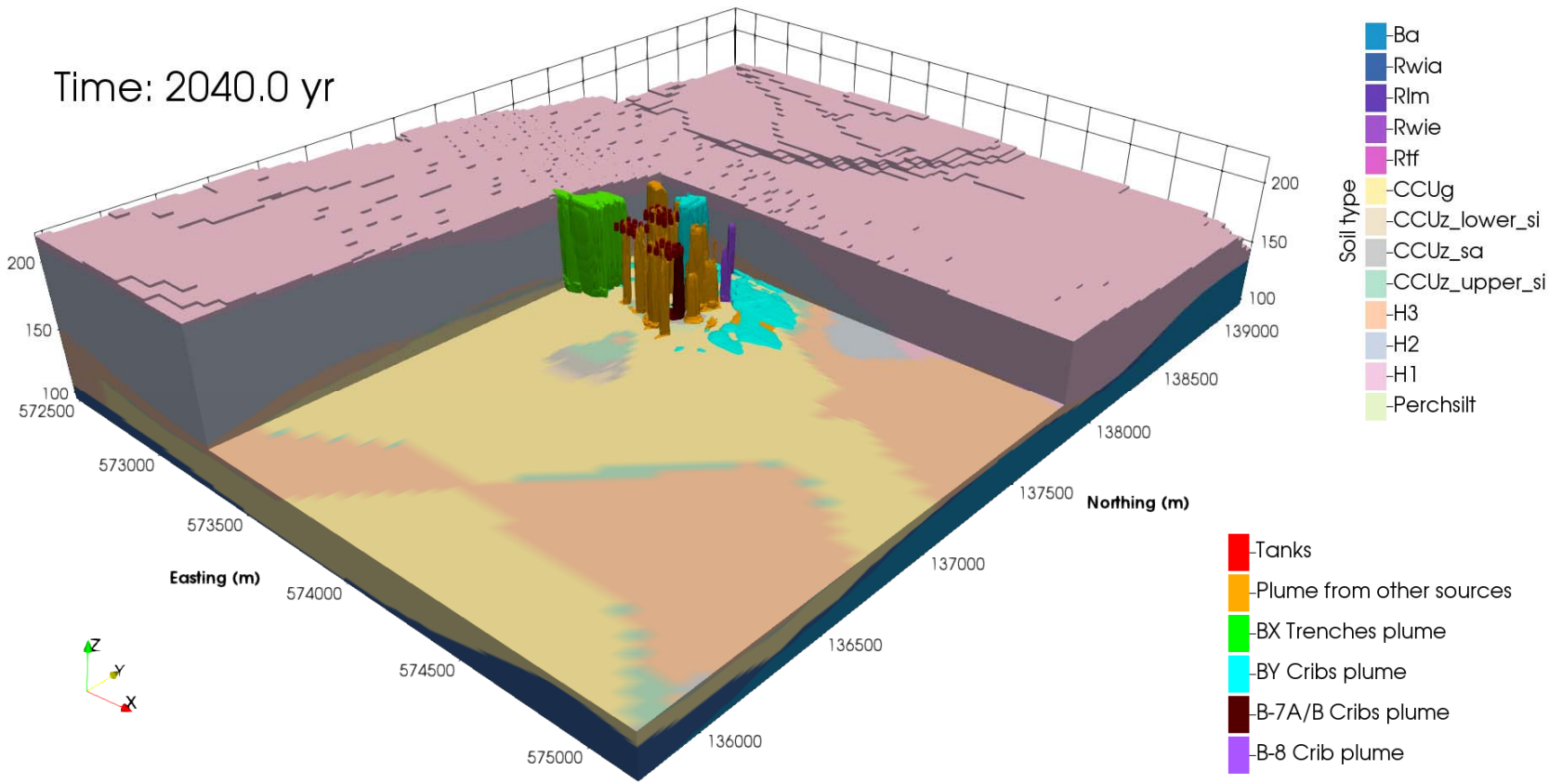

Figure B.42. Cutaway View of Hydrostratigraphic Units Underlying the B-Complex Showing Waste Storage Tanks of the B-BX-BY Tank Farms and Isosurfaces of Simulated Tc-99 Plumes [1 pCi/L] from Different Source Areas in 2040.

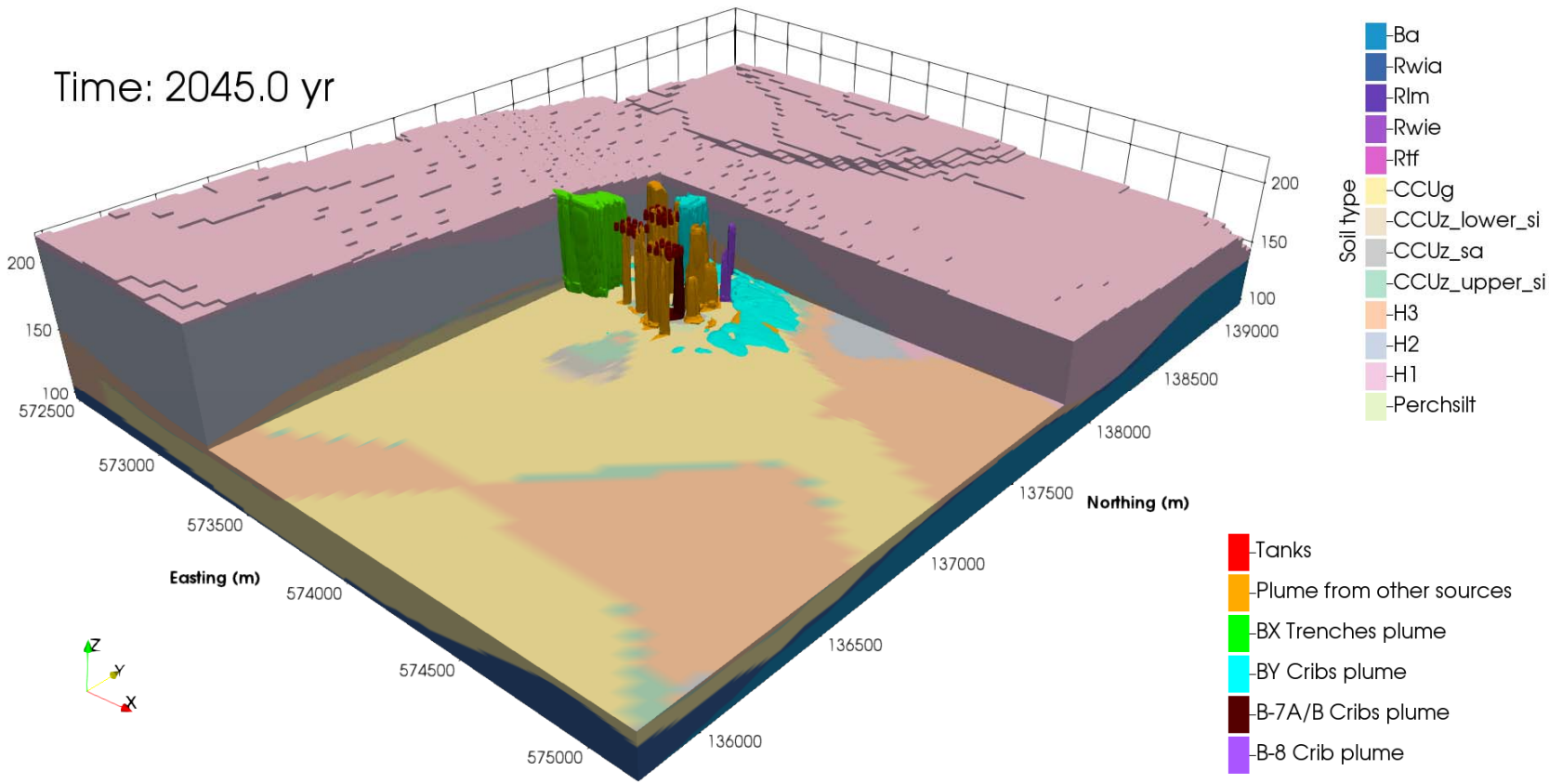

Figure B.43. Cutaway View of Hydrostratigraphic Units Underlying the B-Complex Showing Waste Storage Tanks of the B-BX-BY Tank Farms and Isosurfaces of Simulated Tc-99 Plumes [1 pCi/L] from Different Source Areas in 2045.

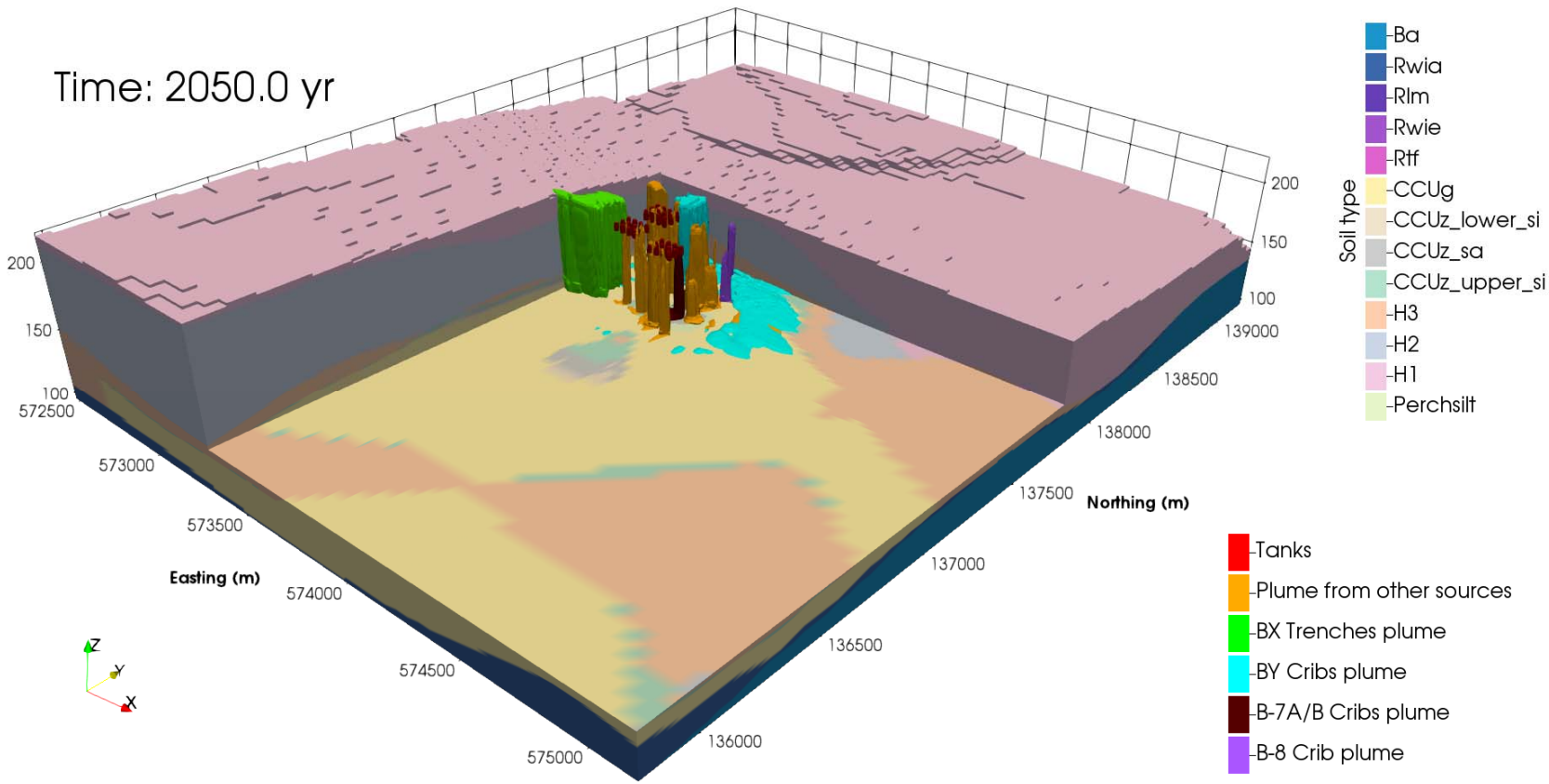

Figure B.44. Cutaway View of Hydrostratigraphic Units Underlying the B-Complex Showing Waste Storage Tanks of the B-BX-BY Tank Farms and Isosurfaces of Simulated Tc-99 Plumes [1 pCi/L] from Different Source Areas in 2050.

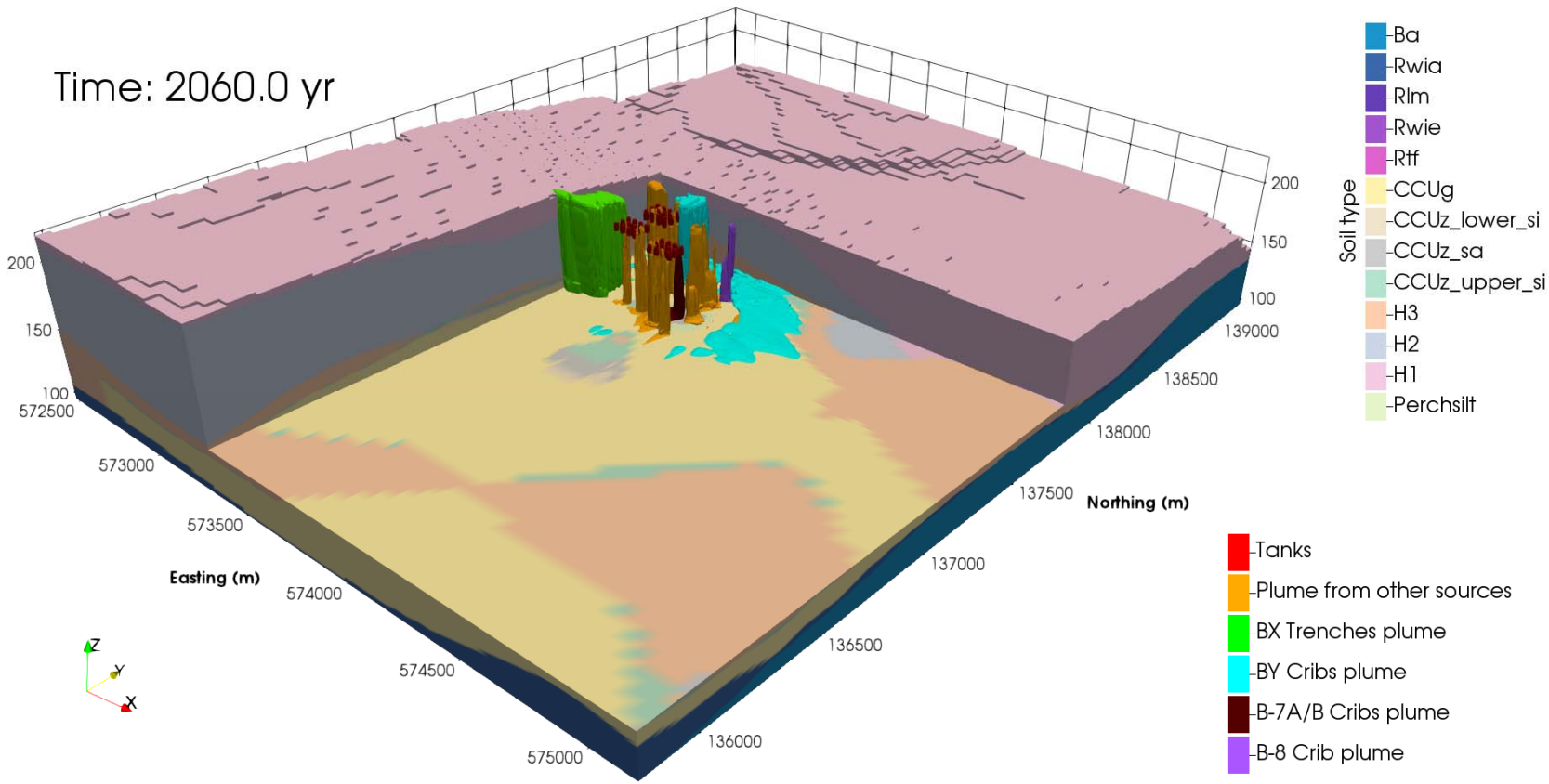

Figure B.45. Cutaway View of Hydrostratigraphic Units Underlying the B-Complex Showing Waste Storage Tanks of the B-BX-BY Tank Farms and Isosurfaces of Simulated Tc-99 Plumes [1 pCi/L] from Different Source Areas in 2060.

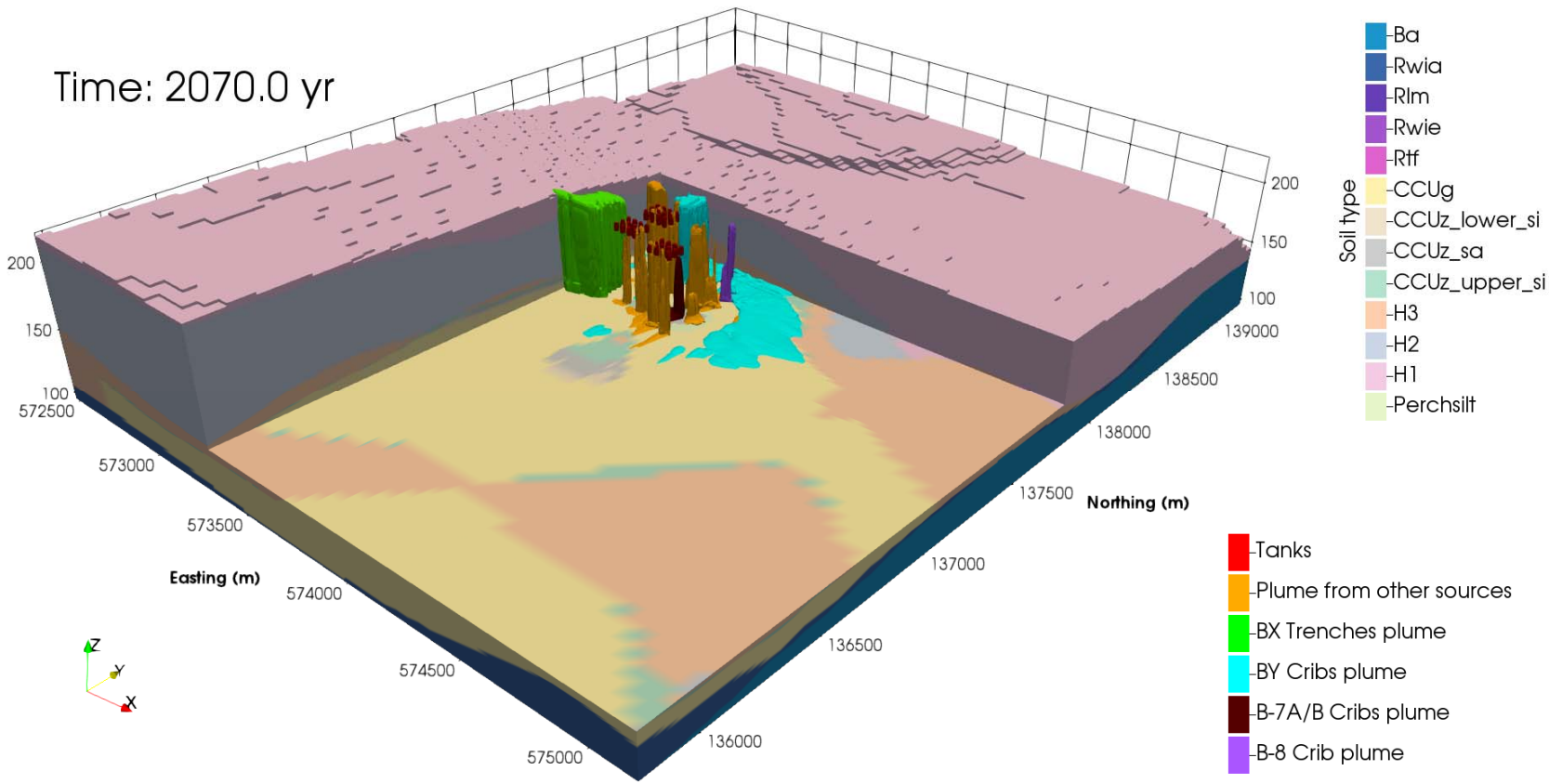

Figure B.46. Cutaway View of Hydrostratigraphic Units Underlying the B-Complex Showing Waste Storage Tanks of the B-BX-BY Tank Farms and Isosurfaces of Simulated Tc-99 Plumes [1 pCi/L] from Different Source Areas in 2070.

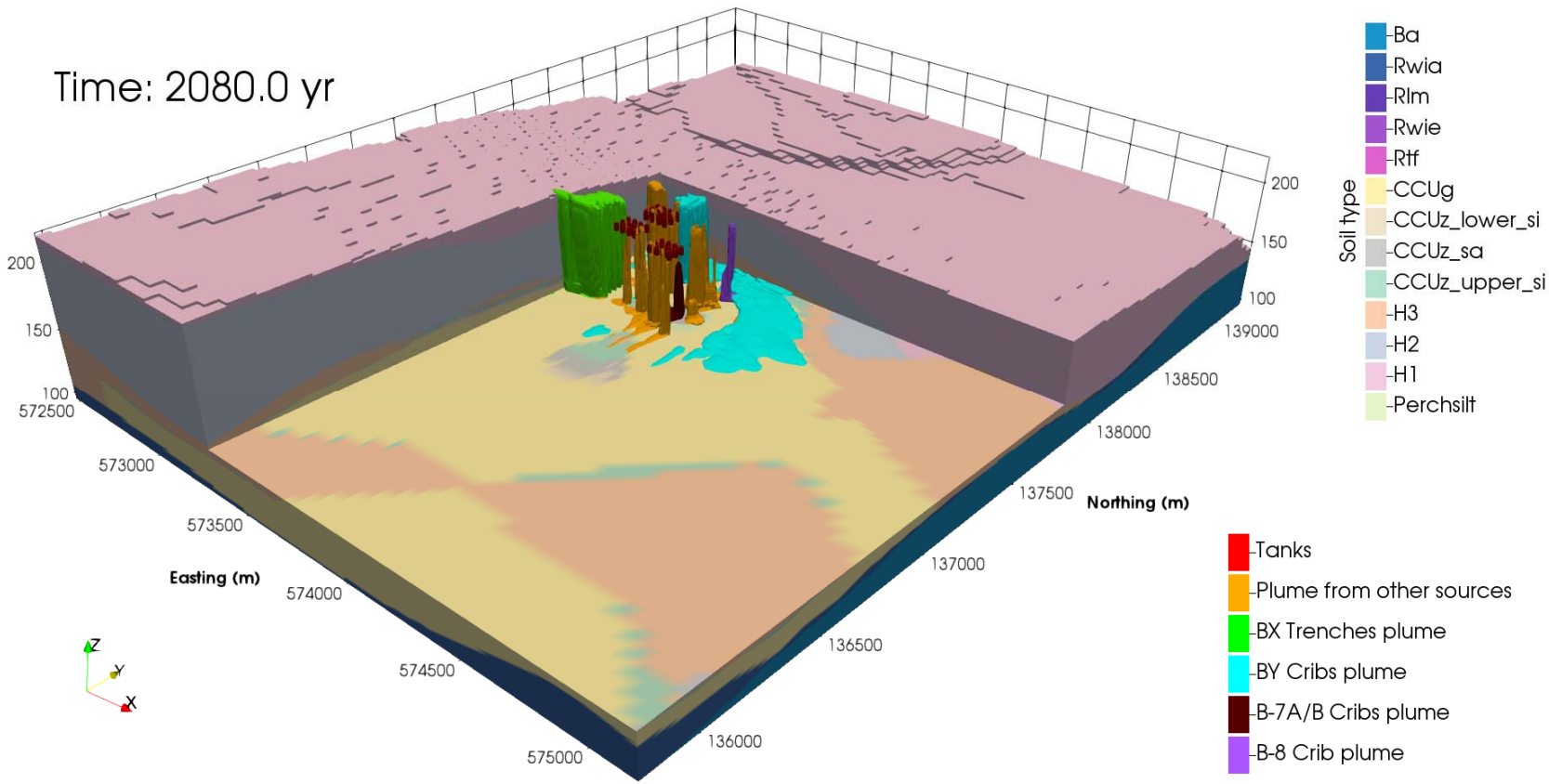

Figure B.47. Cutaway View of Hydrostratigraphic Units Underlying the B-Complex Showing Waste Storage Tanks of the B-BX-BY Tank Farms and Isosurfaces of Simulated Tc-99 Plumes [1 pCi/L] from Different Source Areas in 2080.

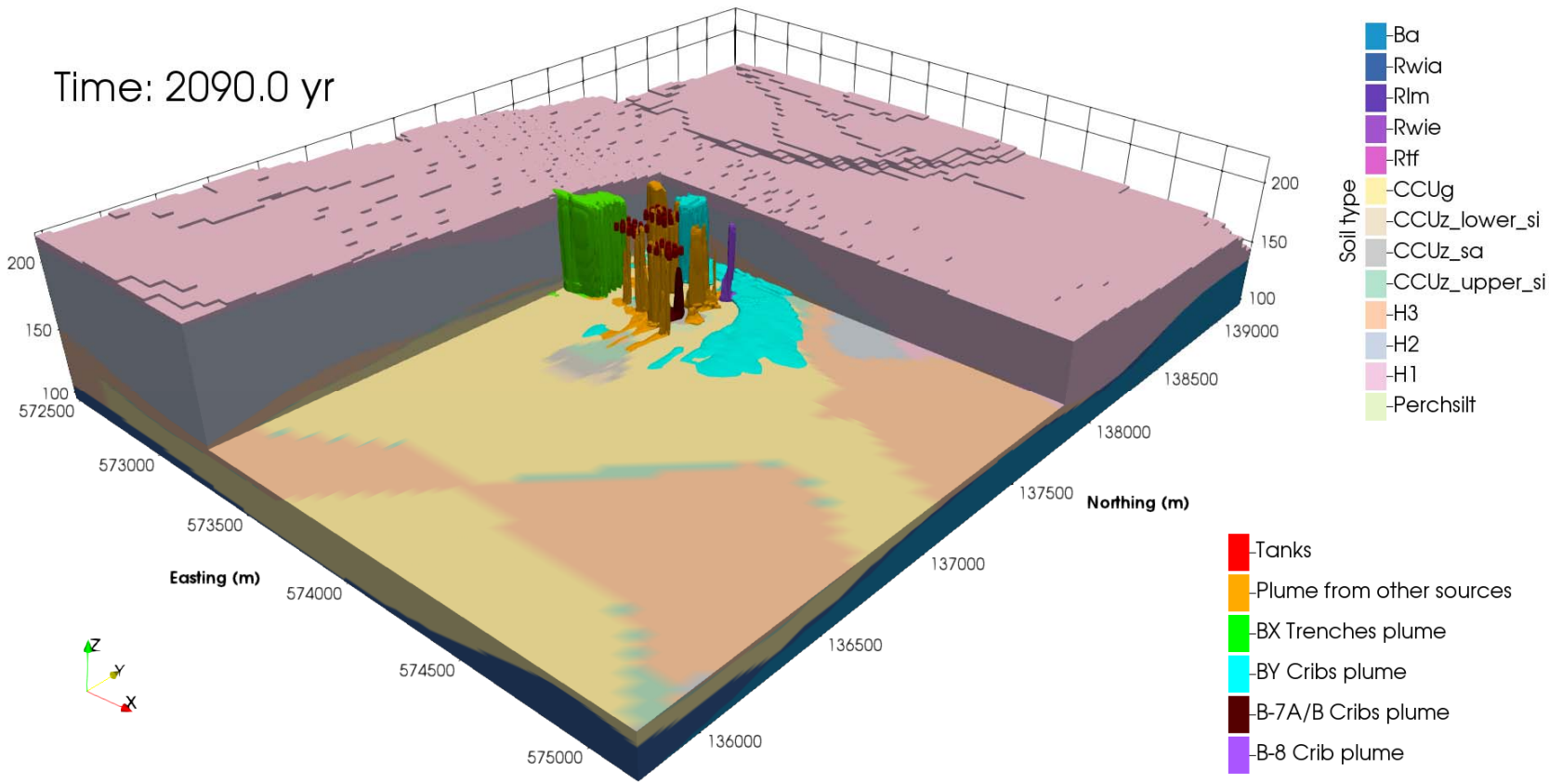

Figure B.48. Cutaway View of Hydrostratigraphic Units Underlying the B-Complex Showing Waste Storage Tanks of the B-BX-BY Tank Farms and Isosurfaces of Simulated Tc-99 Plumes [1 pCi/L] from Different Source Areas in 2090.

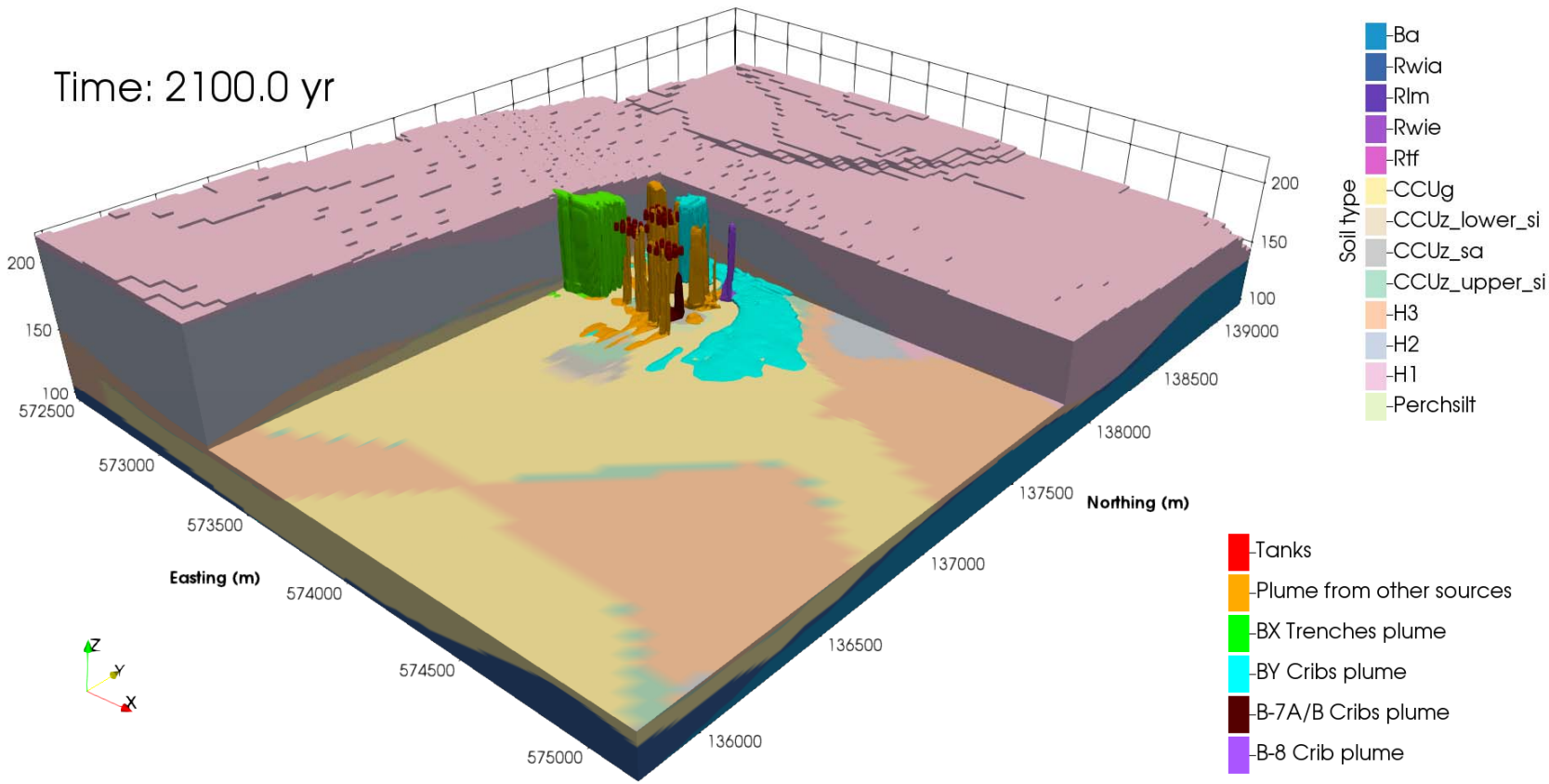

Figure B.49. Cutaway View of Hydrostratigraphic Units Underlying the B-Complex Showing Waste Storage Tanks of the B-BX-BY Tank Farms and Isosurfaces of Simulated Tc-99 Plumes [1 pCi/L] from Different Source Areas in 2100.

Distribution

No. of
Copies

\# Name
Organization
Address
City, State and ZIP Code

\# Organization
Address
City, State and ZIP Code
Name
Name
Name
Name
Name (#)

\# Name
Organization
Address
City, State and ZIP Code

No. of
Copies

\# Foreign Distribution
\# Name
Organization
Address
Address line 2
COUNTRY

\# **Local Distribution**
Pacific Northwest National Laboratory

Name	Mailstop
Name	Mailstop
Name	Mailstop
Name	Mailstop
Name	(PDF)

Pacific Northwest
NATIONAL LABORATORY

www.pnnl.gov

902 Battelle Boulevard
P.O. Box 999
Richland, WA 99352
1-888-375-PNNL (7665)

U.S. DEPARTMENT OF
ENERGY